The onset and propagation of GTRF wear

by

Zupan Hu

A dissertation submitted in partial fulfillment
of the requirements for the degree of
Doctor of Philosophy
(Mechanical Engineering)
in the University of Michigan
2016

Doctoral Committee:

Professor Wei Lu, Co-Chair
Professor Michael Thouless, Co-Chair
Professor James R. Barber
Professor William R. Martin

Dedication

To my grandfather

To my parents

To Qin

Acknowledgements

I am grateful to all individuals who have supported, guided and encouraged me throughout last several years.

Above all, I am deeply appreciative to my advisors Professor Wei Lu, Professor Michael Thouless and Professor James R. Barber, without whose help this dissertation is not possible. The discussions over years have been truly productive and encouraging. I have learned a great deal from their sharp insights and constructive comments, which will be a constant source of inspiration through my future career.

I am also thankful to my committee member Professor William R. Martin's leadership in the Consortium for Advanced Simulation of Light Water Reactors (CASL) program. I still remember the first time I met Professor Martin during my summer internship at Oak Ridge National Laboratory. I was impressed by his knowledge and expertise. I thank Professor Martin's guidance and encouragement.

Many thanks to the CASL program (http://www.casl.gov), an Energy Innovation Hub (http://www.energy.gov/hubs) for Modeling and Simulation of Nuclear Reactors under U.S. Department of Energy, for the financial and technical support over my entire graduate years. It was a great journey to be part of it.

I would also thank my research partners and friends such as Bai Song, Tianlei Li and Hai Wang, who made both my personal life and study full of joy.

At last, a special thanks to my family: my grandfather and my parents for their unconditional love and most importantly my wife Qin who has been supporting me over years.

Contents

List of Figures

List of Tables

Symbols

q	Contact shear stress
p	Contact compressive normal stress
μ	Friction coefficient
v	Poisson's ratio
E	Young's modulus
p_∞	Normal pressure load
q_∞	Tangential load
w	Wear depth
α	Wear coefficient
Γ_{II}	Mode-II toughness
$\hat{\tau}$	Mode-II cohesive strength
ξ_{II}	Instantaneous cohesive length
W_{IIo}	Work by sliding per unit area
K_1	Mode I stress intensity factor
K_{1I}	Mode II stress intensity factor
Q	Shear force
P	Normal force
σ_e	Von mises stress
σ_Y	Yielding strength
ε	Creep strain
T_0	Period of the real vibration cycle
T_i	Period of i^{th} effective vibration cycle
φ	Threshold of contact pressure variation (ratio)
g	Rod-to-grid gap
k_s	Spring stiffness
D_c	Cladding thickness
R	Rod outer radius
f	Load frequency
f_n	First natural frequency of a free rod
f_s	System natural frequency
F	Impact force
F_a	Force amplitude
U	Rod displacement
ρ	Density

Abstract

The Onset and Propagation of GTRF Wear

By

Zupan Hu

Co-chairs: Professor Wei Lu and Professor Michael Thouless

Grid-to-rod fretting (GTRF) wear in pressurized water reactors (PWR) is caused by the vibration of fuel rods against the spacer grid that supports them. GTRF problems account for over 70% of fuel failures of PWR worldwide, leading to costly maintenance and environmental impacts. Due to its complex dependence on factors such as geometry design of the spacer grid, creep deformation, gap formation and coolant flow, the root mechanism of the GTRF problems is still not well understood. The purpose of this dissertation is to provide a fundamental understanding of how the wear initiates from the contact edges and propagates over the entire contact interface, as well as how the key factors such as gap size and excitation frequency affect the wear growth.

The geometry design of the spacer grid is a critical factor determining the GTRF wear. Understanding the contact mechanics in the onset of partial-slip and the propagation of wear scar is the basis for geometry optimization. A new wear modeling method in which the geometry is updated by assigning fictitious eigenstrains to a set of surface elements is

developed. This method enables reliable and efficient modeling of wear in most commercial finite-element-analysis (FEA) codes. It is shown that the sensitivity of slip to the geometrical details of a corner is resolved when a finite interfacial shear strength is incorporated with a Coulomb friction law. The wear scar will propagate continuously to the entire contact interface when either an interfacial shear strength or a yielding strength is introduced, which is in sharp contrast to elastic models, and is more physically sound. As creep plays a similar role as wear in stress relaxation and gap formation, an algorithm is developed to couple wear and creep. The time scales of quasi-static vibration and wear is coupled using effective cycles with magnified wear coefficients. The length of these effective cycles is adjusted adaptively to limit the contact pressure relaxation over a cycle less than a reasonable threshold.

The dependence of wear growth rate on the gap and excitation frequency has been also systematically analyzed. It is found that the fuel rod may have three types of vibrational responses: subharmonic, period doubling and chaotic. The subharmonic vibration usually results in larger wear rate. For a given gap, it is found that there is a critical excitation frequency that leads to the maximum wear growth rate. A concept of system natural frequency is introduced. It is shown that the system natural frequency is determined by the gap size and closely related to the maximum wear rate.

Chapter 1

Introduction

1.1 Overview

In a pressurized water reactor (PWR), a fuel rod is a Zircaloy cladding with UO_2 fuel pellets inside it. As shown in Figure 1-1, the fuel rod is supported by spacer grids with springs and dimples. A fuel assembly has many rods, such as 17×17 Vantage5H and 16×16 Guardian in the USA [1]. The spacer grid has mixing vanes, which enhance the turbulence of the coolant flow to improve the efficiency of heat exchange. However, the turbulence of the coolant fluid also causes the fuel rods to vibrate against the grids that support them, causing fretting wear of the Zircaloy cladding [2, 3]. This phenomenon is called grid-to-rod fretting (GTRF).

GTRF problems account for about 74% of all fuel failures and are responsible for the costly shutdowns [4]. At the early stage of operation, the spacer grid can provide sufficient support to the fuel rod owing to an interference fit. However, over time, wear [1, 5] and creep [6] cause stress relaxation, and the vibration becomes more significant, which causes slip on the grid-to-rod contact interface. It is observed that the GTRF wear first occurs around the contact edges and eventually propagates to the entire contact interface [5], leading to possible formation of a gap [1, 4]. As a result of the gap, both normal and

frictional work rate will increase [7, 8], which significantly increases the wear rate and eventually causes fuel leak problem. This typical mechanism of the GTRF problems is summarized in Figure 1-2.

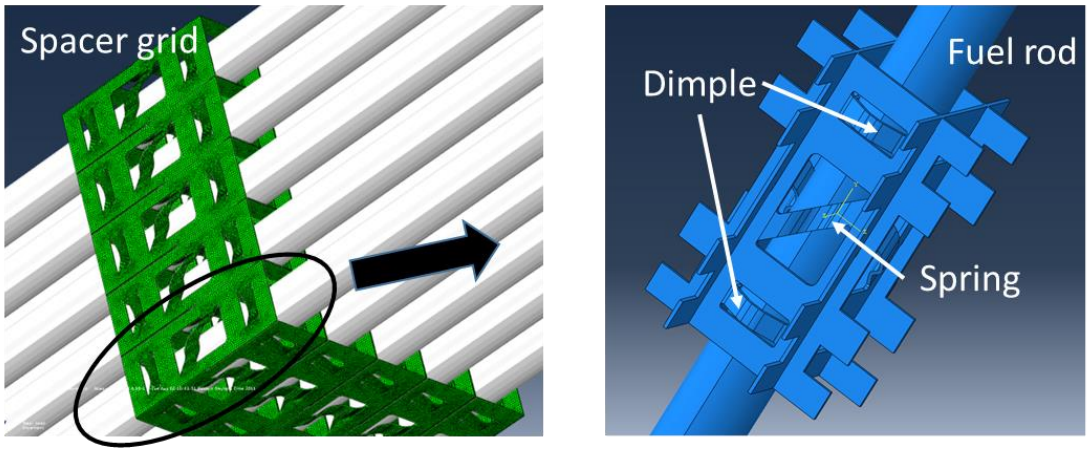

Figure 1-1: PWR fuel assembly and spacer grid.

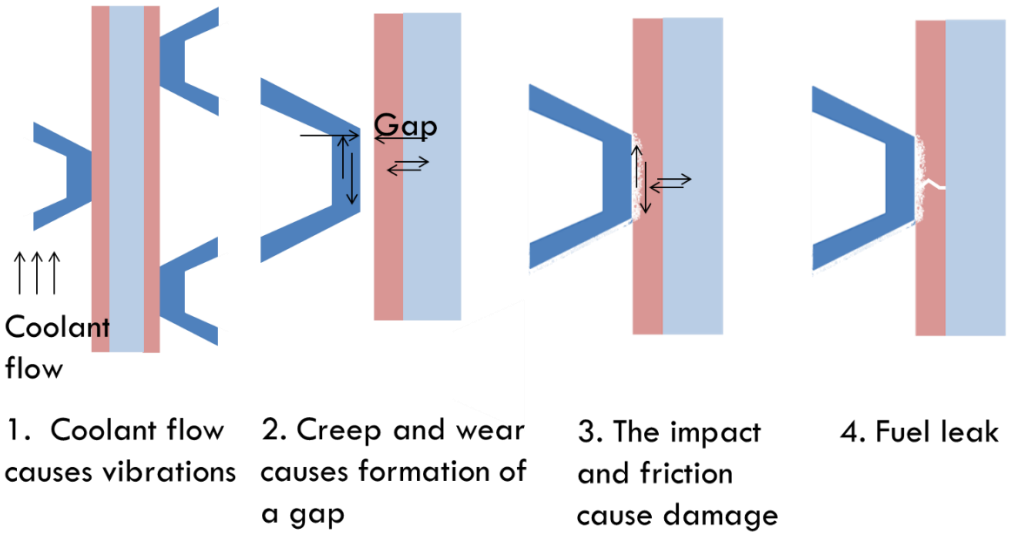

Figure 1-2: Grid-to-Rod Fretting wear causes fuel leak problem

General tribological methods such as coating [9], material change or lubrications are impractical [5] in reducing GTRF wear due to their effects on neutron economy or cool-

ant chemistry. Therefore, the focus of most existing studies is on the spacer grid geometry, turbulent flow, and vibration. It is commonly recognized that GTRF problems are caused by a complex interaction between the rods, grid and coolant [5, 7-13], but there appears to be no detailed description of how the wear starts and propagates, and how it depends on the excitation frequency from the coolant flow and the gap between the grid and rod.

The GTRF wear is governed by the contact mechanics of the grid-to-rod interface, which is the basis to optimize the geometry of springs and dimples on the spacer grid. As the spacer grid is usually manufactured from sheet metal, the variations of the geometry of the springs and dimples are limited. Both experiments and numerical simulations have been used to compare candidate geometry designs. Kim et al. [1, 14] compared two geometry designs of the spacer grid in fretting wear resistance using out of pile tests and found that a smaller contact surface leads to more severe wear behavior. So a support with a concave contour is suggested over a flat or convex one [12]. Similar results were also obtained by Kovács et al. [7] who compared the effects of point-type and plane-type contact on fretting sensitivity, and by Shin et al. through FEA-based optimization simulations [15]. Besides the size of the contact contour, the local wear behaviors are also important. Based on the tests and simulations by Kim et al. [5, 14], at the early stage of GTRF problems, the partial-slip may occur in both axial and transverse directions. Because the springs and dimples are usually manufactured through punching sheet metals, the contact may have sharp edges near which the wear is usually more significant (see Figure 1-3). For the same reason, axial slip usually causes more detrimental wear than

transverse slip [12]. Since the wear severity is strongly dependent on the contact mechanics at the contact contour, setting up clean theoretical models is particularly useful in understanding the onset and propagation of the GTRF wear, and in providing guidelines for the geometry optimization. Besides, it was also observed that the contact area increases considerably as the wear grows [5, 14]. So in a FEA modeling, the dimensional loss due to wear needs to be coupled with the contact modeling.

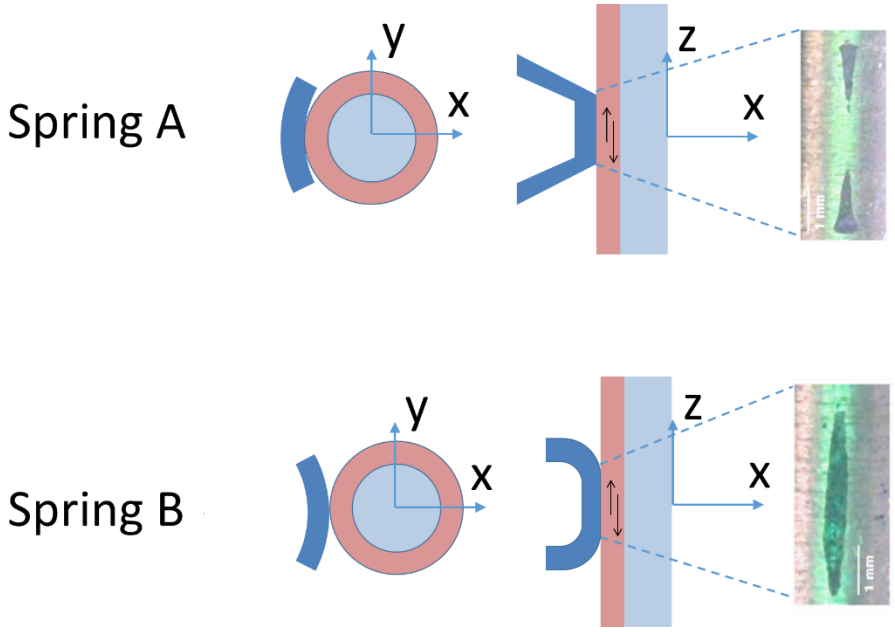

Figure 1-3: Partial-slip is likely to initiate from the sharp contact edges (redrawn based on ref. [5]).

The wear propagation in GTRF problems is also strongly dependent on creep. Due to high temperature and vibrations, both creep and wear may occur near the grid-to-rod contact interface, leading to stress relaxation. The stress condition affects the wear propagation, particularly the partial-slip wear scar [16, 17]. However, there are two major challenges in coupling creep and wear. First, the period of the vibration is usually short owing to the high turbulence in the coolant flow [2, 13], while the wear usually evolves slowly.

Therefore, a simulation based on the time scale of vibrations will be impractical due to the high computational cost. Unfortunately, an efficient algorithm to couple the time scale of vibration with that of wear is still missing. Secondly, the creep and wear may affect each other through the stress field near the contact interface. In a FEA simulation, the time increments need to be small enough so that one of them won't cause excessive error on the other. Since the contact conditions may change over time, a predetermined time increment may become inappropriate as creep and wear evolve. To address this issue, the time increments need to be adjusted adaptively so that the variation of stress near the contact interface is small enough.

The excitation force due to coolant flow also affects GTRF problems, which has been extensively studied. Of particular interest is how the flow rate affects the frequency of the excitation force and the fuel rod vibration. The pressurized coolant flows through the mixing vanes, becoming highly turbulent. Strong swirls with a Reynolds number as high as 500,000 forms in the sub-channels, causing vibrations of the fuel rod against the spacer grid [18]. Based on the CFD analysis by Delafontaine and Ricciardi [18], the fluid forces, as a input for the structural analysis, has a dominant frequency that depends on the particular design of the mixing vanes. Based on PSD analyses of CFD simulation results, Yan et al. [10] also drew the same conclusion. The flow rate is closely related to the dominant frequency of the excitation force, which further affects the vibration of the fuel rod. Fuel assembly tests under different flow rates by Kim [2] show the amplitude and the frequency of the vibration are the key factors determining the fretting wear. It was observed that there is a critical flow rate that causes maximum rod vibration amplitude [19]. However, the mechanism of how the frequency of excitation force affects the vibration of the

fuel rod is still not well understood. By comparing the results of those CFD analyses with the fuel rod vibration tests, it is noticed that there is significant discrepancy on the predicted frequency. The dominant frequency of the excitation force is generally greater than 150 Hz depending on the geometry of mixing vanes and particular flow condition [10, 18], while the vibration frequency of the fuel rod is observed to be less than 60 Hz [2, 13]. Those designs are from commercial companies and therefore are similar, while the difference of the input and output frequencies is fairly significant. How the excitation frequency affects the vibration and wear needs to be investigated.

Vibration of a constrained fuel rod has also been studied based on 1-D numerical simulations, especially under conditions with a gap between the fuel rod and the springs/dimples on the spacer grid. For example, Rubiolo and Young [13] studied the key factors affecting the GTRF wear using a 1D numerical model [20, 21]. The wear damage is modeled by solving the motion and normal work of a gapped-supported beam system. The authors show that grid-to-rod gap and the turbulence forces are two important factors affecting the wear risk, while other factors such as grid misalignments and the cell tilts are less critical. Based on the results of the analyses, the rod reaches a peak vibration amplitude and maximum velocity when the excitation frequency is around 50-60Hz. Efforts were also made in studying the natural frequency of the constrained fuel rod. Using a simplified 1D model, Kim [22] found that the natural frequency of the fuel rod is around 2-36Hz depending on the particular gap conditions. Using similar models with a continuously supported fuel rod, Choi et al. [23] compared the vibration characteristics of two spacer grid designs and found that the natural frequencies of the rod are about 32 and 47

Hz when constrained by the two grids, respectively. Those models provides general vibrational characteristics of the fuel rod, which is particularly useful in understanding the big picture of the GTRF problems. However, a gapped supported system is extremely nonlinear, and the vibration is strongly dependent on both the gap size and the excitation frequency [24-26]. The mechanism of how the gap size and the excitation frequency affect the vibration and the wear is still not clear. Besides, the friction energy dissipation is the major cause of the wear on the cladding [27], which cannot be captured by those models. However, the local wear behaviors is crucially important in understanding the severity of the GTRF wear. As criteria of fuel failure, the maximum wear depth and total wear volume need to be determined.

In this dissertation, a new geometry-updating method which enables reliable and efficient wear modeling [16] will be developed. Using this method, how the wear starts near the contact edges and propagates over the entire contact interface [28, 29] will be investigated. Both smooth and sharp edges are covered, so that the contact mechanics in both axial and transverse directions will be understood. An algorithm to couple creep and wear together in a simulation will also be developed, which is critical in understanding how the creep and wear lead to formation of a gap. After a gap forms, the growth rate of wear is strongly dependent on the dynamic responses of the rod, so we also studied how the gap size and the excitation frequency affect the wear rate and the durability of the system.

1.2 Modeling wear using fictitious eigenstrain

Modeling the material removal caused by GTRF wear is crucial in understanding the root mechanism of gap formation. Since the local slip conditions are very sensitive to the local profile of the contact surfaces, the growth of wear depth and the contact modeling

needs to be coupled in the FEA modeling. However, frequent remeshing is computer intensive and may cause convergence problems. Moreover, there may be no remeshing module available at all in many FEA packages. In Chapter 2 [16], a new wear modeling method using fictious eigenstrain is introduced. Instead of remeshing, a set of eigenstrains are assigned to the surface elements to mimic the dimension change due to wear. The commonly available expansion module is used so that minimum additional knowledge is required in using this method. The eigenstrain method enables efficient and easy modeling of the wear evolution in GTRF problems in most FEA codes. This method does not require unloading the contact stress and therefore provides advantages in modeling the wear propagation in grid-to-rod interface, which is highly dependent on the creep history. As an example, a simple FEA model is set up to illustrate the application and the validity of the method.

1.3 Wear propagation

In a fuel assembly, the spacer grid is designed to hold the fuel rods tightly using a preload created by a small interference. However, due to the vibration caused by the coolant flow, slip will occur near the contact edges, especially when the preload is relaxed by the creep. Eventually, the partial-slip evolves to full-slip, and the wear rate becomes much more significant. Therefore, analysis of partial-slip wear is a key to understand the mechanism of GTRF wear and to optimize the geometry of the spacer grid. Available elastic studies based on a Coulomb-friction law show that the stick-slip boundary does not move as the wear evolves, which results in unrealistic singular stresses when the wear depth is large enough. In this dissertation, clean models are set up to understand how the interfacial shear strength and plasticity affect the wear propagation.

1.3.1 Effects of interfacial shear strength

Stamping of sheet metal creates sharp edges on the springs and the dimples, leading to high stress levels around those contact edges. It is observed that the wear often initiates from those edges [5], and therefore the contact mechanics around them needs to be understood. A common criterion to determine the slip regions at an interface is the Coulomb's law, which states that the interface has a local shear strength that is equal to the product of the local applied pressure and the coefficient of friction. However, in elastic analyses around a sharp contact edge, the stresses generally exhibit a singular form, going to infinity at the edges [30]. The shear strength of the contacting materials must provide an upper bound to this interface strength, and the concept of a finite strength has been used in wear and slip studies [31, 32]. Slip analysis based on a Coulomb's law only is also sensitive to the geometrical details of the corner, which is inherent to the real applications. In Chapter 3 [28], the effects of finite interfacial shear strengths on the stick-slip behavior in a partial-slip interface will be investigated. It will be shown how the incorporation of finite shear strengths concept with a Coulomb friction law solves the unrealistic singular shear stress issue. The sensitivity of stick-slip behaviors to local geometry can be modeled more reliably. Similar to the next section, it is also observed that the partial-slip zone will propagate to the entire contact interface.

1.3.2 Effects of plastic deformation

Partial-slip wear modifies the surface profile in the slip zone and causes the redistribution of stress [17, 33-35]. Using a Coulomb friction law, Goryacheva et al. show that the stick-slip boundary does not move in the wear process [17]; similar results were also obtained through numerical analyses [34-36]. After a long enough time, the materials on the

contact surface are worn away and there will be no contact in the slip zone. As a result, the system becomes elastically similar to a crack, and the normal and shear stress near the stick-slip boundary will be asymptotically singular. In real application, however, the stress may evolve to a level that is greater than the yielding strength and the interfacial shear strength. In this case, the plasticity starts to play an important role in the stress evolution and the wear propagation. In Chapter 4 [29], a partial-slip model is formulated in a general way so that the results can be projected to all problems with a smooth contact edge and a small partial slip zone. The partial-slip wear problem is simulated by incorporating yielding strengths, which may lead to the propagation of partial-slip and wear across an interface.

1.4 Coupling creep and wear

In a fuel assembly, both wear and creep may play important roles in the stress relaxation. To model the propagation of slip, and the formation of a gap, efficiently and accurately, we need to couple the two mechanisms together. However, as is mentioned in section 1.1, there are two issues need to be addressed. First, the vibration in the GTRF problems has a much shorter time scale than a significant amount of wear. If the model is based on the time scale of the vibration, the computational cost will be impractically high. Secondly, both the wear and creep are very nonlinear, and they affect each other through the contact pressure. If the time increments are too large, one of them may cause excessive error on the other one. We need to optimize the time increments so that the two behaviors can be coupled effectively. In Chapter 5, an algorithm is developed to couple the time scale of vibration and that of wear and creep. Instead of modeling every vibra-

tion cycle, a magnified wear coefficient is used, so that one cycle in the model can effectively represent many cycles. These cycles are defined as effective cycles. To couple the creep and wear efficiently, a threshold of stress relaxation is set to make sure the change of contact pressure is close to but less than the threshold.

1.5 The effects of gap and frequency on GTRF wear

The wear and creep in a fuel assembly leads to the formation of a gap between the spring/dimple and the fuel rod [1, 4]. In this case, it is found that both the impact and sliding effect will contribute to the wear growth, which significantly increases the wear rate [1, 4, 19, 37]. However, because the vibration of such a loosely supported rod is nonlinearly sensitive to the gap size and the excitation frequency [25], it is still not clear how the wear rate depends on the two factors. In Chapter 6, a 3D FEA model is set up to simulate the vibration and the wear under a large spectrum of gap size and excitation frequency. It is found that the rod vibration mode may experience sub-harmonic, period doubling and chaotic regimes. The wear rate is closely related to those regimes. A concept of system natural frequency that produces the maximum wear rate is developed, and the dependence of this frequency on the gap size is determined.

Chapter 2

Simulation of wear evolution using fictitious eigenstrains

2.1 Introduction

Wear is a cause of failure in GTRF problems as well as many other engineering applications [18, 29, 38, 39]. Predictions of the magnitude and distribution of wear is crucial for safety and for the determination of operational costs. The local wear rate depends on the contact pressure, and even relatively small amounts of wear can change the profiles of the contacting bodies sufficiently to have a significant influence on the distribution of contact pressures. The contact and wear problems are therefore fully coupled and require an incremental formulation.

2.1.1 Methods for wear modeling

The Euler scheme is commonly used for wear modeling [40-44]. At each time step, the contact tractions are determined based on the instantaneous geometry of the system, and the wear rate is determined from these tractions using a wear law such as that proposed by Archard [45]. The geometry is then updated by the wear predicted at each node during the time step, and the process is repeated. The geometry updating can be realized by either remeshing or an alternative technique such as adjusting the magnitude of gap elements to account for wear [46]. In principle, the geometry should be updated after

each time step, but this would usually be prohibitively computer-intensive, particularly since contact problems typically require a relatively fine mesh in the contact area [47]. Instead, it is usual to solve the contact problem under the assumption that the undeformed profile remains unchanged for an extended period of time. If the loading is periodic, the model is indexed through one complete loading cycle and the total wear predicted at each node is determined. This cyclic nodal wear is then multiplied by an appropriate factor n to approximate the wear during a macro-time step of n loading cycles, after which the geometry of the contacting bodies is updated appropriately. Alternatively, the size of the macro-time step can be adjusted so as to ensure that the nodal wear is large enough to be numerically significant, but not so large as to introduce significant errors [41, 48, 49].

Soderberg and Andersson [42] found that frequent mesh adjustments can induce stability problems, and may increase the difficulty of numerical convergence. For example, they found that the adjustment of nodal coordinates may result in a spurious gap at some nodes necessitating repositioning of the contact components which introduces additional uncertainty into the accuracy of the results. Techniques have also been developed to improve the stability of the model when the wear depth is large compared with the element size [40]. If the mesh adjustment is distributed among several layers of elements, the mesh quality can be preserved [49, 50]. Both the remeshing and multi-layer methods can effectively improve numerical stability, but they increase computational cost significantly.

In this chapter, we present a new method in which the geometry is updated by imposing fictitious eigenstrains in the surface elements. Using thermal expansion as an example, we ascribe fictitious temperatures to the surface nodes such that thermal expansion

(actually contraction) mimics the geometry change due to wear. Since expansion modules are available in most finite-element codes, this procedure requires minimal program modifications by the user and avoids the need for remeshing in cases of moderate wear. This is particularly useful for systems with a dependence on loading history, such as elastic-plastic or Coulomb friction problems. Here we shall introduce the general work flow of the method, and validate it by comparing results of a simple example with a conventional remeshing scheme.

2.2 Wear modeling by fictitious eigenstrains

The nodal displacement induced by wear is realized by controlling the eigenstrain of a layer of fictitious elements adjacent to the contact surface. We use a two-dimensional ABAQUS model for the purpose of illustration, but this method is equally applicable for three-dimensional geometries and other finite element packages. In this chapter, the eigenstrain is realized by the thermal expansion module, but we can also use other available expansion modules.

Figure 2-1 shows a region of the finite-element mesh near the expected contact region, both in the undeformed condition, and as modified by wear defined through a vector of nodal displacements $\mathbf{W}=\{W_1 , W_2 .... W_m\}^T$, where m is the number of potential contact nodes. The required wear profile is achieved by assigning (negative) appropriate values to the corresponding *m* element eigenstrain $\mathbf{\Delta}=\{\Delta_1 , \Delta_2 .... \Delta_m\}^T$. All of the non-surface nodes are assigned zero temperature, and the thermal conductivity is set to be zero, so that the temperature distribution remains unchanged. In order to avoid unwanted lateral displacements, at every time step, the local orientation of the elements in contact is tracked by a subroutine. The thermal expansion coefficient is set to be anisotropic and

only the components normal to the contact surface is non-zero, therefore expansion occurring only in the direction normal to the worn local contact surface.

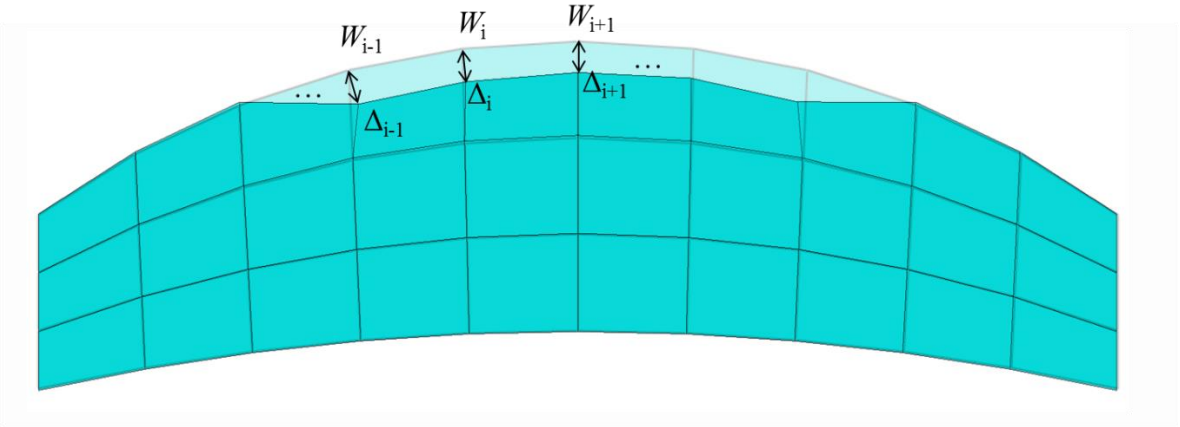

Figure 2-1: The geometry updating is realized through thermal expansion of a layer of fictitious element adjacent to the surface.

In order to implement the method, we need to determine the relation between the vectors **W** and **Δ**. In ABAQUS, the nodal thermal displacement depends on the temperature of the neighboring nodes as well as that of the node itself, but in a linear model we can represent this relationship in the form.

$$W_i = A_{ij}\Delta_j \tag{3-1}$$

where $i,j \in (1,m)$ and **A** is a matrix which depends only on the properties of the original finite element model. In principle, **A** can be extracted from the finite-element code, using appropriate matrix operations [51]. However, an easier, though less elegant, approach is to note that if no loads are applied and if the nodal temperature vector is set to

$$\Delta_j = \delta_{kj} \tag{3-2}$$

where δ_{kj} is the Kronecker delta, the resulting nodal displacements will be

$$W_i = A_{ij}\delta_{kj} = A_{jk} \tag{3-3}$$

Thus, a single run of the code with this temperature distribution yields the coefficients A_{ik} with $i \in (1,m)$, which defines the k^{th} row or column of **A**. Repeating the operation m times for each value of *k*, we can construct the entire *m*×*m* matrix **A**.

2.3 Eigenstrain wear modeling

We next embed the wear calculations in an Euler updating algorithm which is similar to that used with more conventional remeshing methods. We assume Archard's wear law [45] in the form

$$\dot{w}(x,t) = \mu\alpha\dot{h}(x,t)\,p(x,t). \tag{3-4}$$

where μ is the coefficient of friction, α is the wear coefficient, $p(x,t)$ is the local contact pressure and $\dot{h}(x,t)$ is the slip velocity at the contact surface [$h(x, t)$ is the slip *displacement*]. In the finite-element model, the contact pressure and the wear rate are expressed in terms of nodal values $P_i(t)$, $W_i(t)$ through the relations

$$\dot{p}(x,t) = \sum_{i=1}^{m} P_i(t)v_i(x)\,, \quad \dot{w}(x,t) = \sum_{i=1}^{m} \dot{W}_i(t)v_i(x)\,, \tag{3-5}$$

where $v_i(x)$ are the element-shape functions. It follows from Eqs. (3-4) and (3-5) that

$$\dot{W}_i(t) = \mu\alpha\dot{H}_i(t)P_i(t)\,, \tag{3-6}$$

where $\dot{H}_i(t)$ is the instantaneous slip velocity at node *i*. The nodal forces, $P_i(t)$, are determined by running the finite-element contact simulation through a complete loading cycle, after which Eq. (3-6) can be numerically integrated by dividing the loading cycle into appropriate time steps, Δt, and writing

$$W_i(t+\Delta t) = W_i(t) + \mu\alpha\left[H_i(t+\Delta t) - H_i(t)\right]P_i(t). \tag{3-7}$$

The resulting cyclic nodal wear is then multiplied by the factor *n* to determine the wear vector **W** after *n* cycles of loading. As the wear growth in a cycle is usually small, this is mathematically equivalent to the use of an enhanced wear rate $n\alpha$ in a single cycle of loading. The fictitious eigenstrain vector, $\mathbf{\Delta}$, is then updated through the inverse relation

$$\mathbf{\Delta} = \mathbf{A}^{-1}\mathbf{W}. \tag{3-8}$$

This algorithm is shown as a block diagram in Figure 2-2.

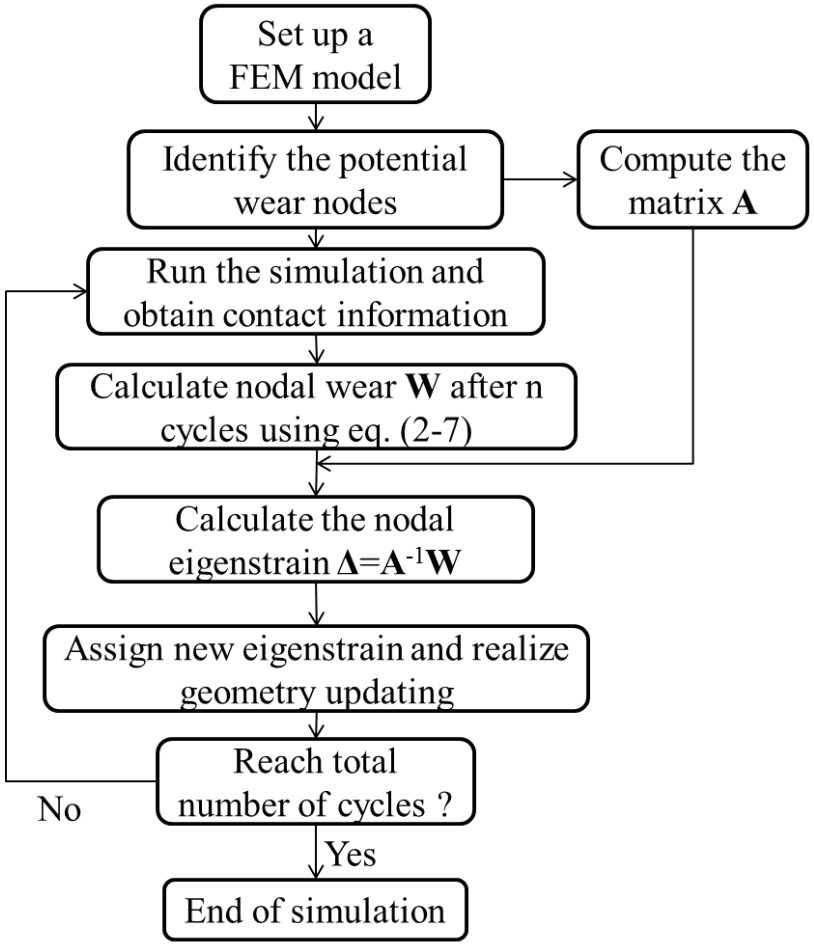

Figure 2-2: An Euler wear scheme based on the eigenstrain method.

2.4 Validation and application in wear simulation

We implemented a two-dimensional ABAQUS model, using an anisotropic thermal expansion module to generate the eigenstrains, for the purpose of illustration, but the method is equally applicable for three-dimensional geometries, other finite-element packages, and other modules that represent eigenstrains. A round-on-flat sliding model was created, as shown in Figure 2-3. A constant vertical pressure, p_∞, was applied to the system as a preload. Then, an oscillating horizontal displacement, d, as applied to the top

surface of the indenter. The amplitude of this displacement was chosen to be sufficient to cause slip at all nodes.

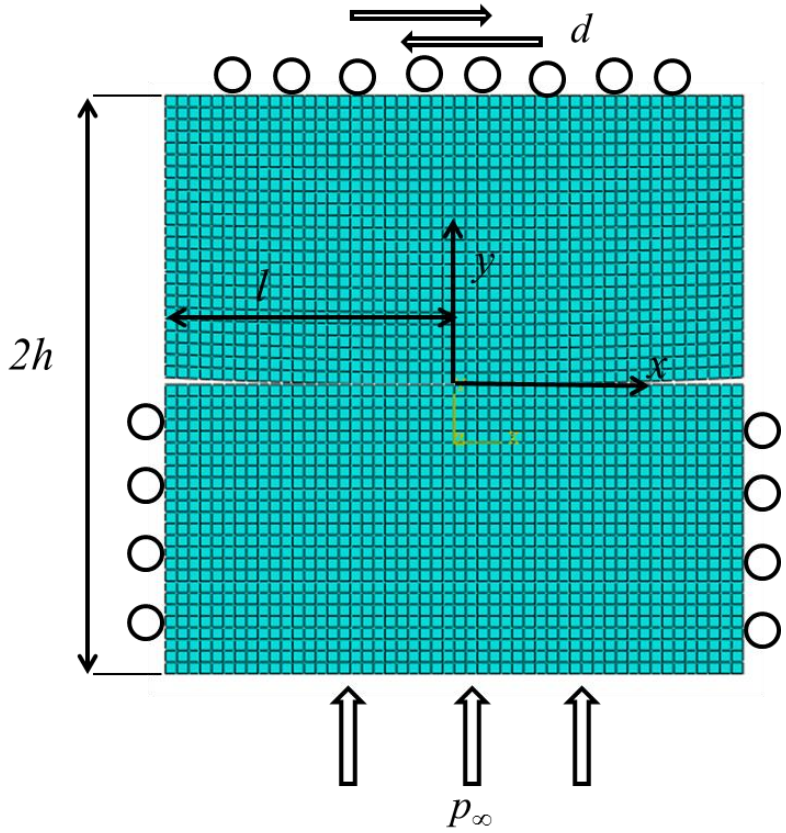

Figure 2-3: A 2D plane-strain wear model with boundary conditions of a compressive pressure, p_∞, and an oscillating horizontal displacement, *d*, The indenter and substrate are elastically similar.

In this particular implementation, the eigenstrain vector, $\boldsymbol{\Delta}$ was obtained by assigning negative temperatures, T_i to each contact nodes, corresponding to the appropriate eigenstrains through $\Delta_i = \alpha_T T_i$, where $\alpha_T T_i$ is the coefficient of thermal expansion of the surface elements. All of the non-surface nodes were assigned zero temperature, and the thermal conductivity was set to be zero, so that the temperature distribution remained unchanged. Obviously, this method cannot be used in problems involving actual thermo-

elastic deformations, but in these cases the appropriate eigenstrains can be generated by alternative methods, such as anisotropic swelling modules.

Results for the wear profile and for the evolution of the contact pressure were obtained by two methods: (i) the algorithm of Figure 2-2, and (ii) a conventional remeshing algorithm. In the remeshing algorithm, the contact nodes were relocated manually based on the predicted wear after n cycles and the original loading scenario was repeated. Since this procedure essentially involved unloading and then reloading the model after the geometry had been updated, the remeshed model was run for a few cycles until a steady cyclic state was identified. We note that ABAQUS contains an adaptive remeshing module, but we encountered convergence problems when computing the contact interactions without the unloading and reloading step.

Figure 2-4 shows the normalized wear profile after 100 and 200 stages of geometry modification, which corresponds to 100n and 200n loading cycles respectively. The dimensionless parameter values used were μ =0.1, αE=0.0075, ν=0.25, d/l=0.005, E/p_∞=3750, h/l=1, where ν and E are Young's modulus and Poisson's ratio, respectively. The results of the thermal-expansion method are shown as circles and those of the remeshing method as crosses. Clearly the two methods give essentially identical results. Similarly, the contact pressure predicted by the two methods is shown in Figure 2-5. The percentage differences between the results of the two methods shown in Figure 2-5 are slightly larger than that in Figure 2-4, but the two sets of results are still not visually distinguishable. Since it slips at all nodes, the frictional traction is everywhere proportional to the contact pressure.

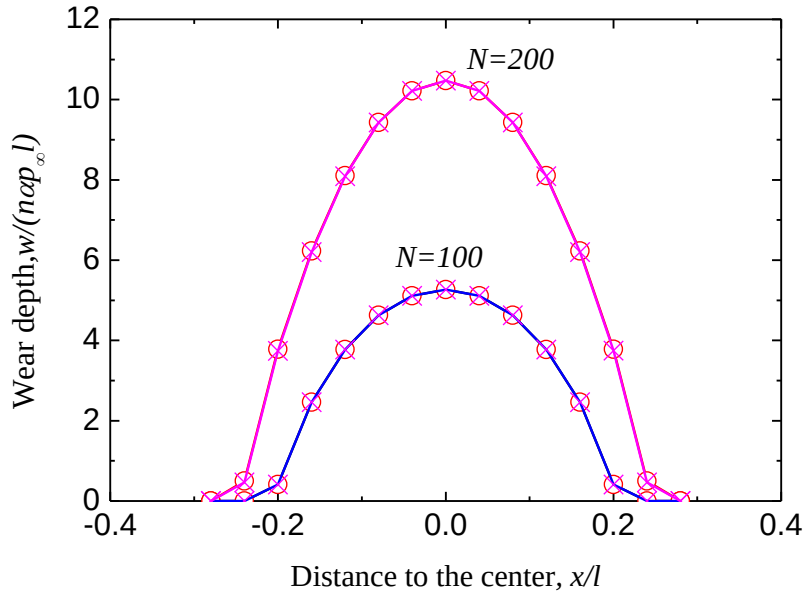

Figure 2-4: Dimensionless wear profiles predicted by the thermal expansion algorithm (circles) and the remeshing method (crosses) for the model shown in Figure 2-3. *N* is the number of stages of geometry modification.

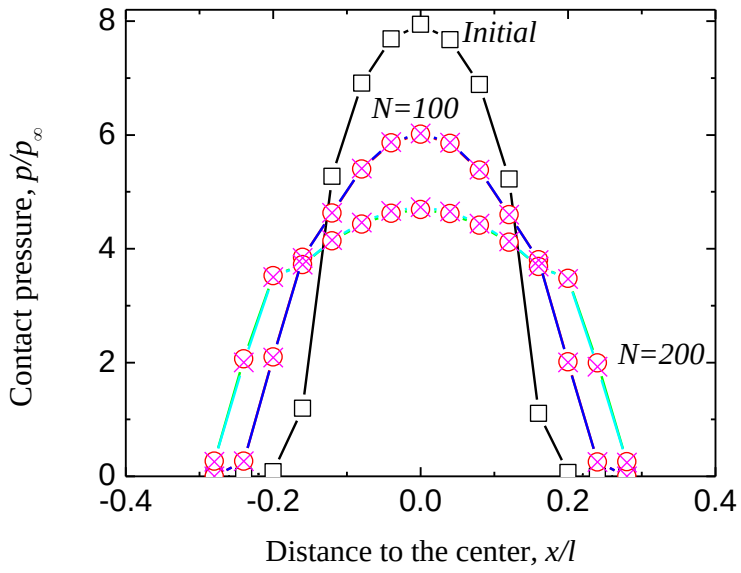

Figure 2-5: The contact pressure predicted by the thermal expansion algorithm (circles) and the remeshing method (crosses).

2.5 Discussion

In conventional remeshing algorithms, it is generally necessary to unload the contact stress on the contact interface each time the geometry is updated. This is undesirable in problems involving plastic deformation, where unloading may lead to unintended modifications of the residual stress field. Also, in fretting problems, where frictional slip is restricted to a part of the contact interface, unloading will release residual frictional slip in the stick zone [30, 52]. This necessitates running the model through several cycles to achieve a steady state after each mesh adjustment, and even then, the release of residual slip may lead to accumulated errors. The adaptive-mesh module in ABAQUS appears to permit remeshing without unloading and reloading, but the present authors' experience was that this causes convergence problems.

By contrast, the example illustrated here shows that the eigenstrain algorithm generates the same solution as a conventional algorithm, without the need for unloading and reloading. This alogrithm is considerably easier to implement than a remeshing algorithm. Although we used a simple two-dimensional model for the illustration in Section 4, the thermal-expansion algorithm can also be applied to three-dimensional models. The method can also be extended using modifications previously introduced in remeshing algorithms. For example, the method can be used to model wear problems with large wear depth. If the wear depth is larger than a critical value [49, 50], the geometry change can be distributed by defining non-zero temperatures over several layers of elements. We also note that other wear laws can be used in place of Eq. (3-4), provided that they depend only on quantities calculable from the underlying finite-element contact model. Besides, although the eigenstrain is realized by the thermal expansion as a example, it should be

noted that the wear profile can also be mimicked by other available expansion modules. For example, we can equally mimic the geometry change by fictitious swelling, which releases the temperature field for thermal simulation and enables the application of this method in thermo-tribological problems.

2.6 Conclusions

The eigenstrain algorithm described in Sections 2.3 and Figure 2-2 provides an efficient and easy to use alternative to conventional remeshing algorithms in finite-element solutions of contact problems involving wear. It enables wear modeling in various finite element codes using available expansion modules. The method allows geometry updating without unloading the contact stress on the contact interface, this could be of advantage in history-dependent problems such as those involving plasticity and/or hysteretic friction and microslip.

Chapter 3

Effects of interfacial shear strength on wear propagation

3.1 Introduction

In a fuel assembly, the fuel rod is supported by springs and dimples on spacer grids. As the springs and dimples are created by punching sheet metals, the contact edges in axial direction may be sharp [12]. The wear is often initiated at the edges of contacts [5] (see Figure 1-3), where there are high stresses. This type of contact limits the life of the fuel rod as well as components in many other applications [53]. In elastic analyses of this contact problems, the stresses generally exhibit a singular form, going to infinity at the edges [54]. However, the ratio between the normal and shear stresses stays constant around a corner, so an assumption of Coulomb friction leads to a prediction of wear only for coefficients of friction is low enough. Whether wear occurs, and the extent to which it occurs can depend on subtle details of the contact geometry. Similar issues of sensitivity to local geometry are inherent for problems of crack propagation in interfacial fracture mechanics. In that field, the concept of cohesive zones, that incorporate finite limits to the strength of the interface, has been found to be a useful tool to resolve some of the unrealistic complexities associated with singular stresses, particularly at small length scales, while retaining some of the general features of fracture mechanics that apply at larger scales [55-57]. In this

chapter we apply the insight provided by this field of interfacial fracture mechanics to interfacial slip, showing that the invocation of a finite shear-strength changes the slip and wear behavior at corners in important ways.

The contact across an interface between two bodies can be described by three regimes of behavior that depend on the geometry and the loads [58]. The first regime is full-stick, where the interface is effectively bonded across its entire length, and the two bodies act as a single entity. The second regime is full-slip, where there is relative motion between the two bodies along the entire interface. The third regime is partial-slip, where the two materials slide relative to each other along some parts of the interface, and are effectively bonded along others. Wear is associated with the energy dissipated by sliding [58, 59], and the analysis of wear requires modeling the relative slip along the interface between the two bodies. The full-stick and full-slip regimes can be relatively easy to describe, but partial-stick regions can provide more of a challenge. However, this regime is particularly important to analyze because fretting wear is often enhanced at the boundary between the slip and stick zones [59], and because the geometry changes induced by partial-slip and wear may result in wear spreading across an interface.

Coulomb's law is a common criterion used to determine when slip occurs. This law states that the magnitude of the interfacial shear stress, q, is limited by the product of the local applied pressure across the interface, p, and the coefficient of friction, μ:

$$|q| \le \mu p \tag{4-1}$$

Slip occurs if this condition cannot be satisfied without allowing a relative shear displacement across the interface. The coefficient of friction is generally assumed to be a

constant that is characteristic of the interface; if it is assumed to vary, non-linear effects are introduced [60].

Coulomb's law allows for the possibility of an arbitrarily high interfacial shear stress, if the local pressure is high enough. Indeed, Coulomb slip at a corner results in singular stresses. This unphysical result can be avoided by assuming that the magnitude of the shear stress is limited by an interfacial shear strength, $\hat{\tau}$, that is independent of local pressure [31, 32]. For example, the shear strength of the contacting materials could provide an upper bound to this parameter. Local equilibrium then requires a second condition that

$$|q| \le \hat{\tau} \tag{4-2}$$

This concept of a single-valued interfacial shear strength, is commonly used in fiber composite models [61-64], as well as in thin-film and composite-laminate cracking problems [55, 65]. The strength of the singularity depends on the details of the geometry and is the same for both the shear stress and the pressure [66-68]. This means that the ratio of the shear to normal stress is constant near the corner, no matter how high the stresses are. So, depending on the magnitude of the friction coefficient, slip by the Coulomb criterion either occurs everywhere in the singular region, or there is complete sticking within the singular region. Partial-slip occurs when the Coulomb condition is met within the singular field, but not outside it. However, the stress field associated with Coulomb slip is still singular, both the contact pressure and the shear stress increase without limit as the corner is approached.

The particular problem addressed in this chapter is partial-slip and wear at the edges of contacts. In a system that is fully stuck, the interfacial stresses follow the elastic field, and are, therefore, generally singular near the edges of a contact. The details of the singularities depend on the details of the geometry as in the related wedge and notch problem [67, 68], and the effects of loading and geometry on the amplitude of the interfacial stresses near the edge are reflected implicitly by parameters known as stress-intensity factors. These stress-intensity factors are analogous to those used to describe the singular elastic stress fields close to a crack tip, which have an inverse square-root singularity. The strength of the singularity is the same for both the normal and shear stresses. This means that the ratio of the two stresses is constant in the singular field. So, depending on the magnitude of the friction coefficient, slip (by the Coulomb criterion) either occurs everywhere in the singular region, or there is complete stick.

If slip and wear occur in the singular region at the corner of a contact, a crack-like geometry can evolve at the interface, with the corresponding singularity. Results from the fracture-mechanics literature suggest that the ratio of the stresses in the crack-tip region can be equal to the ratio of the applied shear and normal loads. In other words, if global slip does not occur, local slip at the crack tip will not occur. This result was identified for partial-slip in the Hertz contact problem [66]. In the Hertz contact problem, the normal stresses are not singular, but the shear stresses are [69]. This results in a region of partial-slip, where wear can occur, along the exterior circumference of the contact. However, even if the wear in this region proceeds to the limit in which there is no longer any contact, the slip does not progress beyond this region with Coulomb friction, even though there are infinitely high shear stresses ahead of the wear scar [66].

Accurate identification of regions of partial-slip near the corners of contact is critical for quantitative predictions of wear evolution. However, with an assumption of Coulomb friction, whether slip occurs, or not, depends entirely on the details of the elastic stress singularity [67, 68, 70]. These singular stresses result in non-physical behaviors, and cause the stress distributions and regions of slip to be very sensitive to the details of the geometry. The use of cohesive-zone models for fracture mechanics, with finite interfacial strengths, has been shown to resolve, in a physically satisfying manner, some of the complications associated with elastic fracture mechanics [55-57]. These include [56], for example, the stress oscillations and interpenetration that can occur with modulus mismatch [66], as well as the generally unphysical nature of infinite stresses. However, cohesive-zone models have the advantage of capturing the essence of the elastic solutions under conditions when they are expected to be approximately valid. (The elastic solutions will always break down close to corners and crack tips, but there can often be intermediate scales at which elasticity results hold. Cohesive-zone models illustrate the correct behavior in these intermediate scales, but keep stresses within physical bounds.)

The development of a cohesive zone ahead of a mode-II crack corresponds to interfacial slip, up until the point at which mode-II fracture occurs [56]. While we don't use a cohesive-zone formulation in this chapter, we use some of the concepts such as a cohesive-length scale to explore how slip with a finite shear strength might evolve in regions of elastic singularities, and how it might lead to the propagation of partial-slip and wear across an interface.

The goal of this chapter is to investigate the effects of finite interfacial shear strengths on the stick-slip behavior of contacting surfaces. By incorporating the concept of finite

shear strengths with Coulomb friction laws, the stick and slip zones can be predicted more accurately, and with less sensitivity to local geometry. It will be shown that one important consequence of introducing a finite shear strength, is that local wear induced by partial-slip can spread from a corner, and that this is a distinct contrast to what would be predicted with only a Coulomb criterion.

3.2 Methodology

3.2.1 No slip

In this chapter we consider the contact between two elastic bodies with the same elastic properties, and contacting each other at surfaces. Figure 3-1 shows a magnified view near the corner with an exterior angle of ϕ for such a system. If the interface between the two bodies does not satisfy either of the two slip conditions given by Eq. (4-1) and Eq. (4-2), the stresses are given by the elastic solution for a wedge. Close to the corner, the stresses are singular. For example, along a line that bisects the exterior angle, the singular component of the normal and shear stresses are given by [30, 70]

$$p_{\theta\theta}(r) = K_I r^{\lambda_I - 1} \tag{4-3a}$$

$$q_{r\theta}(r) = K_{II} r^{\lambda_{II} - 1} \tag{4-3b}$$

where r is the distance from the corner, K_I and K_{II} are the mode-I (symmetrical) and mode-II (anti-symmetrical) stress-intensity factors. The strengths of the singularities, λ_I and λ_{II}, depend on the angle ϕ. The two stress-intensity factors depend on the details of the corner, but they also depend on the macroscopic geometry and the applied loads.

They are analogous to those used in fracture mechanics, and describe the effects of the geometry and loads.

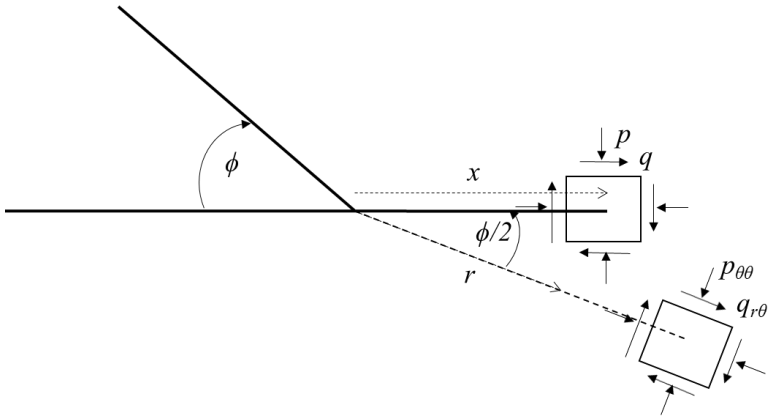

Figure 3-1: Geometry of a corner with an exterior angle ϕ, and an interface along which sliding can occur.

Eq. (4-3) describes the singular stresses along a line that bisects the exterior angle. Of particular interest are the normal pressure, p, and shear stress, q along the interface [30]:

$$p(x) = K_I f_1 x^{\lambda_I - 1} + K_{II} f_2 x^{\lambda_{II} - 1} \tag{4-4a}$$

$$q(x) = K_I f_1 g_1 x^{\lambda_I - 1} + K_{II} f_2 g_2 x^{\lambda_{II} - 1} \tag{4-4b}$$

where x is the distance along the interface (Figure 3-1), and f_1, f_2, g_1 and g_2 are functions of ϕ. The specific geometry we will consider in this chapter is one for which ϕ = 90°. For this case, based on the analytical solutions from Ref. [30], the stresses along the interface are given by:

$$p(x) = 0.7303 K_I x^{-0.4555} - 1.0873 K_{II} x^{-0.0915} \tag{4-5a}$$

$$q(x) = 0.3966 K_I x^{-0.4555} + 0.2381 K_{II} x^{-0.0915} \tag{4-5b}$$

3.2.2 Coulomb slip

A comparison between Eq. (4-4) and the Coulomb slip law of Eq. (4-1) reveals that slip will always occur in the singular region at the corner of a contact if $\mu < g_1(\phi)$, since λ_I dominates the stress field close to the corner. In particular, slip will occur if $\mu < 0.543$ for the right-angled geometry considered in this chapter. If the Coulomb slip condition is met within the singular region, the asymptotic stress field develops a different singularity, λ_s, that is a function of both ϕ and μ. For the right-angled corner considered in this chapter, λ_s is given by the solution to [71]

$$\left[\sin^2\left(\frac{\pi\lambda_s}{2}\right) - \lambda_s^2\right]\cos(\pi\lambda_s) + \frac{1}{2}\sin^2(\pi\lambda_s) + \mu\lambda_s(1+\lambda_s)\sin(\pi\lambda_s) = 0. \tag{4-6}$$

If the slip condition is met, the interfacial stresses close to the corner are given by [30]

$$p(x) = K_s x^{\lambda_s - 1} \tag{4-7a}$$

$$q(x) = \mu K_s x^{\lambda_s - 1} \tag{4-7b}$$

where K_s is a stress-intensity factor that depends on the geometry and loads.

Coulomb slip does not resolve the issue of singular stresses. Theoretically, even if slip occurs, the shear stresses are infinite at the corners. Obviously, in practice, the stresses are limited by the finite strength of the interface. The question addressed in this chapter, is the extent to which the assumption of a finite interface strength affects the slip and wear conditions at the corner of a contact. This is examined by adapting the concept of cohesive-zone models for interfacial fracture, where the introduction of finite strengths

allows smooth transitions between regimes in which singular elastic fields dominate (albeit, limited by the finite strengths), and regimes where these fields provide very poor descriptions of interfacial mechanics.

3.2.3 Cohesive zones

Linear-elastic fracture mechanics is predicated on an assumption that the only interfacial property controlling fracture is the interfacial toughness. Cohesive-zone models incorporate a cohesive strength into the description of the interface. Mode-II cohesive laws provide an analogue for sliding problems without adhesive bonding. For a homogenous system in plane stress, a nominal mode-II fracture length can be defined as [57, 72, 73]

$$\xi_{II} = \frac{\bar{E}\Gamma_{II}}{\hat{\tau}} \tag{4-8}$$

where $\bar{E}$ is the modulus, and Γ_{II} is the mode-II toughness of an interface. If the nominal fracture length is small compared to any appropriate geometrical length, then the toughness controls crack propagation, and the interfacial stresses follow the elastic stress field close enough to the crack tip for the singularity to be experienced. If the nominal fracture length is large compared to any appropriate geometrical length, then the cohesive strength controls crack propagation, and the interfacial stresses are essentially uniform along much of the interface.

If one assumes there is no fracture associated with slip, the concept of a nominal fracture length is not useful, because Γ_{II} isn't defined. However, the concept of a fracture length has been generalized to the notion of an instantaneous cohesive length, which has

meaning at any point during the loading of an interface [55, 57]. For mode-II cracks, this instantaneous cohesive length is given by

$$\xi_{II} = \frac{\bar{E}^* \delta_s^2}{\mathcal{W}_{IIo}} \tag{4-9}$$

where $\bar{E}^*$ is the effective modulus of two materials contacting across an interface (which is E for the plane-stress, homogeneous case considered here[1]), δ_s is the slip distance at the crack tip (defined as the point where the shear tractions go to zero), and $\mathcal{W}_{IIo}$ is the work done in sliding (per unit area) by the shear tractions at the crack tip.

It appears that this definition of an instantaneous cohesive length should be useful for slip problems, since there is no reference to fracture. In particular, if a slip displacement of magnitude δ_s occurs at a critical shear stress of $\hat{\tau}$, the instantaneous cohesive length is given by

$$\xi_{II} = \frac{\bar{E}^* \delta_s}{\hat{\tau}} \tag{4-10}$$

The instantaneous cohesive length can be compared to the smallest relevant dimension of the system, to give a cohesive-length scale. By analogy to fracture mechanics, the magnitude of this cohesive-length scale is expected to determine whether slip can be considered to be small-scale (and controlled by elasticity), or not. If the ratio is significantly smaller than unity, it is expected that a portion of the elastic stress field will exhibit the singularity appropriate to the geometry of the corner. If the ratio is larger, it is expected

[1] $\bar{E}=E$ in plane stress and $E/(1-\nu^2)$ in plane strain, where ν is Poisson's ratio. In the fracture literature, it makes sense to define $\bar{E}^*=2\bar{E}_1\bar{E}_2/(\bar{E}_1+\bar{E}_2)$, where the subscripts refer to the materials on either side of an interface, so $\bar{E}$ is recovered in the homogeneous case.

that the stresses will be constant over a relatively large portion of the interface. These concepts will be illustrated in the results that follow.

3.3 Numerical model

The results in this chapter were generated using a finite-element model to calculate the stresses and slip along an interface near a sharp corner. The geometry and mesh used is shown in Figure 3-2. It is a plane-stress model consisting of a rectangular block of height, h, and length, l, which we will call the slider, in contact with a large substrate with the same elastic modulus E. The exterior angle between the block and substrate is 90°. Attention was focused on the left-hand corner of this geometry (the portion of the interface in which the two objects always remained in contact). The aspect ratio of the slider was $l/h = 20$, and we confirmed that this was large enough for the solutions that are presented to be unaffected by the right-hand boundary. We also confirmed that substrate was deep enough for the effects of the bottom boundary (which was constrained in all directions) were negligible within a reasonable level of numerical error. The absolute values of the parameters were varied to explore the utility of the non-dimensional groups used. In the results that are presented, only the non-dimensional groups that affect the results are reported.

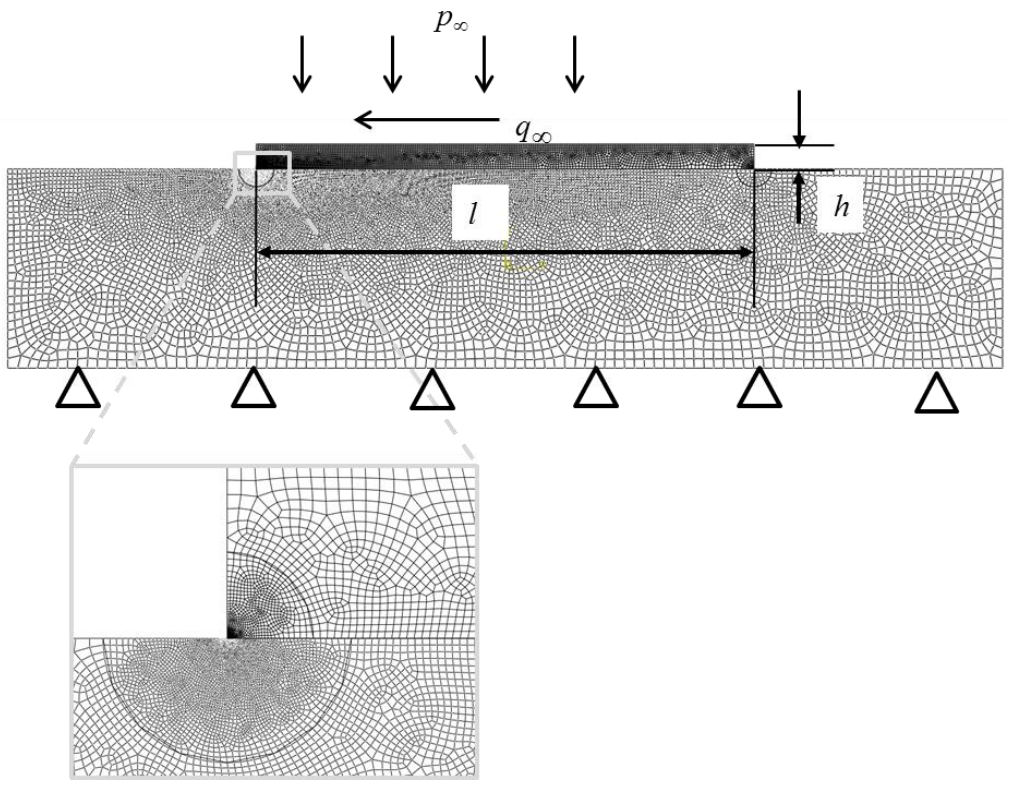

Figure 3-2: The finite-element model for simulations. The bottom figure shows a magnified view of the mesh around the corner.

The block was subjected to a uniform distributed normal pressure, p_∞, and a uniform distributed tangential stress, q_∞. The normal pressure was applied first as a pre-load, and the tangential stress was then applied to explore the subsequent slip. The coefficient of friction μ was varied to explore both stick and slip regimes as predicted by Coulomb's law. The cohesive strength of the interface, $\hat{\tau}$, was given an infinite value when exploring Coulomb friction, or a finite value when exploring the effect of a cohesive strength. In all cases, it was assumed that the contacting bodies were perfectly elastic, and the only non-linear effects were associated with slip at the interface.

The simulations were performed using the commercial finite-element package ABAQUS. Four-node, bilinear, coupled temperature-displacement elements (CPE4T)

were used. Standard options available in the package were used for the contact elements. A master-slave contact was defined along the contact interface; in every time increment, the slave nodes were adjusted so that there was no penetration between the contact surfaces. The contact was formulated according to the "surface-to-surface" option. The particular method for the discretization was set to the "surface-to-surface" option, in which the contact conditions are enforced over neighboring nodes. The slip conditions for Coulomb friction and a finite shear strength were also set within the usual options available in the program. However, since very small amounts of relative motion across an interface can evolve from the finite-element calculations, a separate sub-routine was used to compare the values of q and q/p /to $\hat{\tau}$ and μ and to establish whether these displacements were associated with slip or numerical uncertainty. This was useful for determining slip-stick boundaries.

In order to capture the singular stress field correctly, we refined the mesh around the contact corners using a bias seeding. The mesh had 18463 elements, with the smallest elements being refined to a value of $0.002h$. The validities of the finite element model and the mesh refinement were confirmed by ensuring that the magnitudes of the singularities for the stress fields and the ratio between the contact pressure and shear agreed with the predictions of elasticity theory for a fully-stuck interface.

Validation that the mesh was fine enough was achieved by plotting the stresses along the interface on a log-log plot, and comparing the slope of the line close to the interface with the expected dominant singularity from analytical solutions. For example, the numerical solutions resulted in a predicted singularity of $K_I = 0.544 \pm 0.003$ for a non-slipping interface, and $\lambda_s = 0.651 \pm 0.001$ for a slipping interface with $\mu = 0.27$. These are in

excellent agreement with the expected values of 0.5445 and 0.6503, respectively, and confirms that the quality of our mesh and technique is acceptable to within a very reasonable level of uncertainty. Once it was confirmed that the strength of the singularity in the numerical solutions was correct, the values of the stress-intensity factors could also be found from the plots. For example, when $q_\infty / p_\infty = 0.25$, these values are $K_I h^{\lambda_I - 1} / p_\infty$ = 0.558±0.003, and $K_s h^{\lambda_s - 1} / p_\infty$ = 0.796±0.001 for μ= 0.27.

3.4 Results and discussion

3.4.1 Larger coefficients of friction

The distributions of the shear and normal stresses along the interface are shown in Figure 3-3 for a case in which $\mu > 0.543$, so slip would not occur if only Coulomb friction acted. Since $l / h \gg 1$ in these calculations, the characteristic length scale used to normalize the parameters in these plots is h. The plot labelled ξ_{II}/h=0 corresponds to the limiting case of an infinite shear strength. Since there is no slip, this stress field corresponds to the bonded case. The straight-line portion of this reference curve has a slope that is in excellent agreement with the expected singularity of λ_I= 0.5445. The curves for the two non-zero values of ξ_{II}/h were calculated using different values of the applied stresses, keeping the values of both q_∞ / p_∞ and ξ_{II}/h constant. ξ_{II}/h was kept constant by trial and error by changing the value of q_∞/E, and then calculating the cohesive length from Eq. (4-10) using the slip distance calculated by the finite-element results. Provided that both q_∞ / p_∞ and ξ_{II}/h were kept constant, the plots of stress were co-incident. This indicates that the instantaneous cohesive-length scale provides a means of characterizing the slip.

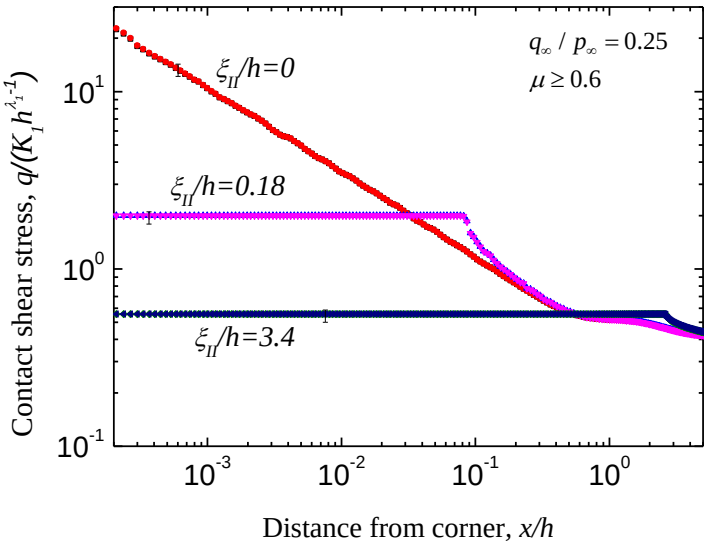
$q_\infty / p_\infty = 0.25$
$\mu \geq 0.6$
$\xi_{II}/h=0$
$\xi_{II}/h=0.18$
$\xi_{II}/h=3.4$
Contact shear stress, $q/(K_I h^{\lambda_1-1})$
Distance from corner, x/h

(a)

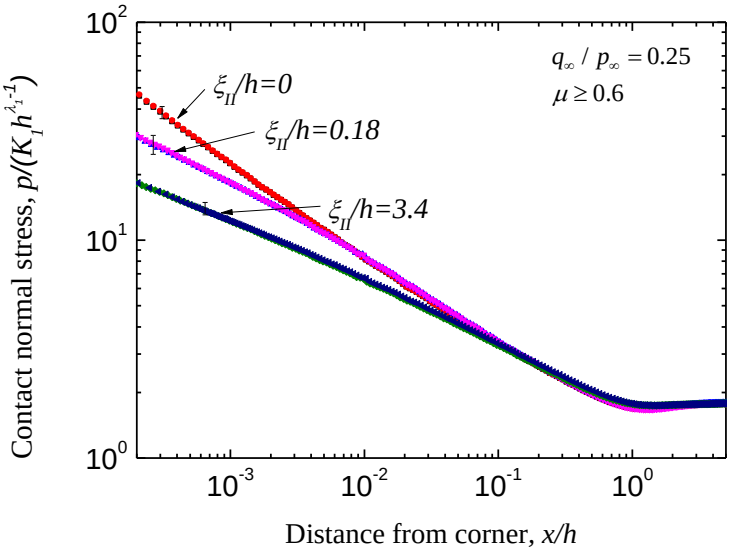
$q_\infty / p_\infty = 0.25$
$\mu \geq 0.6$
$\xi_{II}/h=0$
$\xi_{II}/h=0.18$
$\xi_{II}/h=3.4$
Contact normal stress, $p/(K_I h^{\lambda_1-1})$
Distance from corner, x/h

(b)

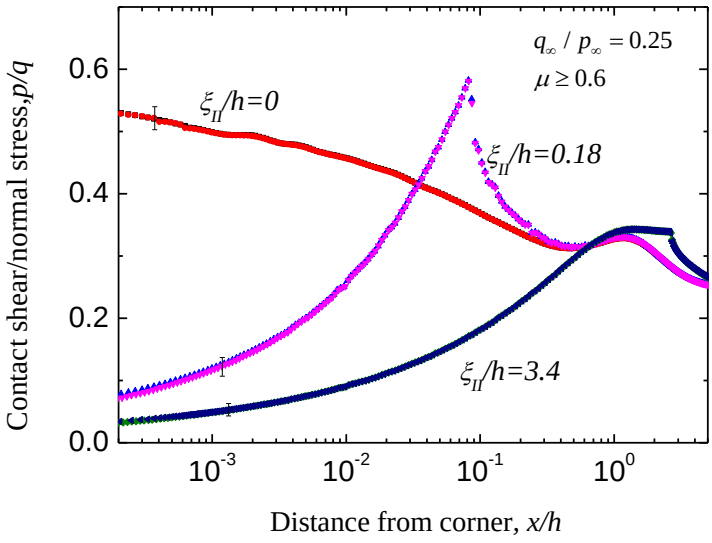

(c)

Figure 3-3: Interface stress distributions with $\mu = 0.6$. No Coulomb slip occurs since $\mu > 0.543$. Any slip is entirely caused by the shear stress exceeding a finite interfacial strength.(a)Shear stress distribution along the interface for three representative cases:(i) no slip ($\xi_{II}/h = 0$),(ii) small-scale slip ($\xi_{II}/h = 0.18$), and (iii) large-scale slip ($\xi_{II}/h = 3.4$).(b)Normal stress distributions along the interface for the same three values of ξ_{II}/h. (c)The corresponding distributions of the ratio between the shear and normal stresses.

Figure 3-3 shows that when the instantaneous cohesive-length scale, ξ_{II}/h, is reasonably small, slip is embedded within the singular elastic field, so that the slip can be described as being small-scale. The instantaneous cohesive-length scale increases as the extent of slip increases, and large-scale slip occurs when it extends so far that there is no region where the stresses exhibit singular behavior. As expected, outside the slip region, the shear stresses follow the far-field elastic solution. This behavior is exactly what is expected by analogy to cohesive-zone models for cracks with similar instantaneous cohesive-length scales. While the shear stresses are limited by the interfacial strength near the corner, the normal pressures still show singular fields, even in the slip region (although the singularity is weaker than predicted by the no-slip condition). In practice, of course, these normal stresses will be limited by yield of the contacting materials.

Whether there would be any regime of Coulomb-controlled slip or not can be seen by looking at the ratio of q/p, as plotted in Figure 3-3(c). There is a peak in this ratio at the edge of the slip regime. If the value of μ is greater than the magnitude of this peak, then the strength-controlled slip regime ends in a region of sticking. If the value of μ is smaller than the magnitude of this peak, there will be two regions of slip: one controlled by the interfacial strength, the other controlled by Coulomb's law. This peak rises from 0.543 to a maximum of 0.74±0.02 as ξ_{II}/h increases from zero to 0.005, the peak then falls with a further increase in the cohesive-length scale.

3.4.2 Smaller coefficients of friction

Figure 3-4 shows similar plots to those of Figure 3-3, but with a much smaller friction coefficient of $\mu = 0.27$. This is below the critical value of 0.543 for this geometry, so Coulomb slip can occur. In these plots the stresses have been normalized by the stresses for the singular field with slip, so that they are of the form of $q / K_s h^{\lambda_s - 1}$, where λ_s=0.6503 is the appropriate singularity for slip with $\mu = 0.27$ (see Eq. (4-7)).

In this case, since there is both Coulomb slip, and finite-strength slip, we need to distinguish between the two regions so as to obtain the appropriate value of δ_s needed to evaluate ξ_{II}/h from Eq. (4-10). The regions where slip is controlled by $\hat{\tau}$ can be identified from the regions of constant shear stress in Figure 3-4(a). The regimes of Coulomb slip can be identified from the regions where the ratio of $q/p = \mu$ in Figure 3-4 (c). Coulomb slip extended out to beyond the limits shown in Figure 3-4 (c), but this was always embedded in the elastic field corresponding to a stuck (or bonded) interface, with no influence from the other boundary.

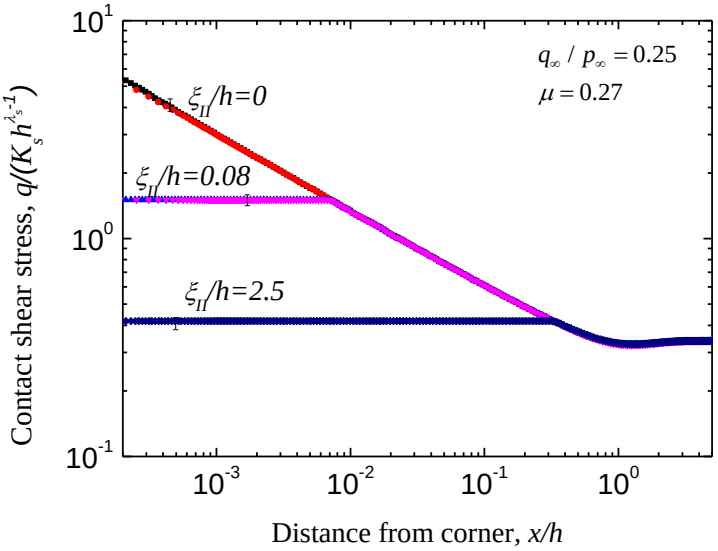
$q_\infty / p_\infty = 0.25$
$\mu = 0.27$
$\xi_{II}/h=0$
$\xi_{II}/h=0.08$
$\xi_{II}/h=2.5$
Contact shear stress, $q/(K_s h^{\lambda_s-1})$
Distance from corner, x/h

(a)

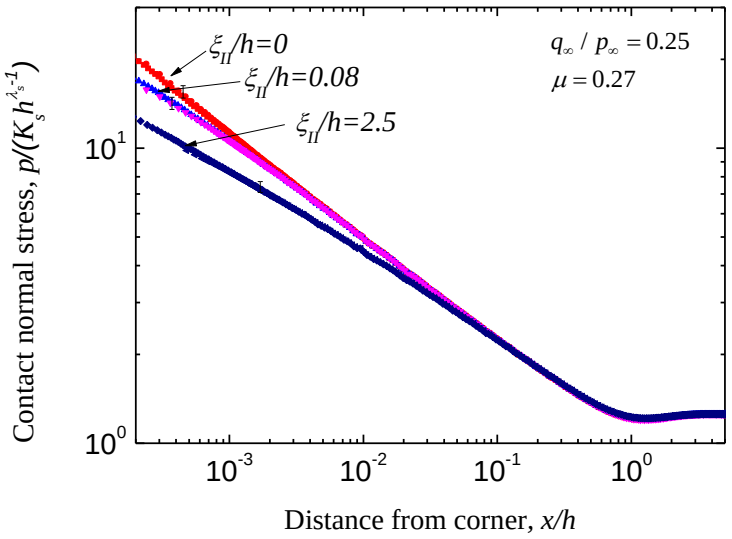
$q_\infty / p_\infty = 0.25$
$\mu = 0.27$
$\xi_{II}/h=0$
$\xi_{II}/h=0.08$
$\xi_{II}/h=2.5$
Contact normal stress, $p/(K_s h^{\lambda_s-1})$
Distance from corner, x/h

(b)

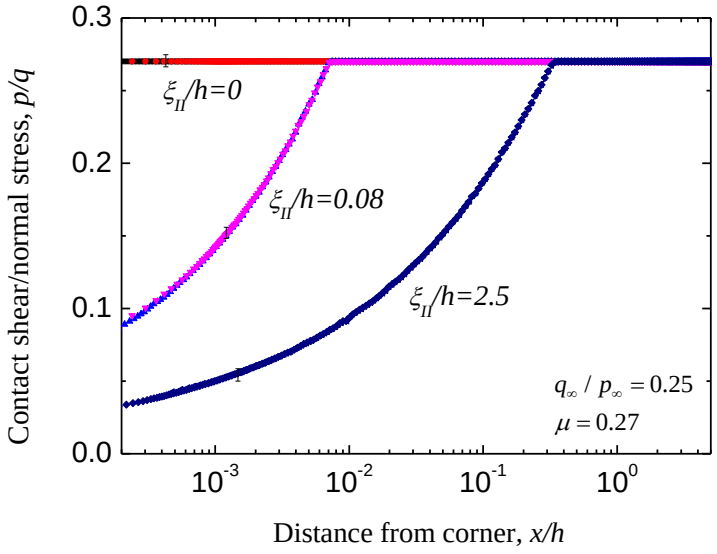

(c)

Figure 3-4： Interface stress distributions with μ = 0.27. The slip zone controlled by a finite interfacial shear strength is embedded in the Coulomb slip zone. (a)Shear stress distribution along the interface for three representative cases:(i) no slip (ξ_{II}/h = 0), (ii) small-scale slip (ξ_{II}/h = 0.08), and (iii) large-scale slip (ξ_{II}/h = 2.5).(b)Normal stress distributions along the interface for the same three values of ξ_{II}/h. (c)The corresponding distributions of the ratio between the shear and normal stresses.

Generally, there will always be a regime of strength-limited slip in the partial-slip zone near the corner of a contact. However, as discussed above, Coulomb slip can also occur just outside this region before the fully stuck zone is encountered. It is also possible for the strength-limited slip region to contact directly onto a stick region. These different types of behavior are illustrated in the map of

Figure 3-5, showing the effect of μ for one specific value of cohesive strength.

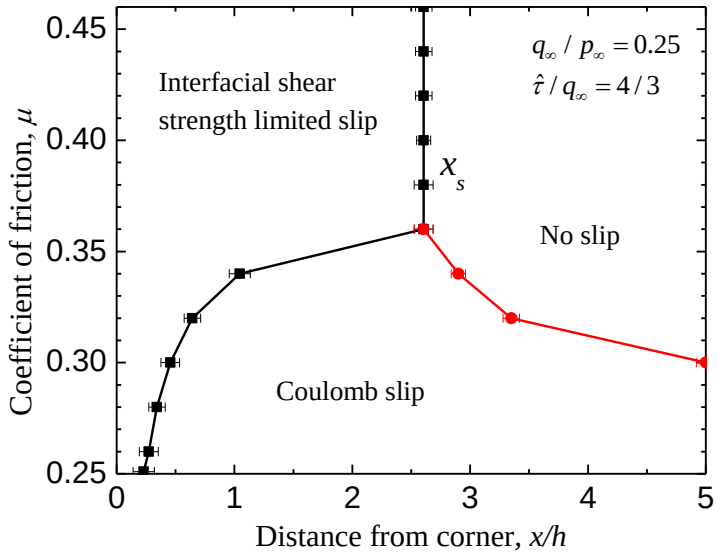

Figure 3-5: Slip mechanism map showing relationship between slip mechanisms as a function of μ and location. The interfacial shear strength and Coulomb's law dominate the slip zone sizes at high and low friction coefficients, respectively.

3.4.3 Sensitivity to corner geometry

One of the major effects of a cohesive zone in fracture is that it reduces the sensitivity to the details of any defects. Larger cohesive-length scales result in less sensitivity to any singularities that would arise from an elastic analysis, associated with reduced notch sensitivity [73]. In this section, we examine how a cohesive zone might affect the sensitivity of slip to the assumed details of a corner. This is done by examining the stress field and slip for three different models, each with the same macroscopic geometry of a contact with a 90° external angle (Figure 3-6). One of these models has a 90° external angle to the smallest scale of the numerical model. Another of these geometries has a small notch, so that the actual angle of contact with the interface is 45°. The last of these geometries has a smooth contact with the interface, formed by the arc of a circle meeting the interface tangentially. The calculations are performed for a coefficient of friction given by

μ=0.34 for all three geometries. The stresses for the three geometries are shown in Figure 3-7 for the case when there is an infinite shear strength, so slip is controlled by Coulomb friction only. The extent of slip can be seen most easily from Figure 3-7 (c), which shows the ratio of the shear to normal pressure along the interface. As can be seen in that figure, both the 90° and smooth corner exhibit Coulomb slip near the corner, with the 90° corner having a longer slip distance. The 45° corner exhibits interesting behavior of being stuck at the corner, but with a region of internal slip (an effect of the weaker singularity which dominates at intermediate distances from the corner still needs to be verified). The total slip at the corner for each of these three geometries is given by $\delta_o/h = 3.2\times10^{-5}$, 0 and 3.3×10^{-6}, for the 90°, 45° and smooth contacts, respectively.

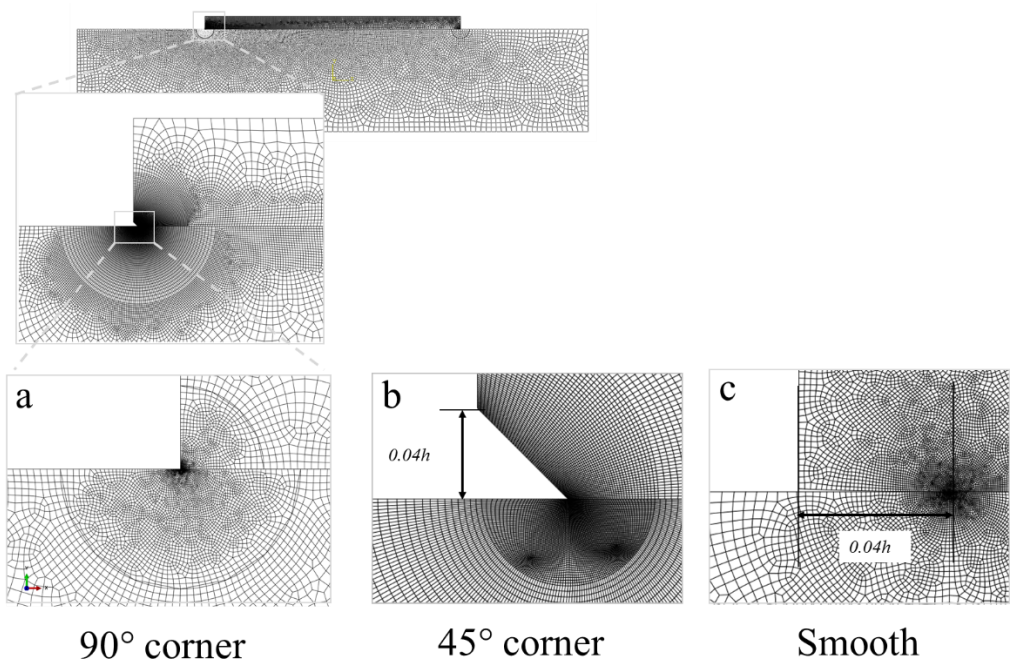

Figure 3-6: Three corners with the same macroscopic geometry as Figure 3-2: (a) a 90° external corner; (b) a 45° external angle for a depth of 0.04*h*; (c) a smooth corner formed by an arc of a circle of radius *h* meeting the interface at a tangent at a distance of 0.04*h* from the edge.

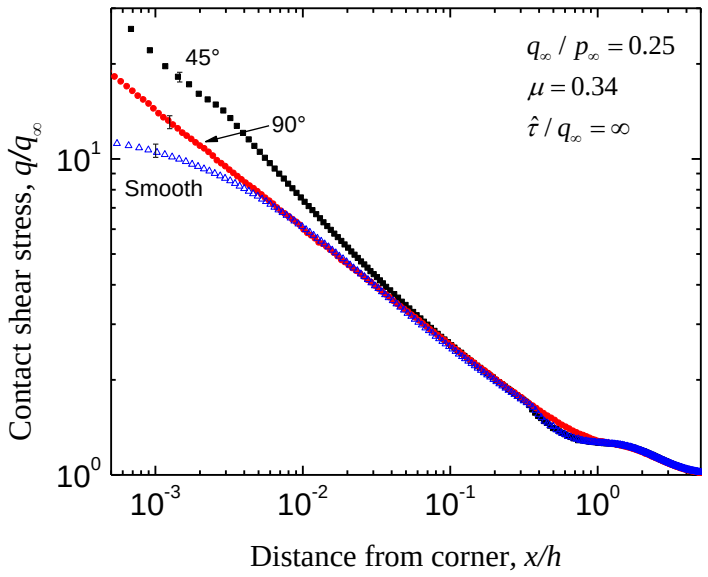
$q_\infty / p_\infty = 0.25$
$\mu = 0.34$
$\hat{\tau} / q_\infty = \infty$
45°
90°
Smooth
Contact shear stress, q/q_∞
10^0
10^1
10^{-3}
10^{-2}
10^{-1}
10^0
Distance from corner, x/h

(a)

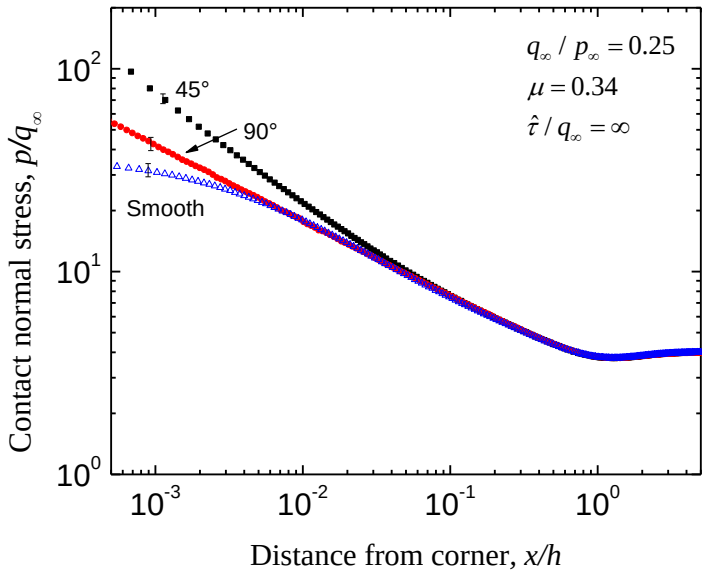
$q_\infty / p_\infty = 0.25$
$\mu = 0.34$
$\hat{\tau} / q_\infty = \infty$
45°
90°
Smooth
Contact normal stress, p/q_∞
10^0
10^1
10^2
10^{-3}
10^{-2}
10^{-1}
10^0
Distance from corner, x/h

(b)

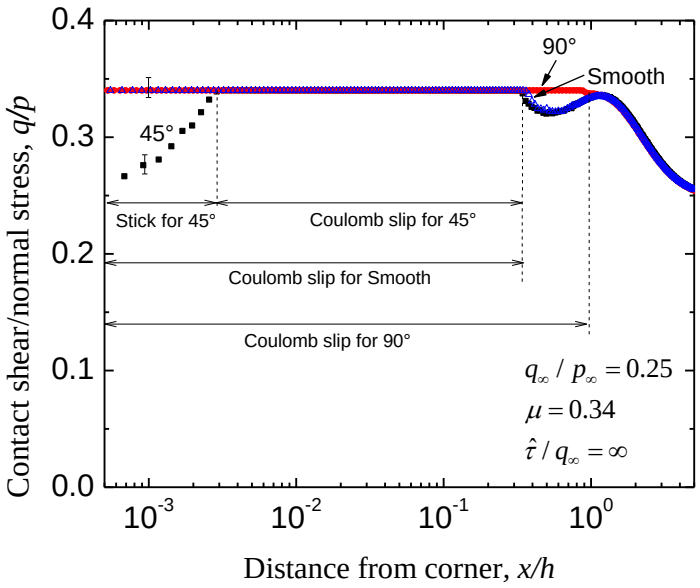

(c)

Figure 3-7: Plots of how the (a) shear stress, (b) normal pressure, and (c) ratio of shear stress to normal pressure vary along an interface for the three different corners of Figure 3-6, with a coefficient of friction given by μ = 0.34, q_∞ / p_∞=0.25, and an infinite shear strength.

The stresses for the three geometries are shown in Figure 3-8 for the case when there is a finite shear strength. The extent of slip can be seen most easily from Figure 3-8 (c), which shows the ratio of the shear to normal pressure along the interface. As can be seen in that figure, all three cases show similar behavior, with strength-limited slip near the corner and Coulomb-limited slip further away, with the total slip length being similar in all three cases. Furthermore, the total slip at the corner for each of these three geometries are also very close, being given by $\delta_o/h = 5.3\times10^{-5}$, 3.9×10^{-5} and 3.7×10^{-5}, for the 90°, 45° and smooth contacts, respectively. With the assumption of an interfacial shear strength, the slip conditions are much less sensitive to the precise details of the contact, even though the cohesive-length scales were relatively low at ξ_{II}/h =0.13, 0.24 and 0.21 for the three cases.

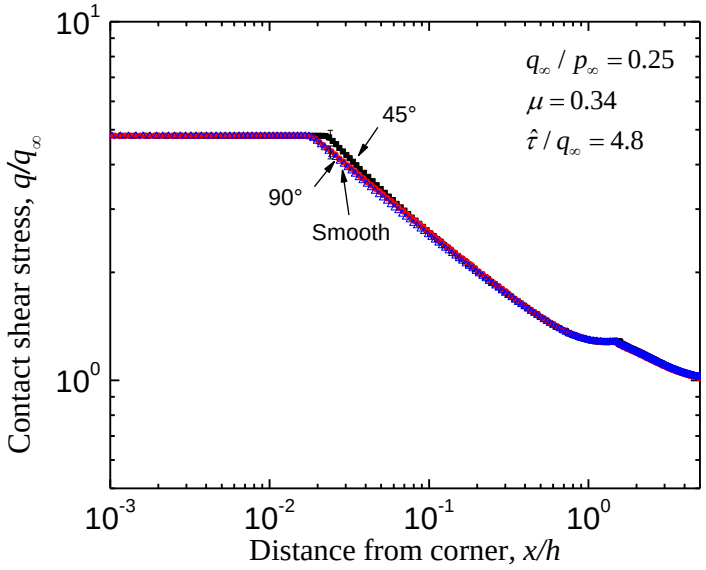
10^1
10^0
10^{-3}
10^{-2}
10^{-1}
10^0
Contact shear stress, q/q_∞
Distance from corner, x/h
$q_\infty / p_\infty = 0.25$
$\mu = 0.34$
$\hat{\tau} / q_\infty = 4.8$
45°
90°
Smooth

(a)

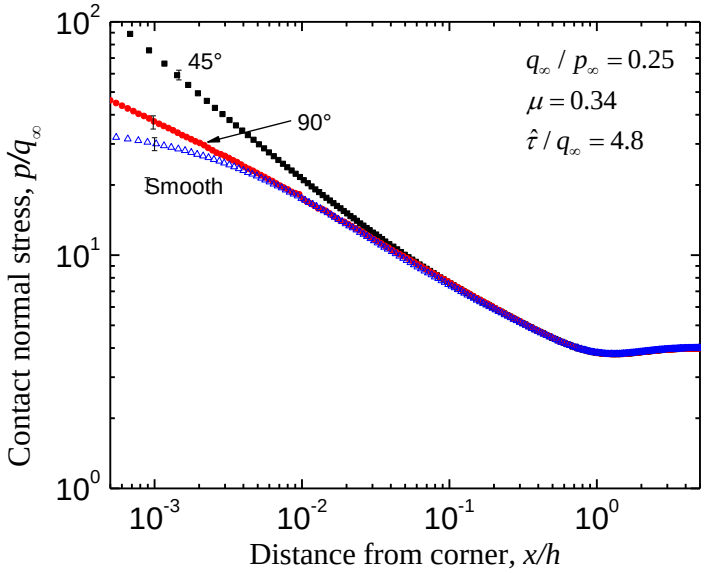
10^2
10^1
10^0
10^{-3}
10^{-2}
10^{-1}
10^0
Contact normal stress, p/q_∞
Distance from corner, x/h
$q_\infty / p_\infty = 0.25$
$\mu = 0.34$
$\hat{\tau} / q_\infty = 4.8$
45°
90°
Smooth

(b)

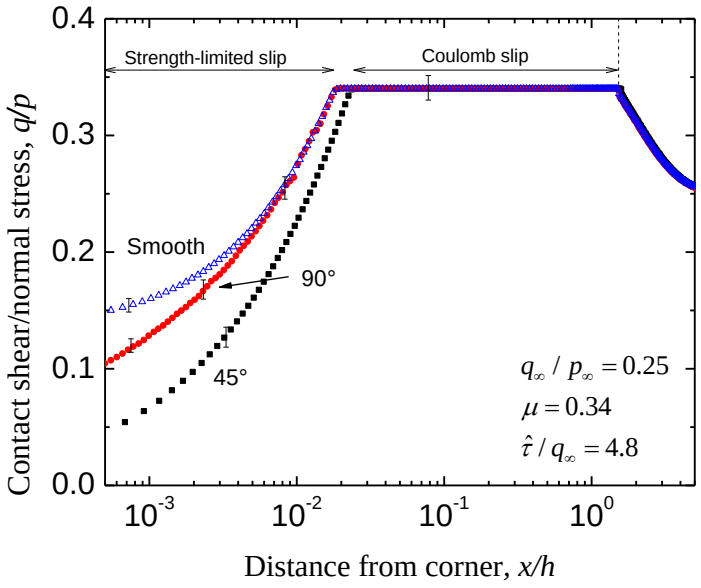

(c)

Figure 3-8: Plots of how the (a) shear stress, (b) normal pressure, and (c) ratio of shear stress to normal pressure vary along an interface for the three different corners of Figure 3-6, with a coefficient of friction given by μ =0.34, q_∞ / p_∞=0.25, and $\hat{\tau} / q_\infty$ =4.8.

3.4.4 Effects of interfacial shear strength on wear propagation

Partial-slip can cause wear. This modifies the profile of the contact surfaces and redistributes the stress. Studies have shown that if Coulomb's law is assumed for friction, the stick-slip boundary does not move as wear progresses [35, 74]. This can be rationalized from a fracture-mechanics perspective. The local wear in the slip region evolves to a crack-like feature. This results in the shear stresses and normal pressure having an inverse square-root dependence ahead of the wear scar, with the mode-I and mode-II stress-intensity factors being proportional to the applied shear and normal tractions. This means that $q/p = q_\infty/p_\infty$, so that if the conditions for macroscopic slip are not met (i.e., $q_\infty/p_\infty < \mu$), partial-slip conditions ahead of the wear scar will not be met either. This is of practical importance, because it would imply that a wear scar cannot proceed beyond the initial stick-

slip boundary. However, as will be shown in the calculations that follow, a finite shear strength always results in slip ahead of a crack-like feature, so an assumption of a finite interface strength can result in the propagation of a wear scar across an interface.

To demonstrate this effect, we generated a worn contact interface and simulated a slip problem. As an example, we used a model with the dimensions and loading conditions of Figure 3-2. The friction coefficient was set equal to 0.38, and the shear strength was switched on or off by setting $\hat{\tau} / q_{\infty}$ equal to either 3 or ∞. These values were chosen to establish a relatively small initial slip zone. We then developed a wear scar by modelling wear according to Archard's law [45]:

$$w = \alpha p \delta_s ; \tag{4-11}$$

where α is the wear coefficient, and δ_s is the nodal slip.

We analyzed one cycle of increasing q_{∞} from zero up to a maximum value, and back again, integrating the slip and normal stress for each node in the contact region to compute the wear during a single cycle. A wear scar typically forms during many loading cycles, with each cycle changing the morphology slightly. We ignored this aspect of the problem for the purposes of this study, and accelerated the process by scaling the wear coefficient, A, so that contact was lost within the wear scar after just one cycle of loading. We computed the normal pressure and slip distance at each node in the contact region during each increment of a single cycle. We then used Eq. (4-11) to compute the integrated wear for each node, and then modified the mesh at the interface to create a wear scar, using the updating method of fictitious eigenstrains described in Ref. [16].

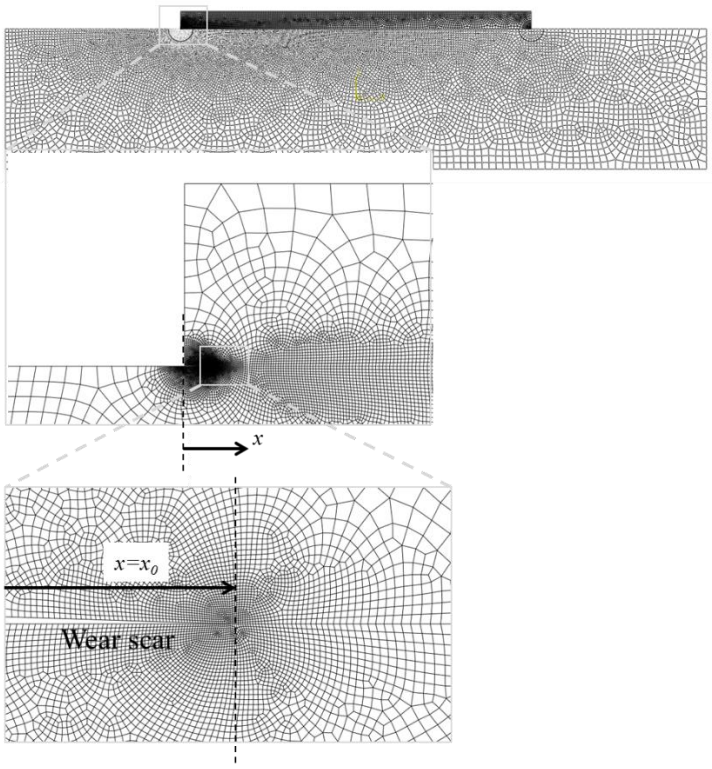

Figure 3-9: The nodal coordinates in the slip zone is adjusted so that it lose contact completely in that zone and the mesh around the stick-slip boundary is refined.

A wear scar typically forms during many loading cycles, with each cycle changing the morphology slightly. We ignored this aspect of the problem for the purposes of this study, and investigated the limit of the process by scaling the wear coefficient, A, so that contact was completely lost within the slip zone after just one cycle of loading. Using the new geometry with a wear scar at the interface (Figure 3-9), we examined the stress state ahead of the scar upon increasing q_∞ back up to its maximum value.

The distributions of shear stress, normal stress and the corresponding ratio of the shear and normal stress are shown in Figure 3-10. With an infinite shear strength, corresponding to Coulomb slip, there is a crack-like singularity (inverse root) for the stresses. The ratio of the stresses in the singular field scales with q_∞/p_∞, as might be expected from a

fracture mechanics of the crack problem. This means that if the coefficient of friction is high enough to prevent general slip along the interface, it will also prevent partial-slip ahead of the wear scar. This is consistent with the analysis of Ref. [17], and may suggest a general result that the stick-slip boundary does not move in response to wear if only Coulomb friction is assumed.

However, when the calculations are repeated with a finite shear strength, with $\hat{\tau} / q_\infty$ = 3, slip occurs ahead of the wear scar. Again, this is expected by analogy to cohesive zones at crack tips. This extended zone of partial-slip means that a wear scar will propagate across the interface, and provides an important example of why the introduction of finite shear strengths can have such an important impact for wear at the corners of contacts.

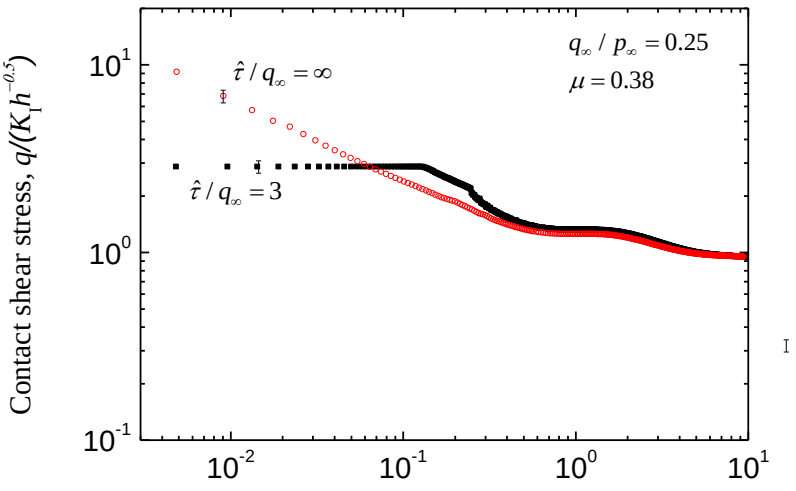

(a)

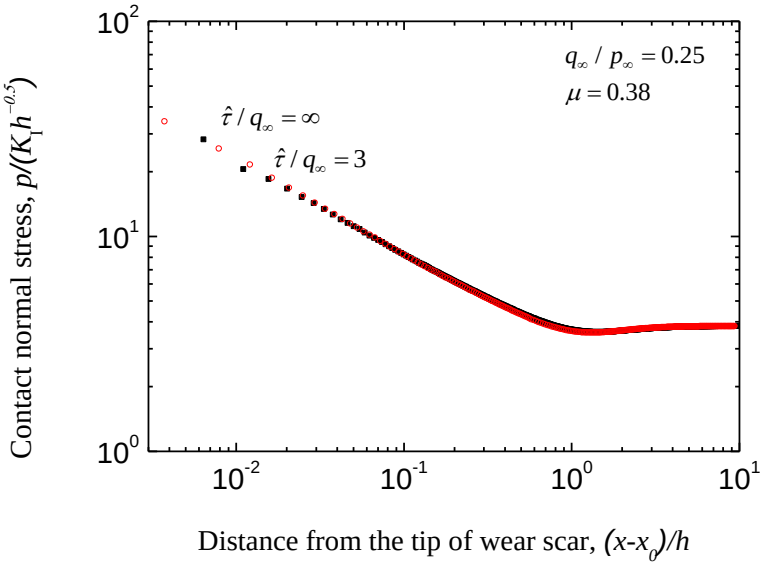

(b)

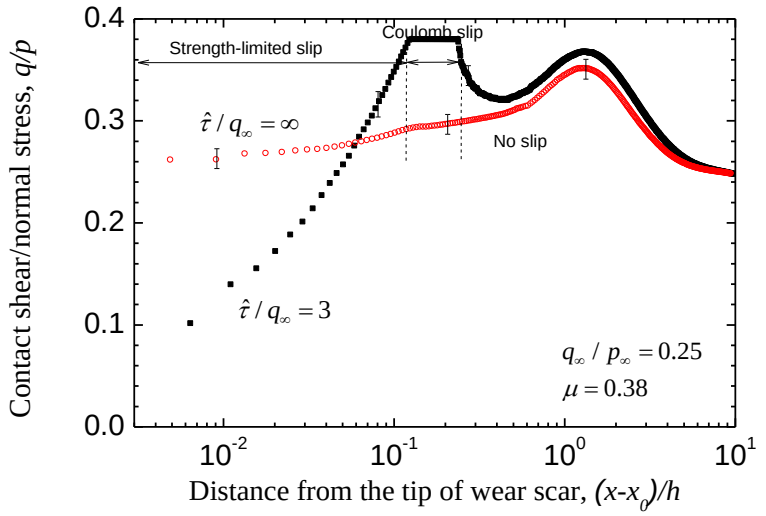

(c)

Figure 3-10: Interface stress distributions with $\mu = 0.38$ on a worn interface (the initial slip zone lose contact completely). (a) Shear stress (b) Normal stresses (c) The corresponding distributions of the ratio between the shear and normal stresses. An interfacial shear strength controlled slip zone exists around the stick-slip boundary and a singular coulomb friction law is not capable to predict it. Although the slip zone size is small in the beginning, the wear causes redistribution of stress and the slip zone grows to the interior region.

3.5 Conclusions

The integration of a finite interfacial strength with a Coulomb friction law has a significant influence on slip and wear at the corner of a contact. It is possible to define an instantaneous cohesive length in terms of the modulus, slip distance and interfacial strength. A comparison of this length with a characteristic geometrical scale gives an indication of when small-scale conditions are appropriate, and the stress field approaching the corner can be reasonably approximated by the singular field. In particular, when the instantaneous cohesive-length scale, ξ_{II}/h is small, the stresses along the interface near the corner are uniquely described by

$$\frac{qh^{1-\lambda}}{K} = f\left(\frac{x}{h}, \frac{\xi_{II}}{h}, \mu\right), \tag{4-12}$$

where K and λ are functions of μ. For larger values of ξ_{II}/h, the ratio of q_∞/p_∞ is no longer captured by the stress-intensity factor, so this becomes an additional non-dimensional group that affects the stresses. Cohesive zones have the advantage of capturing the essence of the elastic solutions where they are appropriate, while describing behavior in the regimes and length scales where elastic solutions are not valid. As with mode-II fracture, the use of cohesive zone concepts reduces the sensitivity of the problem to local details of the singular stress field. Depending on the scale at which a corner is described, the singular fields and corresponding description of slip along the interface can be very different for geometries with similar macroscopic descriptions at a larger scale. The introduction of a cohesive length, reduces this sensitivity.

If there is partial-slip, the resulting wear will cause a crack-like geometry to evolve along the interface up to the stick-slip boundary. However, with the assumption of Coulomb friction, the wear scar will not evolve beyond the original partial-slip boundary, as has been established for the Hertz contact problem [69], in which the normal stresses are not singular, but the shear stresses are [17]. The introduction of a finite interfacial strength results in the slip-stick boundary moving with the propagation of wear. This is expected to be of significance to models of wear, since it allows wear to propagate from the corner of a macroscopically non-slipping contact.

Chapter 4

Effects of plasticity on wear propagation

4.1 Introduction

As mentioned in Chapter 3, GTRF wear usually initiates from the partial-slip around the contact edges. The focus of Chapter 3 is partial-slip around a sharp contact edge, i.e. a 'complete' contact; in this chapter we focus on a contact interface with a smooth edge, which is termed an 'incomplete' or non-conforming contact. This type of contact is commonly noticed for the transverse slip of the grid-to-rod interface as well as many other engineering applications [58, 75-77]. In this `incomplete' contact problems, the normal tractions decrease smoothly to zero at the contact edge [75]. However, when the contact is subjected to a cyclic shear load, regions of reversed microslip are developed at the edges of the contact area and the resulting wear leads to a redistribution of stress [17, 33-35].

Hills and Fellows [78] showed that the boundary between the stick and slip regions does not change during this wear process. This result can be proved rigorously for any problem to which the Ciavarella-Jäger theorem [75, 79] applies and is also observed in numerical solutions [34-36]. Under these conditions, wear will eventually progress to the

state where the contact pressures are negligible in the slip region. The system then becomes elastically similar to a crack, with consequent square-root singularities in the normal and shear tractions in the stick region, as shown in Figure 4-1.

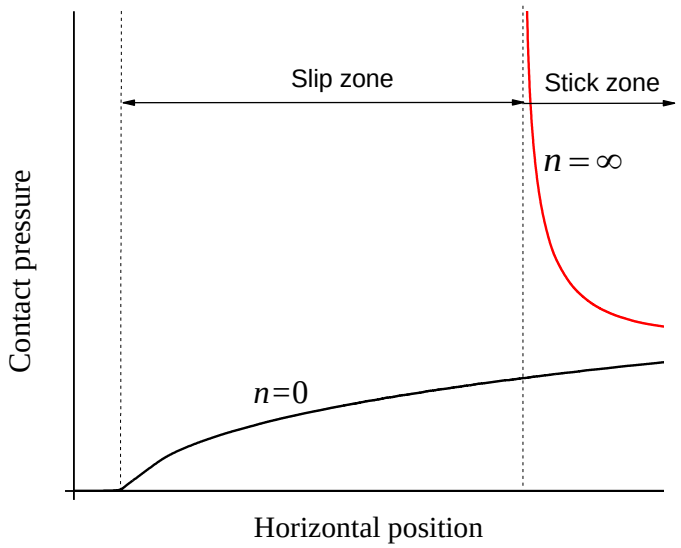

Figure 4-1: The initial contact pressure decreases to zero smoothly. However, after a large number n of loading cycles, the material in the slip zone is worn away and the contact pressure near the stick slip boundary becomes elastically singular.

In most practical cases, this process will be limited by plastic deformation near the incipient crack tip, and this in turn may affect the wear process and the evolution of contact pressure. This is the effect to be explored in the present chapter. It has potentially important consequences for the prediction of the initiation and propagation of fretting fatigue cracks [58, 74, 77, 80-82].

In a fuel assembly as well as many other contact systems, the intention is to provide sufficient normal force to approximate a completely stuck situation, so that the resulting cyclic slip zones are small. In particular, if these zones are sufficiently small compared with the other linear dimensions of the problem, the local stress fields can be completely

characterized in terms of appropriate generalized stress-intensity factors [83]. This procedure is similar in concept to the `small-scale yielding' criterion in linear elastic fracture mechanics (LEFM) [84] and has been shown to be very successful in correlating fretting fatigue life [47].

In this chapter, we shall use this characterization in the context of a finite-element model to make fairly general predictions of the effect of plastic deformation on the evolution of wear and contact tractions, and on the accumulation of plastic strain in a fretting configuration. In this way, the results of this chapter can be projected to various geometry designs of the spacer grid that has a smooth contact edge.

4.2 Methodology

Figure 4-2 shows the edge of the contact between two smooth bodies subjected to a constant normal force P and a tangential force that oscillates between $\pm Q$, where $Q < \mu P$ and μ is the coefficient of friction, which is assumed to be the same under static and dynamic conditions. We assume that the line of action of the tangential force lies at the contact interface, so that no moment is induced. We also assume that the materials of the two bodies are similar, so Dundurs' constant $\beta=0$ [46] and hence the slip displacements have no effect on the contact pressure distribution.

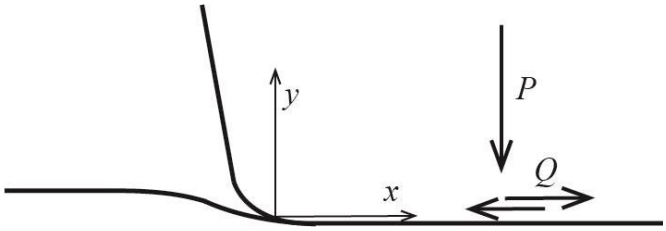

Figure 4-2: A contact pair with a smooth contact edge. The indenter is subjected to a normal force P and oscilating force Q , The coordinate x is measured from the edge of the contact.

4.2.1 Asymptotic elastic fields

Following Dini and Hills [83], we characterize the normal tractions local to the contact edge in the absence of wear by the expression

$$p(x) = C\sqrt{x}\,, \tag{5-1}$$

where C is a constant that depends on the external loads and the macroscopic geometry. If the length d of the slip zone is sufficiently small compared with the macroscopic length dimensions, the local tangential tractions can then be written as

$$q(x) = \pm\mu C\left(\sqrt{x} - \sqrt{x-d}\right) \tag{5-2}$$

[83], where the sign depends on the direction of slip and the square roots are interpreted as zero in any region where their arguments are negative.

We assume that the slip zone length d is sufficiently small that there exists a range in which $x \gg d$, but $x \ll D$, where D is a characteristic dimension of the macroscopic contact problem. The slip zone has little effect on the shear tractions in this range, so these can be characterized by a mode-II stress-intensity factor K_{I} [74, 75, 83, 85], where

$$q(x) = \frac{\mu d C}{2\sqrt{x}} = \frac{K_{\mathrm{II}}}{\sqrt{x}}\,. \tag{5-3}$$

Notice that this definition differs by a numerical factor of 2π from that conventionally used in fracture mechanics.

The parameters C and K_{I} are determined only by the macroscopic geometry and the external loading, and hence could be determined from a numerical model of the system under `full stick' conditions. Eq. (5-3) then provides a condition

$$d = \frac{2K_{II}}{\mu C} \tag{5-4}$$

for the length of the slip zone, and hence for the local shear traction distribution, through Eq. (5-2). Eq. (5-4) can be used to define a dimensionless coordinate $\xi = x/d$ and a corresponding normalization for tractions can be defined as $\tilde{p} = p/\sigma_0$, $\tilde{q} = q/\sigma_0$, where the stress measure

$$\sigma_0 = \sqrt{\frac{2K_{II}C}{\mu}} \tag{5-5}$$

With this normalization, all elastic problems are condensed into a single problem, subject only to the `small slip zone' approximation.

4.2.2 Asymptotic elastic fields

Ciavarella [75] and Jäger [79] have shown that when an elastic contact is loaded first by a normal load P and then by a tangential load Q, the stick region A_{stick} is coextensive with the contact region A^* for a fictitious normal load P^* given by

$$P^* = P - \frac{Q}{\mu}. \tag{5-6}$$

This result also applies at the extreme points where the tangential load is $\pm Q$, during completely reversed periodic loading.

It follows that A_{stick} depends only on the profile of the contacting bodies inside A_{stick}, and this cannot be affected by wear, since wear occurs only where there is slip. Thus, the extent of the stick region remains unchanged throughout the process [17, 78]. By contrast, material is worn away in the slip region and eventually, if the process is not limited

by yielding, the entire load P will be carried by the stick region. The pressure distribution in this limiting state will comprise the superposition of (i) $p^*(x)$ due to the fictitious load P^* and (ii) a 'flat punch' distribution due to the additional load $(P-P^*)=Q/\mu$ transferred to A_{stick} from the worn region. This latter contribution will lead to a singular traction at the edge of the stick zone, whose magnitude can be characterized by a mode-I stress-intensity factor K_I. Furthermore, since the Green's functions for normal and tangential loading of the half plane are identical in form, Eq. (5-6) implies that

$$K_{\mathrm{I}} = \frac{K_{\mathrm{II}}}{\mu} \tag{5-7}$$

4.2.3 The limiting wear profile

In order to reach this limiting state, material must have been worn from the slip region, corresponding to the overlap that would be implied by the limiting solution if there had been no wear and interpenetration of the bodies were permitted.

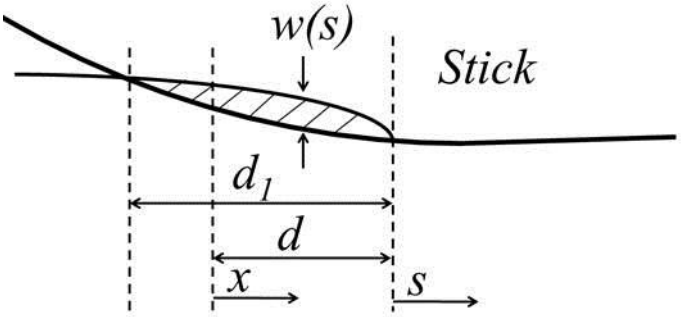

Figure 4-3: Overlapping material (shaded) that must be removed in the limiting state.

This situation is illustrated in Figure 4-3, where the origin of coordinate s is now taken at the edge of the stick region, so $s=x-d$. For $s>0$, the asymptotic form of the contact pressure is

$$p(s) = \frac{K_{\mathrm{I}}}{\sqrt{s}} + C\sqrt{s} \tag{5-8}$$

where we note that the parameter C defining the strength of the bounded term is not significantly changed between loads P and P^* as long as the slip zone is sufficiently small.

Application of Williams' asymptotic technique to these fields, shows that the necessary wear $w_\infty(s)$ in $s<0$ to avoid interpenetration is

$$w_\infty(s) = \frac{4K_{\mathrm{I}}(-s)^{1/2}}{E^*} - \frac{4C(-s)^{3/2}}{3E^*} = \frac{4K_{\mathrm{II}}(-s)^{1/2}}{\mu E^*} - \frac{4C(-s)^{3/2}}{3E^*} \tag{5-9}$$

where E^* is the composite modulus (Johnson, 1985), which for similar materials is

$$E^* = \frac{E}{2(1-\nu^2)} \tag{5-10}$$

where E and ν are respectively Young's modulus and Poisson's ratio.

Eq. (5-9) shows that $w(s)$ is positive in a region of length

$$d_1 = \frac{3K_{\mathrm{II}}}{\mu C} \tag{5-11}$$

and this is exactly 50% larger than the original slip length d from Eq. (5-4). In other words, as wear occurs, the bodies move closer together, so that the contact region grows.

The limiting wear profile (5-9) can be written in terms of the coordinate $x=s+d$ of Figure 4-3 as

$$\tilde{w}_\infty \equiv \frac{E^* w_\infty}{\sigma_0 d} = 2\left(1-\xi\right)^{1/2} - \frac{4}{3}\left(1-\xi\right)^{3/2}; \quad -\frac{1}{2} < \xi < 1, \tag{5-12}$$

where σ_0 is defined in (5-5) and we recall that $\xi=x/d$. No wear occurs outside this range.

4.2.4 Wear model

We assume that wear is governed by the Archard wear law [45] in the form that wear is proportional to the work done against friction. Since the contact pressure is independent of slip displacements, it is approximately constant throughout a single loading cycle, so the wear depth accumulated during the i^{th} loading cycle can be written

$$w_i(x) = 2\mu\alpha\, p_i(x)\Delta(x) \tag{5-13}$$

where α is the wear coefficient and $\Delta(x)$ is the local slip displacement during tangential loading from $-Q$ to Q. We can also write this equation in the dimensionless form

$$\tilde{w}_i\left(\xi\right) = \frac{E^* w_i}{\sigma_0 d} = 2\tilde{\alpha}\,\tilde{p}_i\left(\xi\right)\tilde{\Delta}\left(\xi\right) \tag{5-14}$$

$$\tilde{\alpha} = \mu^2\sigma_0\alpha; \quad \tilde{p}_i = \frac{p_i}{\sigma_0}; \quad \tilde{\Delta} = \frac{E^*\Delta}{\mu\sigma_0 d}. \tag{5-15}$$

With this formulation, wear rates of the order $\alpha\approx 1$ would cause the steady state $w_\infty(\xi)$ to be closely approached in a few cycles. Realistic dimensionless wear rates are significantly lower than unity, and indeed must be of order $\alpha\approx 10^{-2}$ or below for the assumption of constant pressure during each separate cycle to be reasonable.

4.3 Finite-element simulation

In order to determine the effect of wear on the contact stresses, particularly in the presence of yielding, we created a plane strain finite-element model in ABAQUS of the form shown in Figure 4-4. Interest is focused on the slip region at the left edge of the contact, so very considerable mesh refinement was used in this region, as shown in the two successive insets. The two bodies were modelled by semicircles in order to facilitate appropriate mesh gradation away from the contact region. The contact surfaces were chosen to be circular of large radius, in order that the model could be validated using theoretical results.

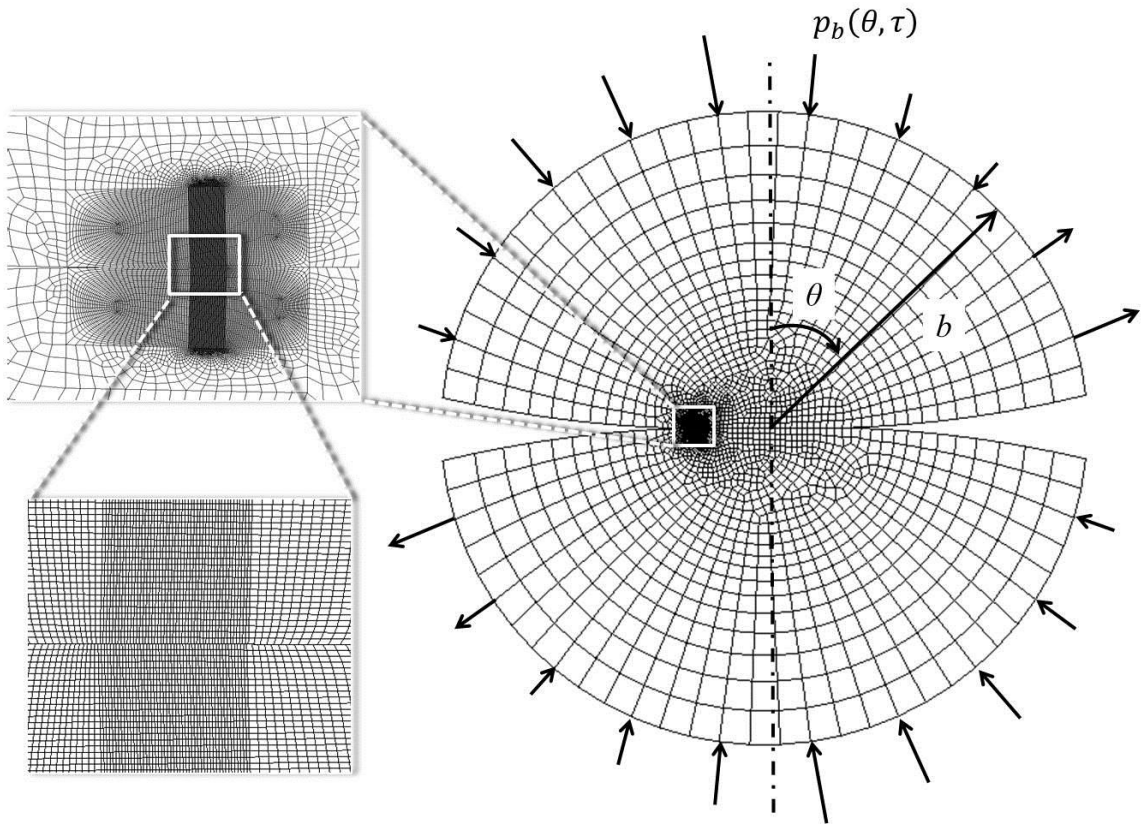

Figure 4-4: Finite-element model.

Sinusoidal tractions $p_b(\theta,\tau)$ were applied at the semicircular boundaries $r=b$ in order to ensure the transmission of the desired forces P, $Q(\tau)$ across the interface. Here τ is a time-like parameter which is introduced solely in order to define the sequence of loading, since this is periodic and hence non-monotonic. All the results were obtained under quasi-static assumptions and hence are independent of loading rate. The model was constrained against rigid body motion by fixing both degrees of freedom at one interior node and one DOF at another node. It was verified that no unwanted nodal forces were generated at these constrained nodes.

The model was validated by comparing the normal tractions with the classical Hertzian solution, and the shear tractions with the Cattaneo-Mindlin solution [54]. Also, slip displacements $\Delta(x)$ during the first cycle were compared with theoretical calculations from Goryacheva *et al.* [17]. In all cases, excellent agreement was obtained.

Wear at the slip nodes was calculated using Eq. (5-13) and the corresponding mesh adjustment was made using the method of fictitious eigenstrains [16]. We assume that the worn material is completely removed from the slip zone. In practical situations, the wear process is generally very slow, so that there is very little change in the contact pressure distribution even after hundreds of cycles. For computational efficiency, it is then reasonable to use an enhanced value of $\tilde{\alpha}$; which is equivalent to considering an appropriate number of successive cycles as having the same pressure distribution.

Various strategies might be used to implement this approximation. Here, we used a linear extrapolation method in which two successive cycles were simulated, including the very small change in the second cycle due to wear, giving values for $\tilde{w}_i(\xi), \tilde{w}_{i+1}(\xi)$. The

change in wear during each of the next *n* cycles is then assumed to be $\tilde{w}_{i+1}(\xi)-\tilde{w}_i(\xi)$, so that the total accumulated wear during *n* cycles is

$$\sum_{j=i}^{i+n}\tilde{w}_j(\xi)=n\tilde{w}_i(\xi)+\frac{n(n-1)}{2}\left[\tilde{w}_{i+1}(\xi)-\tilde{w}_i(\xi)\right] \tag{5-16}$$

4.4 Results

In this section, we first investigate the evolution of the stress field due to wear under elastic conditions, from which we can determine when yielding is triggered for a given dimensionless yield strength σ_Y/σ_0. We then investigate the subsequent plastic deformation, including its effects on the evolution of the wear profile and the accumulated plastic strain.

4.4.1 Elastic behavior

As long as the system remains elastic and the slip zone is small compared with the other linear dimensions in the problem, the dimensionless solution is independent of all material and loading parameters, including the coefficient of friction, and a completely general numerical solution can be presented. The evolutionary process is then characterized by the product $\tilde{\alpha}N$, where *N* is the number of tangential loading cycles. We shall refer to this parameter as the normalized number of loading cycles.

4.4.1.1 Wear profile

Figure 4-5 shows the dimensionless wear profile $w(\xi)$ at several values of $\tilde{\alpha}N$. These results were obtained using a value of *n* in Eq. (5-16) corresponding to $\tilde{\alpha}n\approx 0.16\times10^{-3}$. This involved around 1500 applications of the extrapolation strategy of Eq. (5-16) in the

range $0<\tilde{\alpha}N<0.25$, which we found to be more than adequate to achieve numerical convergence. Also, the high degree of mesh refinement ensured extremely smooth results, which are therefore presented as lines rather than points in this and subsequent figures.

Notice that the wear profile has reached approximately 95% of its steady-state value at $\tilde{\alpha}N=0.25$. We also note that the left extent of the slip zone moves steadily towards the limiting value $\xi=-1/2$ as wear progresses, but the stick-slip boundary remains unchanged, as predicted by theoretical arguments [17, 78].

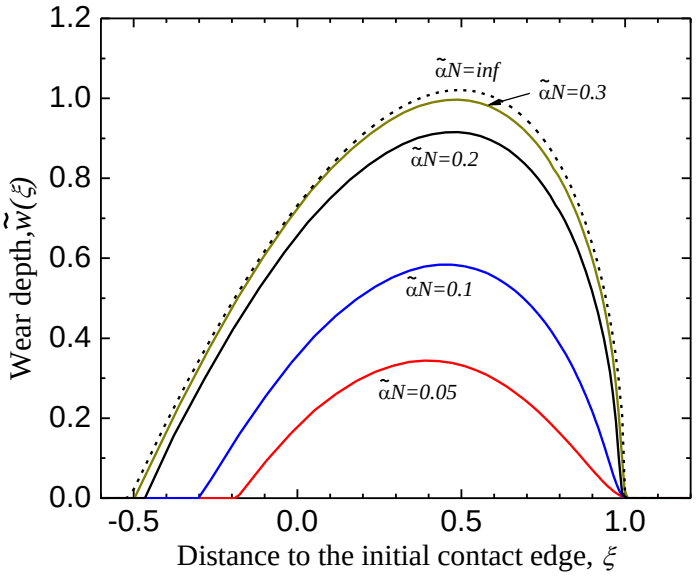

Figure 4-5: Evolution of the wear profile with the normalized number of loading cycles $\tilde{\alpha}N$. The dotted curve represents the maximum wear profile in the elastic case, illustrated by the shaded region in Figure 3 and defined by Eq. (5-12).

4.4.1.2 Contact pressure

Figure 4-6 shows the corresponding evolution of the dimensionless contact pressure distribution $\tilde{p}(\xi)$. The K_I-dominated field is well-developed away from the boundary of

the stick zone for $\tilde{\alpha}N$ >0.1, but the maximum pressure near the stick-slip boundary ξ =1 continues to grow (without limit) as the wear profile approaches its long-time limit.

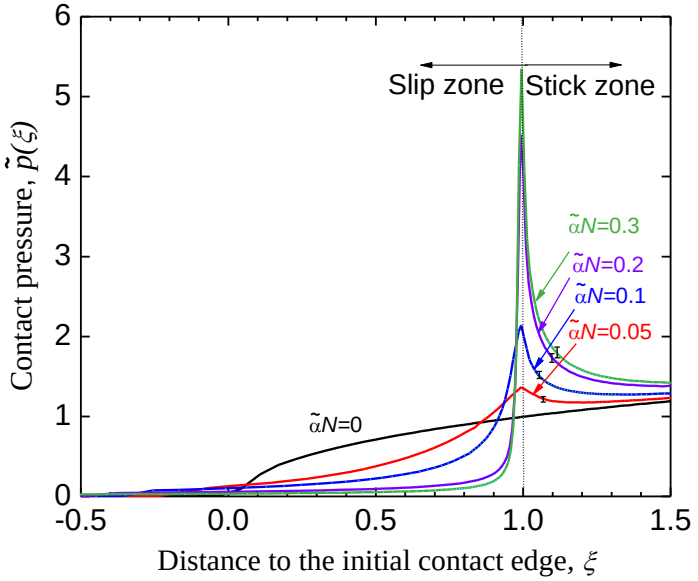

Figure 4-6: Evolution of the dimensionless contact pressure $\tilde{p}(\xi)$ with the normalized number of loading cycles $\tilde{\alpha}N$, from elastic analysis.

4.4.1.3 Maximum von Mises stress

For real materials, the development of the mode-I singularity at the stick slip boundary will be limited by plastic deformation, which we assume occurs at a critical value σ_Y of the von Mises equivalent tensile stress

$$\sigma_e = \sqrt{\frac{3\sigma_{ij}\sigma_{ij} - \sigma_{ii}\sigma_{jj}}{2}}\,. \tag{5-17}$$

Figure 4-7 shows the magnitude of the maximum von Mises stress $\sigma_e^{\max}$ as a function of $\tilde{\alpha}N$. At the beginning of the process, the maximum occurs far from the slip region, but as the peak in contact pressure starts to develop at around $\tilde{\alpha}N \approx 0.1$ we obtain an almost

linear increase in $\sigma_e^{\max}$ with $\tilde{\alpha}N$. The instant at which plastic deformation starts depends of course on the ratio σ_Y/σ_0. In all cases, the maximum von Mises stress was observed to occur on the contact interface, at the stick-slip boundary.

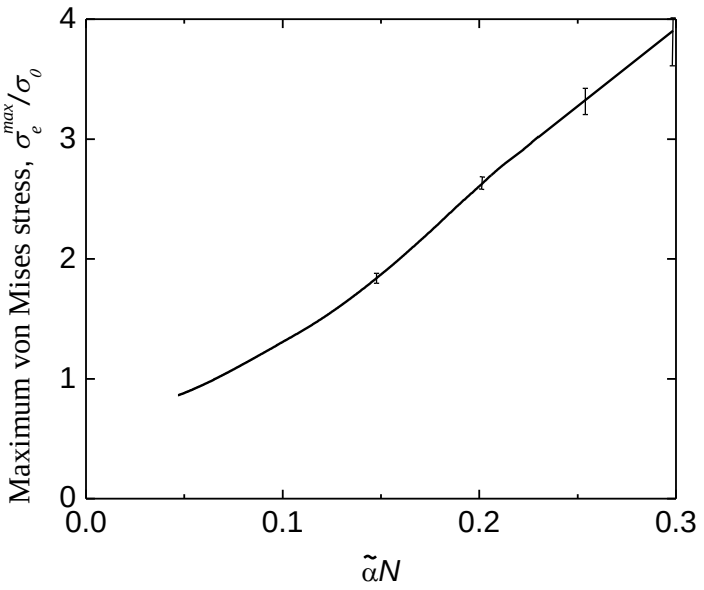

Figure 4-7: The maximum von Mises stress associated with the developing contact pressure singularity. Notice that early in the wear process, the maximum occurs far from the slip region and is not related to the wear process.

4.4.2 Plastic deformation

We next consider the effect of plastic deformation on the evolutionary process. We assume that the material is elastic-perfectly plastic, so that yielding occurs at a constant von Mises stress σ_Y. This introduces a new dimensionless parameter σ_Y/σ_0 into the calculation, so we are only able to present particular cases. In order to explore the influence of plastic deformation, we chose the values σ_Y/σ_0=1 and 1.5, which we note from Figure 4-7 ensure that the contact starts in the elastic régime, but that plastic deformation starts relatively early in the wear process (at $\tilde{\alpha}N$ =0.07 for σ_Y/σ_0=1).

4.4.2.1 Wear profile

Figure 4-8 (a, b) shows the development of the wear profile for σ_Y/σ_0=1 and 1.5 respectively. The limiting value of wear in the elastic case is shown dotted for comparison. It is clear that plastic deformation allows wear to continue indefinitely both in depth and extent. In particular, the slip-stick boundary extends into the original stick zone and the wear scar also extends further into the original separation zone. A comparison of the two figures shows that wear progresses more rapidly when the yield stress is lower.

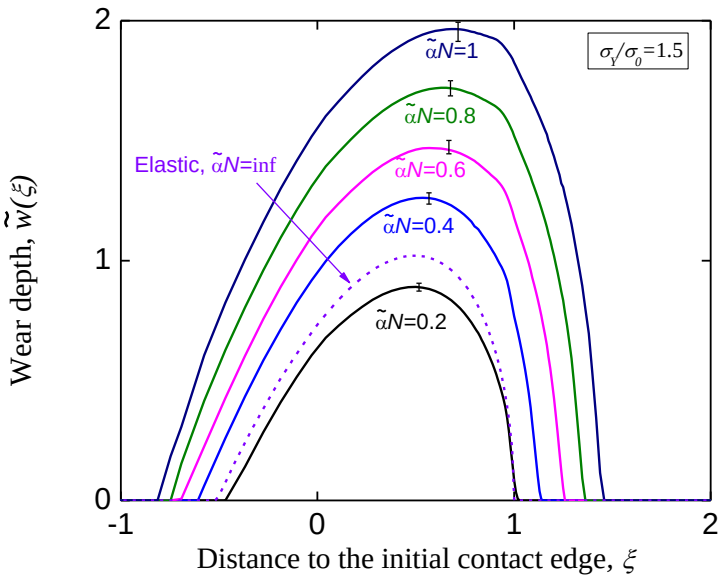

(a)

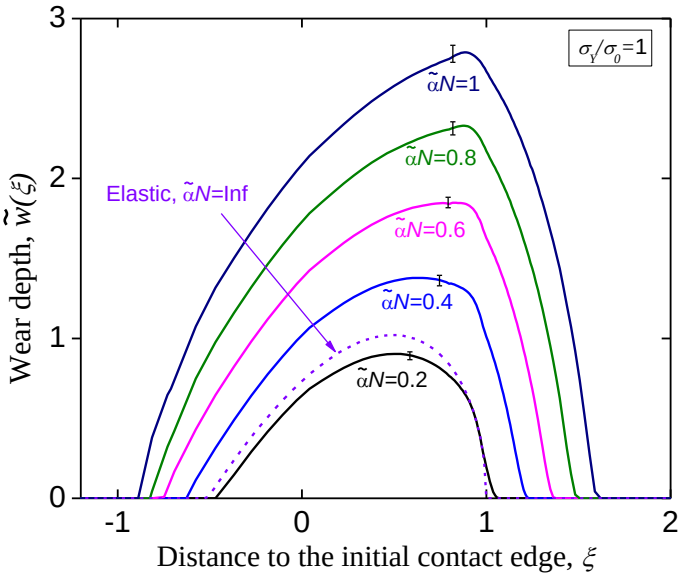

(b)

Figure 4-8: Development of the dimensionless wear profile $\tilde{w}(\xi)$ with the normalized number of loading cycles $\tilde{\alpha}N$ for the elastic-plastic case: (a) σ_Y/σ_0=1.5 and (b) σ_Y/σ_0=1. The limiting wear in the elastic solution is shown dotted.

4.4.2.2 Contact pressure

The corresponding contact pressure distributions are shown in Figure 4-9 (a, b). The most striking feature of these results is that the maximum contact pressure now levels out at about $p_{max}\approx 2.5\sigma_Y$. This ratio is consistent with values for the maximum normal stress that arise in elastic-plastic crack problems [86, 87], being slightly less than the limiting value of 2.97 expected from the Prandtl solution for a crack in a rigid-plastic material. The location of this maximum moves to the right as wear progresses, and is always very close to the instantaneous slip-stick boundary.

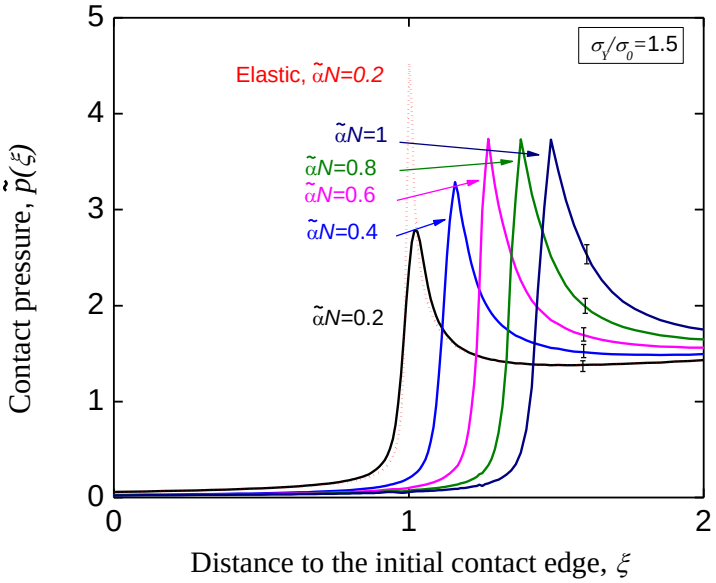

(a)

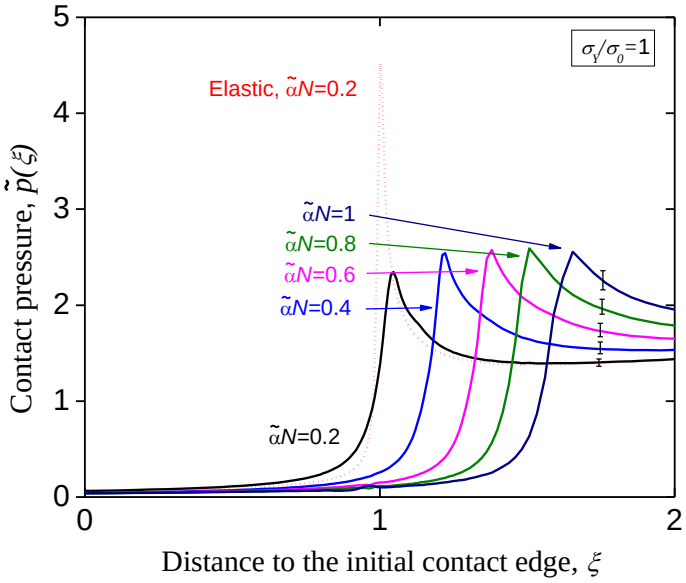

(b)

Figure 4-9: Evolution of the contact pressure distribution $\tilde{p}(\xi)$ with the normalized number of loading cycles $\tilde{\alpha}N$ for the elastic-plastic case: (a) σ_Y/σ_0=1.5, (b) σ_Y/σ_0=1. The dotted curve shows the elastic pressure distribution for $\tilde{\alpha}N$ =0.2.

4.4.2.3 Accumulated plastic strain

As the wear evolves, a plastic zone forms starting from the contact interface and its size grows. The magnitude of the accumulated plastic strain is defined as

$$\varepsilon_e^p = \int_0^t \sqrt{\frac{2}{3}\frac{\partial \varepsilon_{ij}^p}{\partial \tau}\frac{\partial \varepsilon_{ij}^p}{\partial \tau}}\, d\tau \ : \tag{5-18}$$

where we recall that τ is a time-like parameter characterizing the sequence of loading. The maximum accumulated plastic strain, ε_e^p, is considered to be an important indicator of fatigue crack initiation [88-91].

Notice that with the definition (5-18), the plastic strain increases monotonically during the cyclic loading process, even if the individual strain components oscillate. Two extreme cases would be (i) if the plastic strain components reverse completely during each cycle, as in a beam subjected to completely reversed bending moments, or (ii) if the plastic strain components accumulate monotonically.

Case (i) raises difficulties for the present computational scheme, since it is not practical to simulate every cycle of loading throughout a realistic wear process. We therefore performed a preliminary study in which we simulated n=50 consecutive cycles in the plastic régime and compared the resulting accumulated plastic strain with that accumulated during a single cycle with an enhanced wear rate $\tilde{\alpha} n$. The results differed by less than 3% and, in fact, the single-cycle strain was the largest. We conclude that the evolving plastic strain is a result of monotonic accommodation to the change of profile due to wear, rather than of cyclic plasticity. This also implies that estimates based on a reduced

number of cycles with an enhanced wear rate are likely to give good predictions for the accumulation of plastic strain.

Figure 4-10 shows contour plots of ε_e^p at $\tilde{\alpha}N$ =0.15, 0.2, and 0.25 for σ_Y/σ_0=1. In the interests of generality, we present these results in the combination

$$\tilde{\varepsilon}_e^p \equiv \frac{E^* \varepsilon_e^p}{\sigma_0}, \tag{5-19}$$

since the results then apply to all systems with the same ratio σ_Y/σ_0.

The plastic zone first grows along the contact interface and then spreads in the perpendicular direction. However, the maximum accumulated plastic strain is always located close to the contact interface and it moves with the slip-stick boundary.

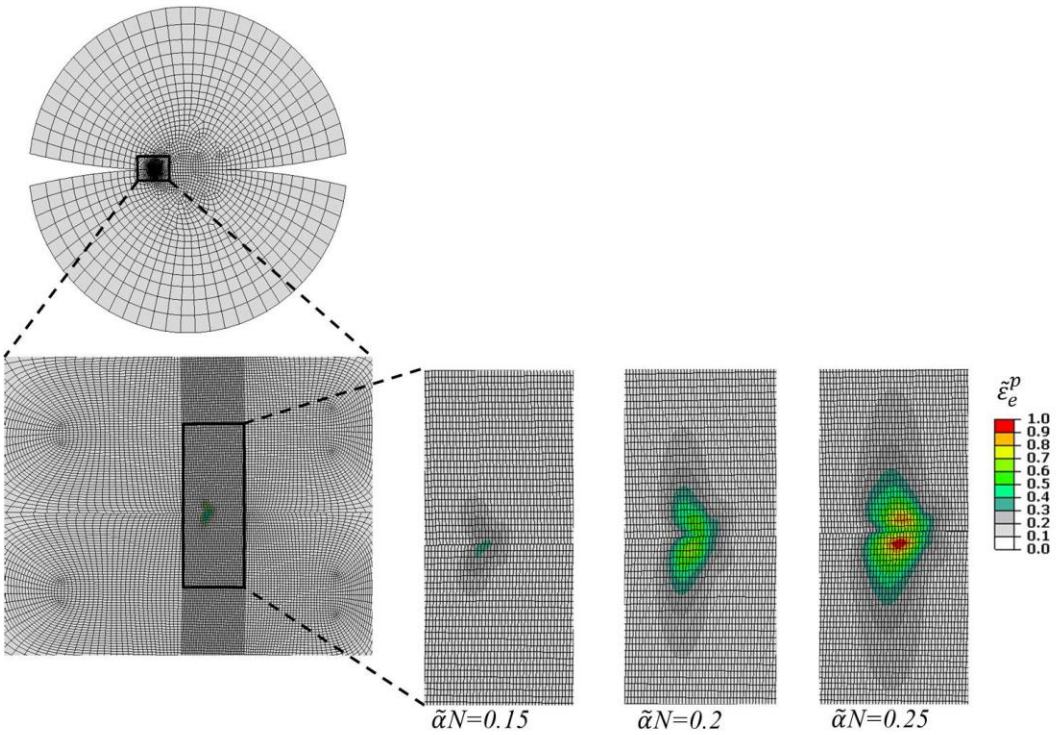

Figure 4-10: Contour plot of accumulated plastic strain at three values of $\tilde{\alpha}N$ (σ_Y/σ_0=1).

Figure 4-11 shows $\tilde{\varepsilon}_e^{p,\max}$ as a function of $\tilde{\alpha}N$ for σ_Y/σ_0=1 and 1.5. In each case, plastic deformation starts at the value of $\tilde{\alpha}N$ determined by the appropriate intercept in Figure 7, and $\tilde{\varepsilon}_e^{p,\max}$ increases approximately linearly thereafter. It is interesting to note that for higher yield stress, plasticity is delayed, but the plastic strain then accumulates more rapidly. Figure 4-11 is terminated at $\tilde{\alpha}N$ =0.3 because beyond that point, the plastic zone extends into a region of coarser mesh, implying less accuracy. However, the indications from these less precise calculations are that $\tilde{\varepsilon}_e^{p,\max}$ continues to increase linearly indefinitely as the wear scar continues to extend.

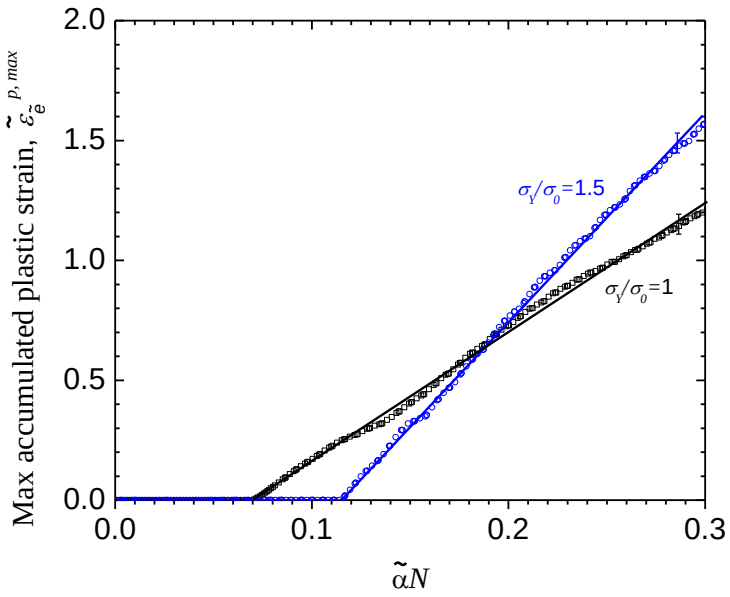

Figure 4-11: Maximum accumulated plastic strain $\tilde{\varepsilon}_e^{p,\max}$ as a function of $\tilde{\alpha}N$ for σ_Y/σ_0=1 and 1.5.

4.4 Conclusions

We have presented a finite element model of the evolution of local stress fields due to fretting wear, in the case where the normal contact force is constant and the slip zone is

small compared with the other linear dimensions of the system. In this limit, the elastic solution characterizes all possible problems of this class, of course, including any designs of springs and dimples in the fuel assembly. As wear progresses, the slip-stick boundary remains stationary and a local stress singularity is developed, which can be characterized by a stress-intensity factor $K_I = K_{II}/\mu$, where K_{II} is the mode-II stress-intensity factor for the `full stick' solution and μ is the coefficient of friction.

For elastic-plastic material behavior, the slip-stick boundary moves steadily into the stick region once the yield stress is locally exceeded. The contact pressure distribution then achieves a stable peak value which moves with this boundary. Plastic strain accumulates with a maximum at or near this moving boundary, and the maximum accumulated plastic strain increases approximately linearly with subsequent cycles.

Chapter 5

A algorithm to couple wear and creep

5.1 Introduction

Due to a excitation force and high temperatures, both creep and wear may occur at the grid-to-rod contact interface [14, 22]. Creep deformation and dimensional changes caused by wear result in stress relaxation and a change in the contact area; this affects the propagation of GTRF wear and the lifetime the fuel assembly. The creep and wear also affects the life or performance of components in many other applications [92-95]. The simulation of wear has been addressed in many studies, but an efficient and reliable numerical algorithm to model the two behaviors is still missing.

The period of the vibrations responsible for the GTRF wear is usually much smaller than the time scale for significant amount of wear [2, 13]. In wear simulation, the wear depth is usually predicted using the Archard's law [45, 54], in which the local wear depth is proportional to the product of the local contact pressure and slip distance. However, the wear usually evolves slowly, and the wear in one loading cycle is usually small. Therefore, it would be computationally expensive to update the surface geometry every time increment. Instead, the wear process is further discretized and the mesh adjustment was usually executed after multiple cycles. However, the need to simulate every vibration cycle makes this method inefficient. Because the loading condition changes very little in

successive cycles, it is reasonable to assume that the wear growth is the same in those cycles. In this way, the wear in one vibration cycle can be scaled to represent N cycles. This algorithm is usually referred to as the Euler method [40, 41, 43, 44]. The efficiency and reliability of the model is sensitive to the choice of N. If N is too large, it may cause excessive error in the analysis; if N is too small, it will be a trivial benefit to the efficiency. Therefore, a given value of N may be reasonable at the beginning of the simulation, but become inappropriate as the wear propagates. So, as an improved method, the scale factor N can be dynamically determined so that the growth of the maximum wear increment is scaled up to a threshold value [41]. This method is reliable and efficient in simulations if the worn interface is relatively smooth. However, in many engineering problems, the worn interface may not be smooth and small local wear increment may cause very large variation of contact pressure. For example, in partial-slip problems, very small increment of wear depth around the stick-slip boundary may result in very large change of local contact pressure [16, 17]. Therefore, in those applications if we couple the time scale of wear and vibrations using a threshold wear increment, some dramatic change of contact pressure may not be picked up, which would cause an error in the wear prediction.

Consideration of creep in this problem brings another time scale. Similar to wear, the time scale of significant creep deformation is usually much larger than vibrations. In numerical modeling of creep, a relatively large time increment can be used, which is usually much larger than the period of any vibrations. Therefore, if the model is based on the time scale of vibrations the computational cost will be unpractically high. In creep simulation, constitutive laws associated with various creep mechanisms are used to describe the relationship between the strain rate and stress [6, 96]. Of course the determination of

the time increments do not account for the amount of wear. The creep and wear in the FEA modeling have their own convergence criteria and do not interact with each other. Therefore, a time scale based on either one of them may be too large and cause excess error. Overall, an efficient method to couple the time scales of vibrations, creep and wear is still missing.

Stress redistribution is the criterion governing the time scale of both creep and wear. The creep and wear may affect each other through stress redistribution. On one hand, the stress redistribution due to creep deformation may affect both local contact stress and slip, which affects the wear rate. In many engineering applications, preloaded components are designed to provide full stick condition on the contact interface. However, partial-slip may occur if there are vibrations [16, 28]. Over time, the initially small partial-slip zone propagates and the wear scar becomes larger [28]. The stress relaxation owing to creep will significantly accelerate this propagation. On the other hand, the dimension loss due to wear causes redistribution of contact stress; this may in turn affect the creep strain rate, especially that near the contact interface. As the dominant mechanism may change with time, an assumption of dominant mechanism may not persist throughout the simulation. Because the effects of the two mechanisms are through the stress, as long as the stress variation over a time increment is limited within a reasonable threshold, both creep and wear will converge reliably.

In this chapter, we are going to set up a numerical algorithm that can be used to couple creep and wear efficiently and reliably. Instead of simulating every vibration cycle, we simulate the wear and creep of a successive cycles using an effective cycle and a magni-

fied wear coefficient. The efficiency of modeling is optimized by enforcing the stress redistribution over an effective vibration cycle to be less but close to a threshold. Using this method, the model can automatically couple wear and creep together when both behaviors contribute to the stress redistribution. This method can avoid the complexity of identifying the dominant mechanism for stress redistribution and enhance the efficiency significantly.

5.2 Methodology

The stress redistribution due to creep and wear usually evolves slowly, while the vibrations responsible for wear are usually much faster. In this section, we describe a method to effectively couple the time scale of vibration with that of wear and creep, and present an algorithm to optimize the simulation reliability and efficiency.

5.2.1 Coupling vibration and creep-wear using effective cycles

As mentioned in Section 1, in many problems such as GTRF wear [2, 4], the relative displacement on a contact interface responsible for wear is usually caused by vibration, of which the period is usually in seconds. However, the time scale of significant stress redistribution due to creep and wear may be in months or years. In a numerical simulation, the time increments need to be smaller than the period so that the resolution will be high enough to represent the vibration profile. Therefore, a numerical simulation discretized based on the time scale of vibrations will be unpractically computer intensive and an efficient coupling method is critically necessary.

If we use the Archard law to model wear, the local wear increment is proportional to the local frictional work. If we assume the vibration that is responsible for wear is cyclic and has a period of T_0, the wear increment one cycle is written

$$w_i(x) = \int_{t_i}^{t_i+T_0} \alpha_0 p_i(x,\Delta)\mu d\Delta \tag{6-1}$$

where t_i is the start time of a vibration cycle, μ is the friction coefficient in the Coulomb friction law, α_0 is the wear coefficient, $p(x, \Delta)$ is the local contact pressure and Δ is the local slip distance. Notice that the wear increment is an integration of slip distance, therefore is independent of the length of a cycle T_0.

Although there are various constitutive laws associated with different creep mechanisms [6, 96], as a simplification, the equivalent creep strain in this chapter is given by

$$\varepsilon = \int_{t_i}^{t_i+T_0} \dot{\varepsilon} dt = \int_{t_i}^{t_i+T_0} A\tilde{\sigma}^n dt \tag{6-2}$$

where $\tilde{\sigma}$ is the Von mises equivalent stress, the equivalent creep strain rate is $\dot{\varepsilon} = \sqrt{2/3\dot{\varepsilon}_{ij}\dot{\varepsilon}_{ij}}$ and A and n are constants depending on temperature and microstructure. If we consider creep only, the growth of creep strain in a cycle is an integration of time, and is usually independent of the slip distance. In other words, as long as the time is the same, the creep strain over a time interval is independent on the number of loading cycles. Next, we will take advantage of this feature to couple the time scale of vibration with that of wear and creep.

We assume the displacement boundary condition (i.e. vibration) that is responsible for wear is shown as the left curve in Figure 5-1. As the growth of wear depth and creep deformation is small in one vibration cycle T_0, it is reasonable to assume that the stress condition in a number of successive cycles is the same. If this assumption is valid in a time interval of T_i, then we can define a simplified effective cycle with length of T_i as is shown on the right of Figure 5-1. In an effective cycle, instead of simulating many cycles, we simulate only one cycle but use a magnified wear coefficient so that the wear can proportionally represent that in many cycles. Then the wear increment in the effective cycle is calculated by

$$w_i(x) = \frac{T_i}{T_0}\int_{t_i}^{t_i+T_i} \alpha_0 p_i(x,\Delta)\mu d\Delta. \tag{6-3}$$

Note this equation is similar to Eq. (6-1), we only need to scale up the wear coefficient by T_i/T times.

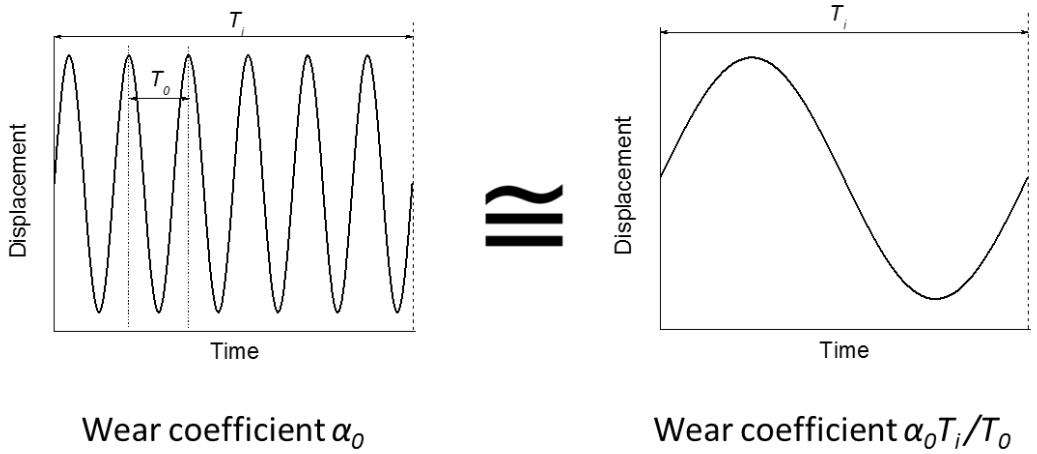

Figure 5-1: Cyclic displacement boundary condition (i.e. the vibration) is coupled with wear-creep using effective cycles. The force loading can be treated in a similar way.

As the creep is the integration of time and we keep time unchanged when using effective cycles, the creep strain in the effective cycle is calculated by

$$\varepsilon = \int_{t_i}^{t_i+T_i} A\tilde{\sigma}^n dt \tag{6-4}$$

Note this equation has the same form as Eq. (6-2).

5.2.2 Optimization the length of effective cycles

When coupling wear and creep in a numerical simulation, the length of an effective cycle T_i needs to be small enough so that the assumption in Figure 5-1 is valid. In a simulation, the magnitude of T_i proportionally determines the magnitude of time increments in the cycle. If T_i is too large, the creep deformation in time increments will cause excess error on the contact pressure $p_i(x,\Delta)$ and Δ in Eq.(6-1), or the wear will result in excess error on σ in Eq. (6-2) the other way around. Their interaction is generally through their effects on the stress condition. Therefore, we need to limit the variation of stresses within a reasonable limit. As the shear stress is proportional to contact pressure on a slipping contact interface controlled by the Coulomb law, we only need to limit the contact pressure. Therefore, if we can limit the variation of contact pressure over an effective cycle T_i within a well-defined limit, Δp_t, the two behaviors can be coupled effectively. The value of the reasonable limit Δp_t will depend on the stress level on a interface. As the stress level may change over time, we define $\Delta p_t = \varphi p_{m,i}$, where $p_{m,i}$ is the maximum contact pressure along the interface at the beginning of the i^{th} cycle and the constant φ is a threshold that determines the amount of stress redistribution over an effective cycle. We need to determine an appropriate φ to balance the efficiency and accuracy. As a verification method, we can run the simulation using a relatively large φ, say 10%, for certain number

of effective cycles, say 5 cycles, and then repeat the simulation using a decreased φ, say 5%, if the difference of contact pressure is less than the numerical uncertainty of the model, we can use this φ for the simulation. The flow of applying this method in a numerical simulation is shown in Figure 5-2. We start the modeling with a relatively small effective cycle T_1 so that the maximum change of contact pressure, $\Delta p_{m,i}$, due to wear and creep are much smaller than the threshold value Δp_t. Then we increase the length of the next effective cycle proportionally, so that the stress relaxation is close to the threshold. In a similar manner, we can always update the length of the next effective cycle based on the result of current one the following equation,

$$T_i = \frac{\varphi p_{m,i}}{\Delta p_{m,i}} T_{i-1} \tag{6-5}$$

where T_i and T_{i-1} denotes the length of the current (i^{th}) and last effective cycles. It should be noted that the maximum contact pressure $p_{m,i}$ and the maximum change of contact pressure $\Delta p_{m,i}$ may be at different nodes.

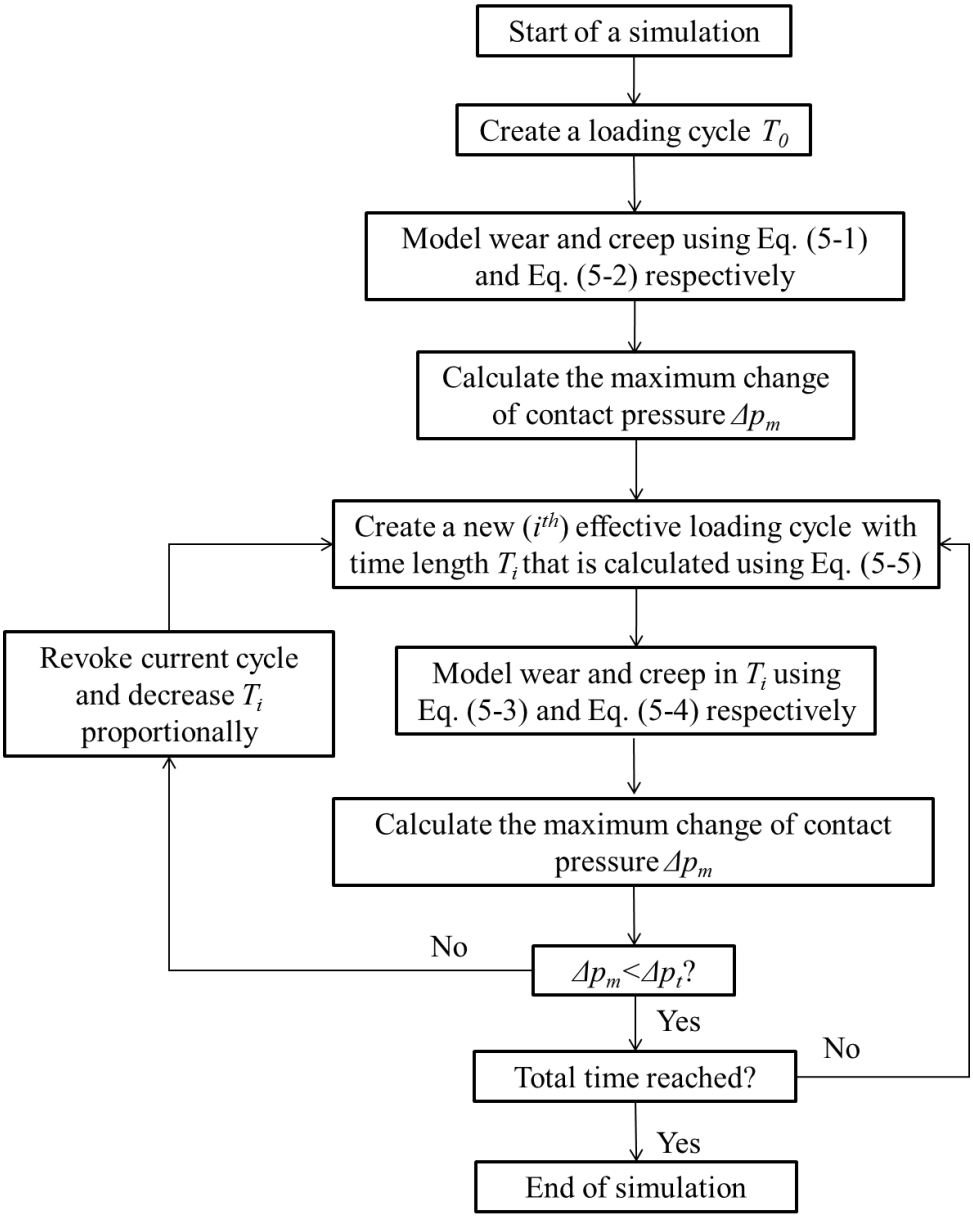

Figure 5-2: The algorithm to couple wear and creep

Using this method, we can keep predicting and updating the length of the next effective cycle based on the stress variation of current one. At the end of each effective cycle, we check the real change of contact pressure to make sure it is within the threshold, if not, we revoke the cycle and rerun it using a proportionally decreased length. In this way,

the change of contact pressure will be always close to but not greater than the predefined threshold value.

5.3 FEM examples

In this section, we set up 2D FEA models in ABAQUS to illustrate the application of this method in a couple of typical scenarios. We use a Hertz contact under ‘full-slip’ condition to show the application of this method when the creep and wear cause a global stress relaxation. We also use a Hertz contact under ‘partial-slip’ condition and a complete contact under ‘full-slip’ condition to illustrate this method when creep and wear causes localized stress redistribution.

5.3.1 Full-slip with Hertz contact

We first consider a situation when the creep and wear cause a global stress relaxation on the interface. We set up a simple plain-strain Hertz-contact model as shown in Figure 5-3. The contact is formulated using a master-slave contact pair, in which the nodes on the slave surface move in order to avoid penetration. The frictional force is modeled using a classical Coulomb friction law.

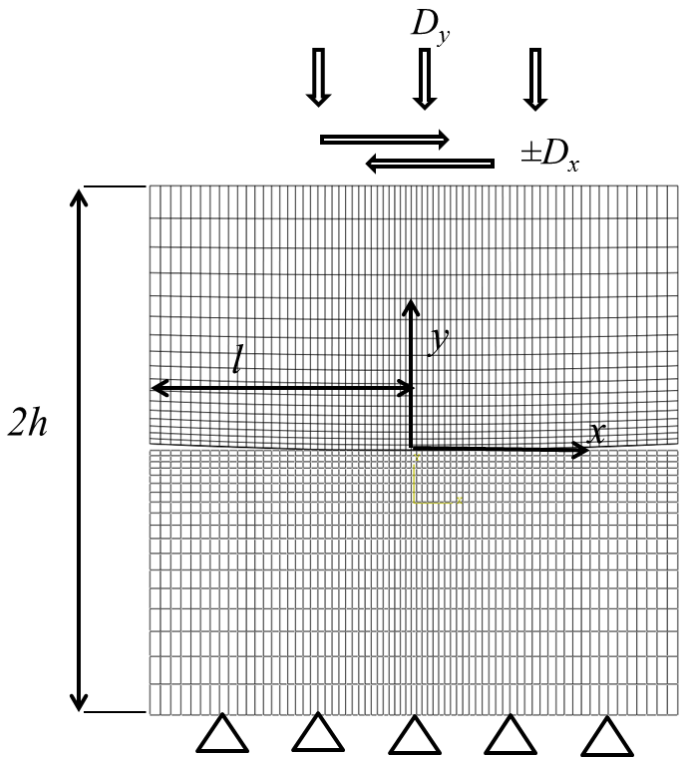

Figure 5-3: A Hertz contact example. The contact pair is subjected to a fixed normal displacement D_y and oscillating tangential displacement $\pm D_x$. The indenter has a lower surface with a radius of 20h.

As is shown in Figure 5-3, at the beginning of the simulation, a fixed displacement D_y was first applied at the top of the indenter as a preload. Then, in each cycle, a tangential displacement oscillating between $\pm D_x$ creates interfacial slip. The fixed normal displacement boundary conditions are applied so that stress relaxation on the interface is more significant. We make the amplitude of the tangential displacement large enough so that the contact interface is under a 'full-slip' condition. We use the algorithm described in Figure 5-2 to couple creep and wear. The simulation is quasi-static and thus an effective cycle is divided into small time increments. In each time increment, both creep and wear are calculated using the Eq. (6-3) and Eq. (6-4). The geometry change due to wear is modeled by assigning eigen strains to the surface elements [16]. The stress redistribution

over an effective cycle is evaluated by comparing the contact pressure in the beginning of the cycle with that of the next cycle. The period of the next effective cycle is determined using the Eq. (6-5).

We first consider a scenario that wear and creep make comparable contributions to the stress relaxation. We choose parameters as the scenario 1 in Table 5-1 so that this condition can be satisfied. Using these parameters, we simulated the wear and creep for $t/T_0=5\times10^4$= the real number of cycles. We repeated the simulation using different values of threshold φ: 20%, 10% and 5%. Figure 5-4 (a, b) show the contact pressure and wear depth respectively. In order to distinguish the contribution of wear and creep to stress relaxation, we also show a curve of contact pressure with wear switched off in Figure 5-4 (a); it is confirmed that the contribution of wear and creep to stress relaxation is comparable. The curves of three threshold values overlap, therefore, the simulation has good accuracy when the threshold φ is as large as 20%.

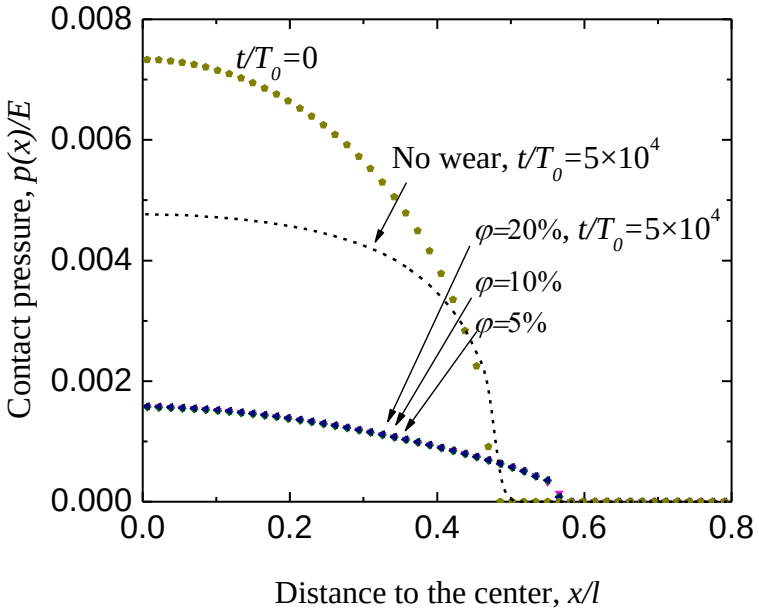

(a)

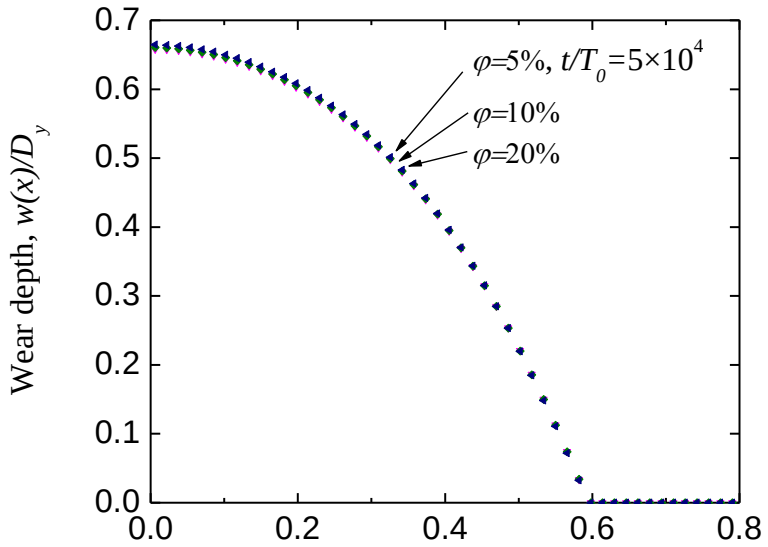

(b)

Figure 5-4: Contact pressure (a) and wear depth (b) after $t/T_0=5\times10^4$ for a full-slip Hertz contact when the wear and creep have comparable contribution to the stress relaxation (Scenario 1). The curves converge to the same one as the threshold φ decreases from 20% to 5%.

Table 5-1: Dimensionless parameters

	Scenario 1 (Hertz full-slip)	Scenario 2 (Hertz full-slip)	Scenario 3 (Hertz partial-slip)	Scenario 4 (Complete full-slip)
D_x/l	8×10^{-3}	8×10^{-3}	4×10^{-3}	8×10^{-3}
D_y/l	0.01	0.01	0.01	0.01
l/h	1	1	1	1
μ	0.2	0.2	0.2	0.2
v	0.25	0.25	0.25	0.25
n	4	4	4	4
AE^nT_0	4×10^{15}	4×10^{15}	4×10^{15}	4×10^{15}
α_0E	3.5×10^{-5}	3.5×10^{-7}	7×10^{-5}	3.5×10^{-5}

Next we consider a scenario in which creep dominates the stress redistribution but the wear depth is of particular interest. This corresponds to applications such that small wear of coating layers may result in critical risks. As is shown in the scenario 2 of Table 2, we reduce wear coefficient by 100 times while keeping other parameters the same as that in scenario 1. Figure 5-5 (a) shows the initial and final contact pressure. The curves overlap, since the stress relaxation is dominated by creep, which is barely affected by the number of effective cycles. Again the 'no wear' curve is shown for reference, based on which we confirm that the wear has negligible effect the evolution of contact pressure. Figure 5-5 (b) shows the wear depth. The curves converges to the same one as we decrease φ from 20% to 2%. The difference between 5% and 2% is already smaller than the numerical uncertainty and therefore 5% is good balance of efficiency and accuracy. In fact, the error is relatively small when the φ is as large as 20%. In the given time interval, the number of real vibration cycles is $t/T_0=5\times10^4$. However, by the adaptive method, we can effectively model the process with negligible error using less than 30 effective cycles, which is a huge improvement of computation efficiency.

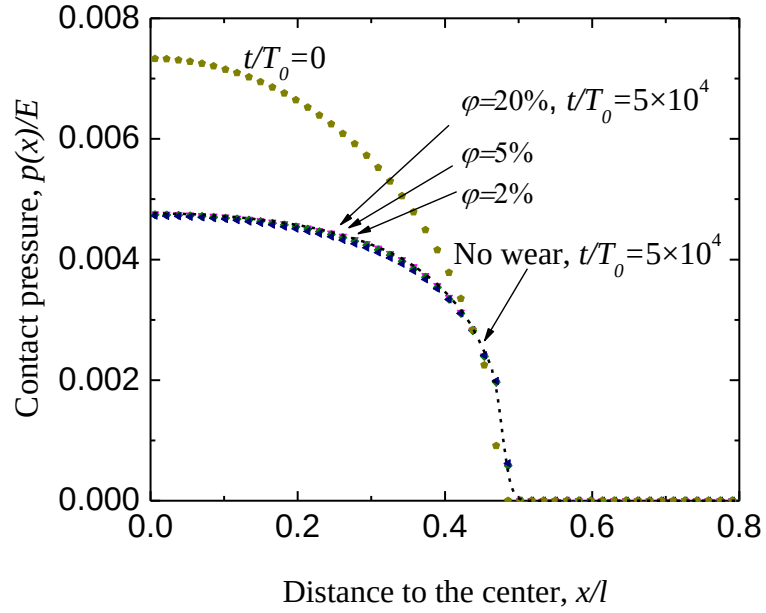

(a)

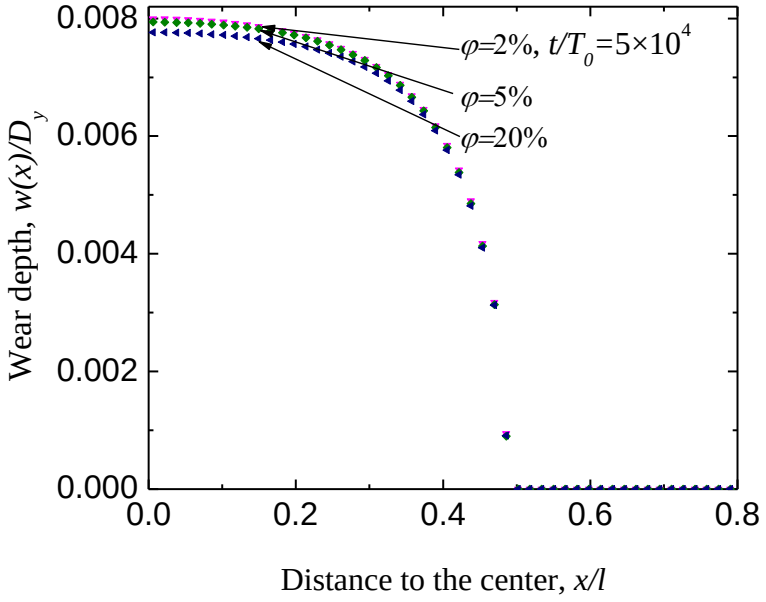

(b)

Figure 5-5: Contact pressure (a) and wear depth (b) after $t/T_0=5\times10^4$ for a full-slip Hertz contact when the creep dominates the stress relaxation (Scenario 2), the curves converge to the same one as the threshold φ decreases from 10% to 2%.

5.3.2 Partial-slip with Hertz contact

As is mentioned in section 1, many preloaded contact pairs are designed to provide full-stick condition. However, partial-slip may occur around the contact edge due to vibrations [28]. Over time, as the stress level is decreased owing to creep deformation, the partial-slip may evolve to full-slip. In this process, the dominant mechanism for stress relaxation may change from creep to wear over time, which increases the complexity of the problem. In order to validate the method in this application, we again use the same setting as Figure 5-3, but increase the friction coefficient so that only part of the contact interface will have slip. Again, we repeat the simulations using different threshold φ ranging from 20% to 2%. Figure 5-6 (a) shows the evolution of contact pressure using φ of 20%, 5% and 2%. The data at t/T_0=1×10^4, 5×10^4 and 1×10^5 are plotted to show the progress of wear and creep. Again a curve for the 'no wear' case is plotted to distinguish the contribution of wear and creep. At t/T_0=1×10^4, the difference between 'no wear' and the three 'wear' cases with wear are very small. Therefore, most stress relaxation is caused by creep. However, at t/T_0=1×10^5, the contact for the three 'wear' cases decrease to a much lower level than the 'no wear' case. Therefore, wear has dominated the stress relaxation. In Figure 5-6 (a) the curves of contact pressure using different threshold φ converge well. Figure 5-6 (b) shows the wear depth at t/T_0=1×10^4, 5×10^4 and 1×10^5. At t/T_0=1×10^4, the wear, i.e. slip, only occurs at the contact edge, while at t/T_0=5×10^4 it has evolved to full-slip. As we decrease the φ, the curves asymptotically approach a limit. The difference between φ = 5% and 2% is negligible. In this example, the dominant mechanism for stress relaxation change from creep to wear over time, so we cannot assume a dominant mechanism. The effective cycle method can automatically determine a reasonable time scale

without identifying the dominant mechanism. This example also demonstrates its capability of dealing with partial-slip problems.

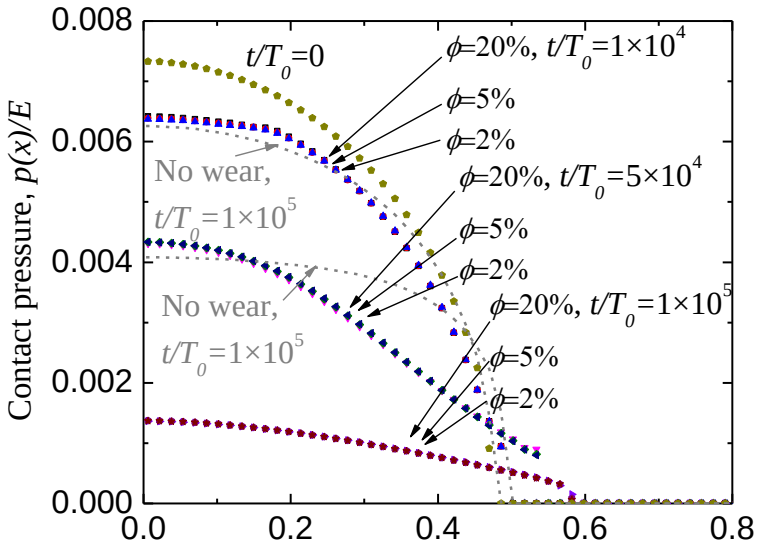

(a)

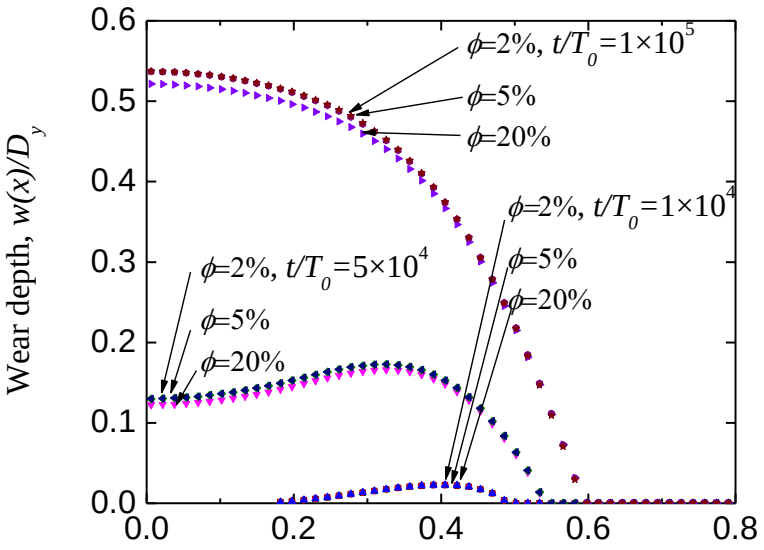

(b)

Figure 5-6: The evolution of contact pressure (a) and wear depth (b) for a Hertz contact evolving from partial-slip to full-slip (Scenario 3). The stress relaxation is initially dominated by creep (t/T_0=0 to 1×10^4) and later dominated by wear (t/T_0=5×10^4 to 1×10^5). The curves of both contact pressure and wear depth converge to the same ones as the threshold φ decrease from 20% to 2%.

5.3.3 Contact with a sharp corner

In this section, we consider a contact pair with a sharp corner, i.e. a complete contact. The stress field is elastically singular around the corner, leading to dramatic variation of creep rate and wear rate along the interface. We use this example to show the application of this method in a scenario when creep and wear cause localized stress redistribution. In order to capture the behaviors around the corner, the mesh is refined to be 0.001 times of l. The contact is formatted using a way similar to the Hertz contact in the last section. The displacement loading condition is shown in Figure 5-7. Again, a constant normal and oscillating tangential displacement D_y and $\pm D_x$ are applied so that the contact interface will be in 'full-slip' condition. We repeated the simulation using threshold φ=20%, 10% and 5%.

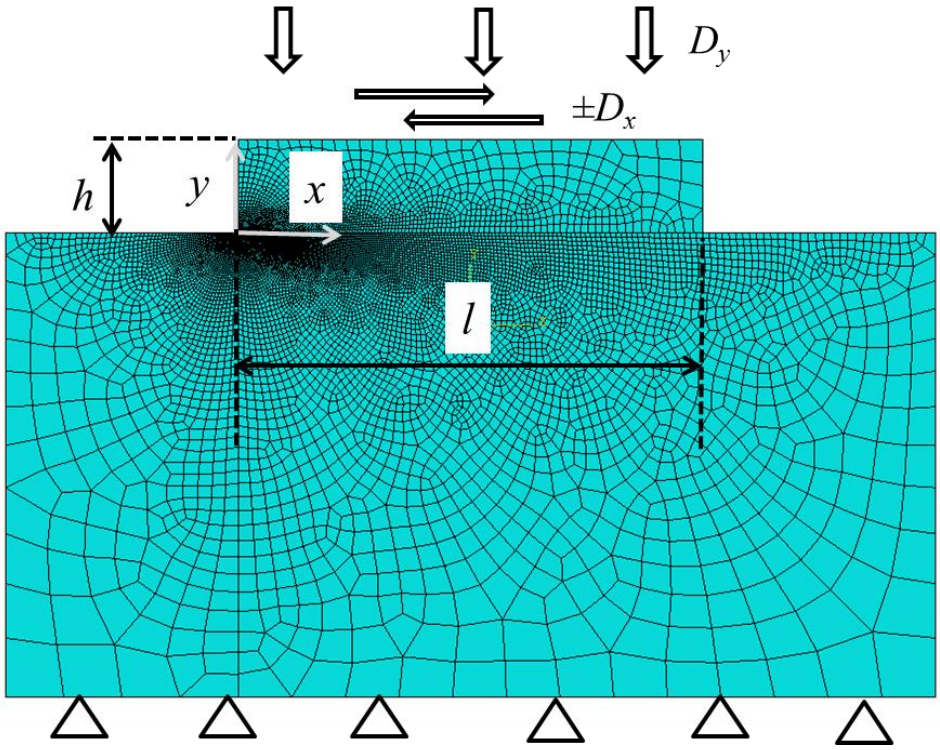

Figure 5-7: A contact model with sharp corners. The contact pair is subjected to a fixed normal displacement D_y and oscillating tangential displacement $\pm D_x$.

Figure 5-8 (a, b) shows the contact pressure and wear depth respectively. Due to creep and wear, the stress at the corner drops dramatically. Although the sharp corner increases the uncertainty, the error for both contact pressure and wear depth are still within a reasonable range even if φ is as large as 20%. Although the stress level increases dramatically when it approaches the contact corner, the modeling can still pick up the dominant variations automatically, and the results converge well. Owing to the intensified mesh around the corner, the computational cost is increased significantly, making the efficiency a key for a practical simulations. The algorithm in this chapter significantly improved the efficiency and enables reliable modeling.

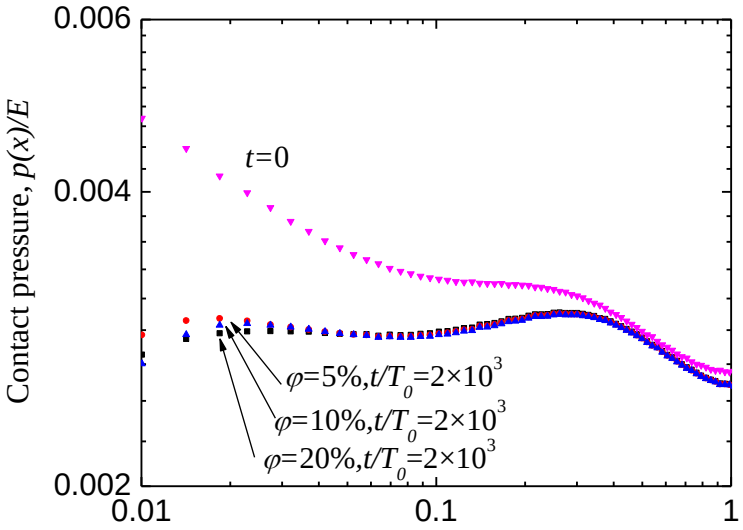

(a)

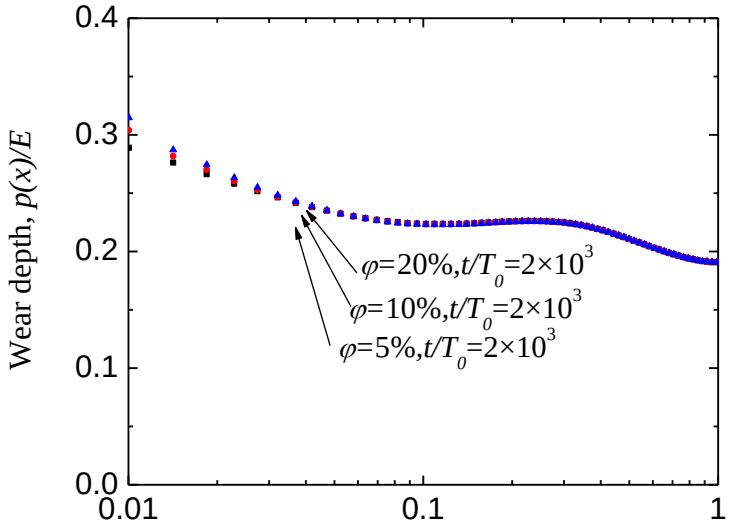

(b)

Figure 5-8: The evolution of contact pressure (a) and wear depth (b) for a full-slip complete contact when the wear and creep comparably contribute to the stress relaxation. The curves converge to the same one as the threshold φ decreases from 20% to 5%.

5.4 Conclusions

In this chapter, we introduced an adaptive method to couple creep and wear under cyclic loading. The time scale of cyclic loading is coupled with that of wear and creep using effective cycles; The length of the effective cycles are optimized by a prediction algorithm in which the change of contact pressure is limited within a threshold value. The method is shown to be robust in modeling problems when creep or wear causes either global or localized stress redistribution. The method automatically determines reasonable time increments without raising the complexity of identifying the dominant mechanism. Using this method, the efficiency of simulation is improved significantly.

Chapter 6

The effects of frequency and gap on GTRF wear

6.1 Introduction

As mentioned in Chapter 1, GTRF is a phenomenon in which the turbulent flow of the coolant exerts excitation forces on the fuel rods, causing the rods to vibrate against the grid that supports them. This leads to fretting wear of the rod surface, i.e. the Zircaloy cladding around the fuel [2, 3]. While it has been recognized that the problem is caused by the complex interaction between the rod, grid and coolant [5, 7-13], there is a lack of quantitative understanding of how the wear rate depends on the size of the gap between the grid and the rod (referred later as gap size), and on the frequency of the excitation force (referred later as excitation frequency). In this chapter we will address these two important factors and their roles in the GTRF problem.

The gap between a fuel rod and the grid depends on many factors. The rod is designed to be held in place by a small compressive load between the grid and the rod using an initial interference. However, this load can be relaxed by creep and deformation during assembly [2, 97], transportation [2] and operation [38, 39, 98]. During operation a gap can open because of creep-down on the cladding [98], or close again because of fuel swelling or expansion from hydride formation. A gap can also be created as a result of the formation

of a wear scar [2, 99]. Therefore, understanding how the fretting wear is affected by the gap is of critical interest in the design of nuclear reactors.

The gap size plays an important role in determining the wear rate. Multiple possible scenarios may work together. A close fit between the rod and grid is often associated with a larger contact pressure and frictional force, which tends to increase the wear rate when sliding happens. However, a sufficiently tight fit can restrict sliding at the contact interface and therefore reduce the wear rate. A loose connection between the rod and grid may lead to a high dynamic impact load during oscillation; this would increase the wear rate [1, 4, 19, 37]. However, if the gap between the rod and the grid is too large, the oscillation may not have sufficient amplitude to cause contact to happen at all; this would reduce the wear rate. Of course, this is not a desirable condition even though the wear is minimal since the spacer grid will not be able to provide adequate support for the fuel rod.

The wear rate is also sensitive to the excitation frequency, which depends on the mechanical design and flow velocity [2, 100]. Conceptually, the wear rate is expected to increase with the fretting frequency [8] and the vibration amplitude of the rod, since a higher fretting frequency means more fretting cycles per unit time while a larger amplitude is associated with a larger frictional force. However, the situation is more intriguing since fretting frequency of the rod and its vibration amplitude are not independent. The excitation frequency affects both the fretting frequency and the amplitude in a non-monotonic way, making the effect of excitation frequency on wear complicated. We found that as the excitation frequency varies, the rod vibration mode may experience sub-harmonic, period doubling and chaotic regimes [25]. The dependence of the fretting frequency and amplitude of

the rod on the excitation frequency may change dramatically when the vibration mode of the rod evolves from one regime to another.

Experimental [4, 19, 37] and numerical studies [3, 21, 26, 101-105] have shown various and sometimes conflicting trends in GTRF, which calls for a complete understanding of the mechanisms. For example, experimental testing of several designs of spacer grids suggests that large gaps result in larger wear depths [4, 19, 37]. However, the conclusions are tied to the specific conditions and limited range of gap sizes that were tested. Numerical models give inconclusive results: some suggest that the wear rate may decrease with the gap size [20, 21] while others give completely opposite predictions [13, 103]. Experiments based on a displacement controlled impact system suggest that the wear rate increases with the number of fretting cycles [8]. However, the effect of excitation frequency on the fretting frequency and vibration amplitude of the rod cannot be captured by a displacement controlled system, and they play important roles in determining the wear rate [25].

Most existing numerical models on GTRF have been based on 1-D simulations. While these models are capable of estimating how normal loads and displacements are affected by the geometry and vibration, they cannot provide local wear information. Local wear rates are important for the prediction of fuel rod failures [106], since such failures require details about the contacts and local stresses [107]. In this chapter we use 3-D finite-element modeling to explore the dynamic response of a fuel rod under the driving forces of various frequencies induced by the coolant, the effects of the gap size and initial interference on the wear rate of the rod, and the effect of the excitation frequency on the wear rate. A key contribution of this chapter is to determine the critical gap size that generates the maximum

wear rate and how this critical size depends on the excitation frequency and the dynamic response of the rod.

6.2 Numerical Method

A fuel rod with four supports is shown in Figure 6-1. The two ends of the rod are pinned. The supports are connected to a fixed spacer grid by springs. The stiffness of these springs can reflect the effective stiffness of more complicated support structures. There is a gap or an interference between the rod and the supports, which is adjusted as part of the numerical studies. In this chapter, an interference fit is denoted as a negative gap. The fuel rod is composed of Zircaloy cladding and UO_2 fuel pellets. We lump their mass together when considering the rod vibration. The stiffness of the rod mainly comes from the Zircaloy cladding, since the UO_2 pellets are isolated and their contribution to the rod stiffness can be neglected. We consider rod vibration along the diagonal direction of the *x* and *y* axes. Because of symmetry, the rod displacements in the *x* and *y* directions are the same. The non-dimensional groups are listed in Table 6-1.

Table 6-1: Fixed parameters of the system

L / D_c	920
R / D_c	7.5
$\frac{F_a}{D_c k_s}$	1.2×10^{-4}
μ	0.25
αE	3×10^{4}
$\frac{k_s}{E D_c}$	2×10^{-3}
$\frac{\rho L^2 f_n^{\,2}}{E}$	6×10^{-6}

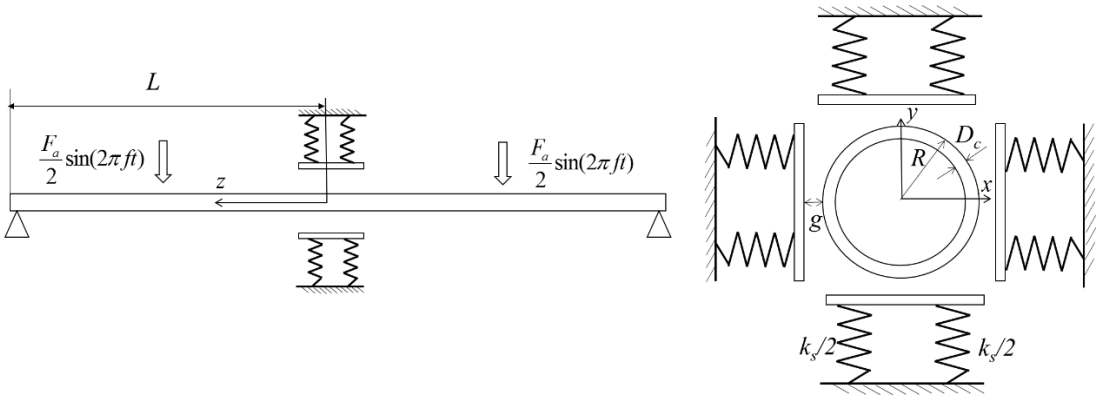

Figure 6-1: A sketch of the model used for the GTRF simulation. The fuel rod has an outer radius of R with a cladding thickness of D_c. Four support plates are connected to springs with a stiffness of k_s. The gap between the fuel rod and the plate is g. The rod vibrates along the diagonal direction of the x and y axes.

Figure 6-2 shows a 3-D finite-element model of the rod and supports. The mesh around the contact areas is refined to capture the contact information accurately. The mesh size is refined sufficiently to reduce the associated numerical errors to less than the error bars appeared in the figures of the result sections. The length and width of the contact plates are 1.7 and 0.7 times of the outer radius of the rod, respectively. The material of plates is Zircaloy- and their dynamic responses are captured by the associated springs having a characteristic stiffness of k_s. Our simulations showed that the material damping effect of the support grid is negligible. The dynamic response of the system is modeled using ABAQUS implicit dynamics. The contact between the plates and the fuel rod is formulated using a master-slave contact pair: the surface nodes on the slave surface will move to avoid penetration to the master surface. We validated our model by test calculations using the same dimensions, boundary conditions and material properties as those in experiments [108] and

other numerical simulations [109]: the vibration displacement and the impact force that we obtained were consistent with those published results.

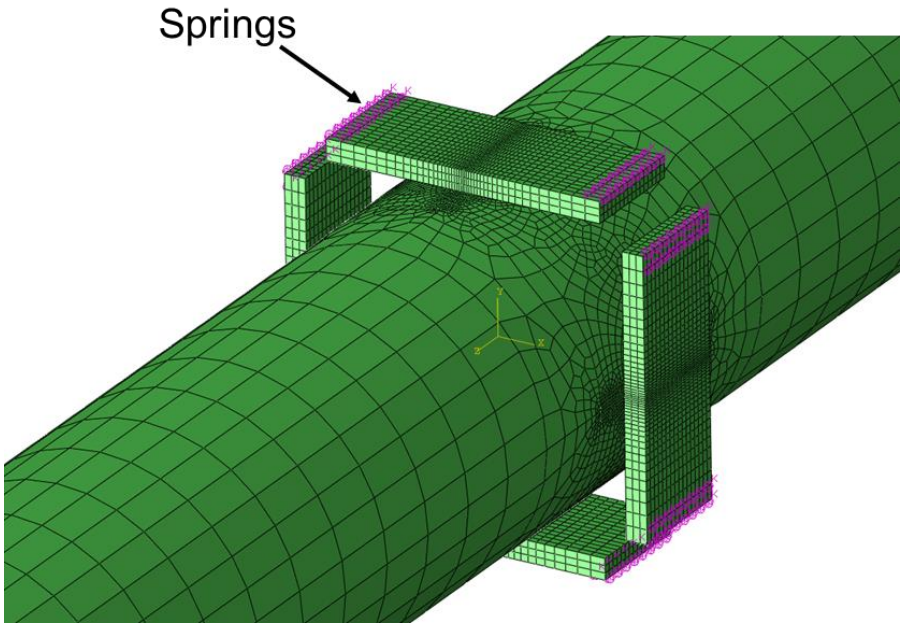

Figure 6-2**:** The 3-D finite element model for dynamic simulations. Each plate is connected to ground springs with total stiffness of k_s normal to the plate. Contact elements and refined meshes are used in the contact regions.

The excitation force is modeled as a harmonic load to study the effect of various frequencies. We investigated a large spectrum of gap sizes and excitation frequencies. For each calculation, we ran a transient simulation until a steady-state response emerged, or until we could determine that the response was chaotic. The chaotic response is expected to appear in some regimes during oscillating impact [24, 25, 110]. When periodic rod vibrations can be identified, we use the steady-state vibration response to compute and evaluate the wear rate. Otherwise, the behavior is identified as chaotic. From the perspective

of understanding GTRF, it is important to appreciate that chaotic behavior can emerge even when the driving force is harmonic.

The wear rate associated with different parameters is estimated using Archard's Law [54]. In the local form of this law, the evolution of the wear depth, *w*, with time *t* at any point (*x*, *y*) on a surface is given by

$$w(x, y, t) = \mu\alpha \int_0^t p(x, y, t) d\Delta \tag{7-1}$$

where t is time, *p(x,y,t)* is the local contact pressure, μ is the coefficient of friction, α is the wear coefficient, and Δ is the local slip distance. In this chapter we define an average wear rate to evaluate and compare the growth rate of wear depth under various conditions. If the rod vibration can reach a steady periodic state, we calculate the average wear rate by computing the accumulated wear depth over 5 rod vibration cycles and divide it by the total time of these 5 cycles. Here we use 5 cycles instead of simply calculating over 1 cycle to reduce the numerical error. If rod vibration has no periodicity and is identified as chaotic, we calculate the average wear rate by computing the accumulated wear depth over 5 cycles of the excitation force and divide it by the total time of these 5 excitation cycles.

6.3 Results

6.3.1 Vibrational response

Several studies [110, 111] have shown that the vibrational response of an object is sensitive to the excitation frequency, and may exhibit several types of vibrational behaviors. For the GTRF problem considered here, we first need to determine whether the system can reach a steady-state of vibration. We have identified three types of vibrations; Type 1: The

fuel rod impacts on the plate in each fretting cycle and the vibration displacement is the same for each fretting cycle; Type 2: The fuel rod impacts on the plate in each fretting cycle but the vibration displacement is different between sequential fretting cycles; Type 3: The fuel rod may not impact on the plate in some cycles and the vibration is chaotic. Figure 6-3 shows examples of these three types of vibrational responses. In the figures the time is normalized by the first natural frequency of free rod vibration which was obtained by calculating the vibration mode of a free rod without any support plate, while the displacement is normalized by the cladding thickness. The first two types are periodic but differ in the vibration period. The vibration period of the first type is the same as that of the excitation force; however, the period of the second type is greater than that of the excitation force. We refer the regimes associated with type 1 and 2 as subharmonic and period doubling, respectively. The type 3 is not periodic and there may or may not be impact in any excitation cycle; therefore it is termed as the chaotic regime [110, 112]. The wear rate of the chaotic vibration is relatively low since the number of impact with the plate per unit time is small.

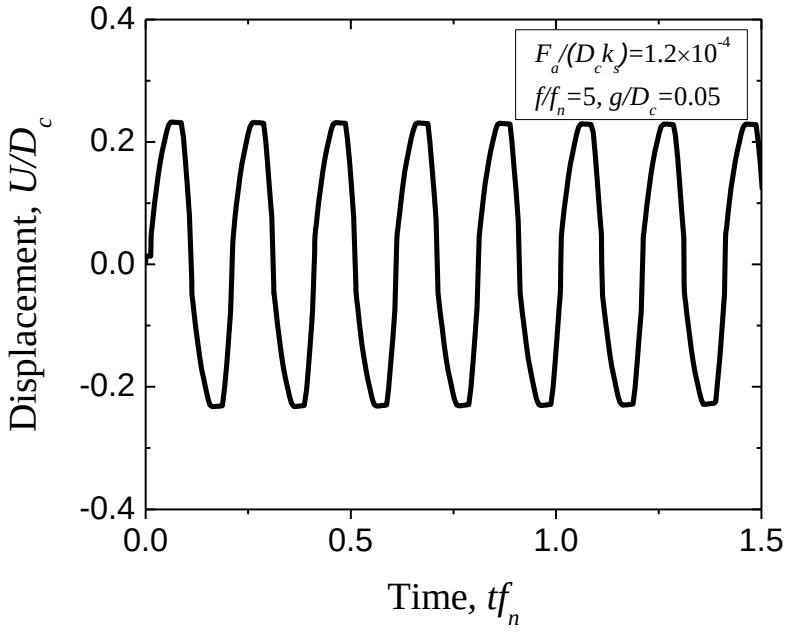
$F_a/(D_c k_s)$=1.2×10^{-4}
f/f_n=5, g/D_c=0.05
Displacement, U/D_c
Time, tf_n
0.4
0.2
0.0
-0.2
-0.4
0.0
0.5
1.0
1.5

(a)

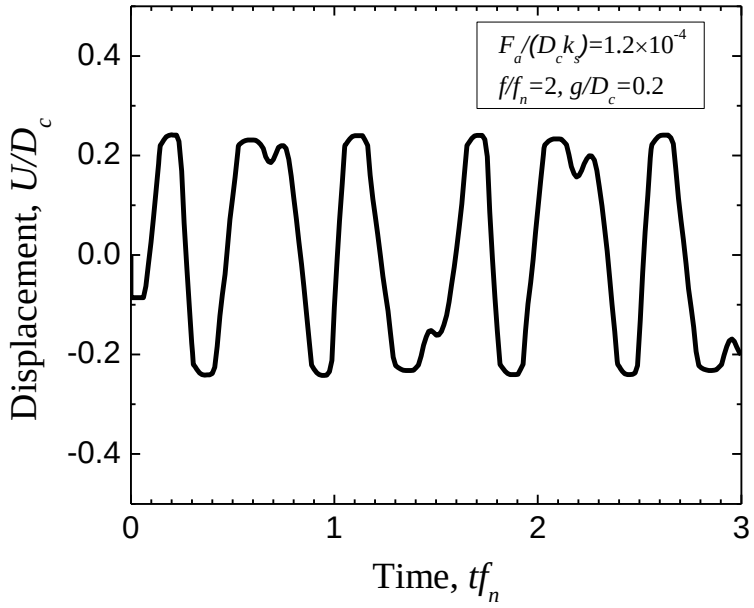
$F_a/(D_c k_s)$=1.2×10^{-4}
f/f_n=2, g/D_c=0.2
Displacement, U/D_c
Time, tf_n
0.4
0.2
0.0
-0.2
-0.4
0
1
2
3

(b)

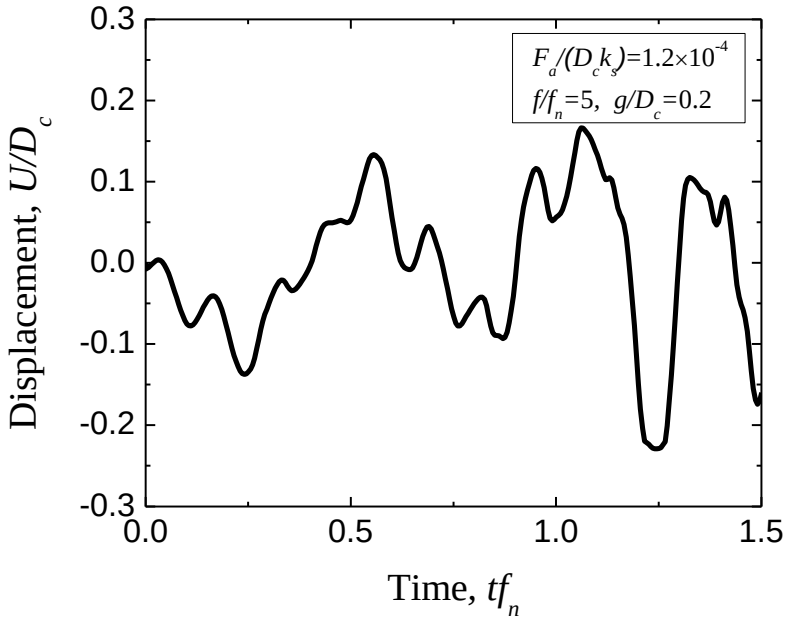

(c)

Figure 6-3**:** Three types of vibrations. (a) Type 1: the rod impacts on the plate in each fretting cycle. The rod vibration is periodic and its period is equal to that of the excitation force. (b): Type 2: the rod impacts on the plate in each fretting cycle. The rod vibration is periodic but its period is greater than that of the excitation force. The rod vibration period changes with the gap size. (c) Type 3: the rod may or may not impact on the plate in any excitation cycle and the vibration is chaotic.

Figure 6-4 shows the impact force on the fuel rod in the subharmonic regime. The impact force is defined as the integration of the contact pressure *p(x,y,t)* over the contact area. As the gap size increases, the impact force increases as well. The contact slip also increases with the gap, therefore the wear depth per fretting cycle goes up. However, it should be noted that this trend persists only in the subharmonic regimes, since the contact force and slip change in a non-monotonic way in the period doubling and chaotic regimes.

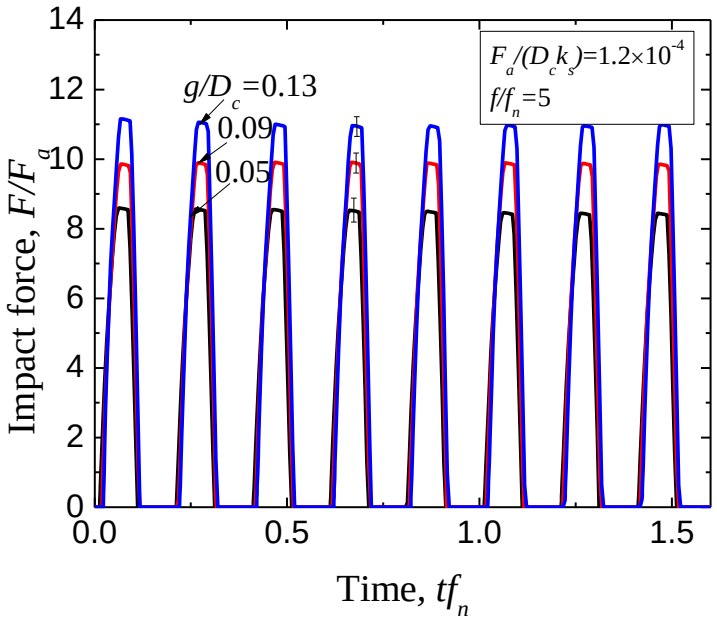

Figure 6-4**:** The impact force increases with the gap size, g/D_c, in the subharmonic regime

6.3.2 The effects of gap size and excitation frequency on the wear rate

Subharmonic regime: We calculated the wear rate using the method discussed in Section 2. The maximum local wear rate, $W_{d,m}$, was obtained by surveying all contact points in the contact area. The dependence of the maximum local wear rate on the gap size is shown in Figure 6-5. The maximum wear rate increases with the gap size until it peaks at a particular gap that we call the critical gap size, and then drops suddenly. The positive correlation between the maximum wear rate and the gap size in the subharmonic regime can be understood by referring to Figure 6-4. As the gap increases, both the impact force and the slip distance increase. Therefore, the frictional work rate becomes larger and the wear in a fretting cycle increases. The number of impacts per unit of time in the subharmonic regime is the same as the excitation frequency, and does not change with the gap size. As a result,

the wear rate increases with the gap size. Beyond the critical gap size, the vibration becomes chaotic. In the chaotic regime, the vibration is not periodic and the wear rates will somewhat depend on the specific sampling intervals that are chosen for evaluation. But they are all very small in comparison to the wear rate in the subharmonic and period doubling regimes, as shown in Figure 6-5. The reason for this small wear rate is that the chaotic vibration significantly reduces the chances of contact between the fuel rod and the plate, as shown in Figure 6-3 (c). While in the chaotic regime the vibrational behavior is fairly complicated due to lack of periodicity, for practical applications we do not need to worry much about this regime since the wear rate is small. A comparison between the figures in Figure 6-5 shows that the wear rate is also strongly dependent on the excitation frequency. When the normalized excitation frequency, f/f_n, increases from 3 to 5, the maximum wear rate increases significantly, while the corresponding critical gap size decreases.

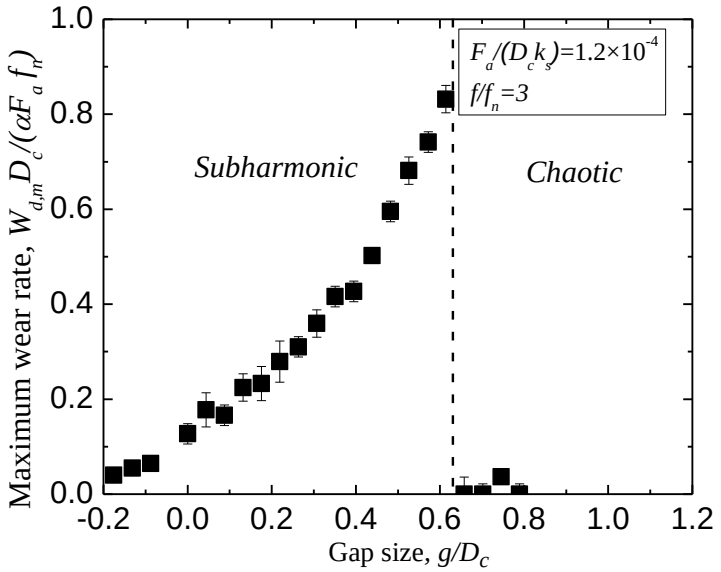

(a)

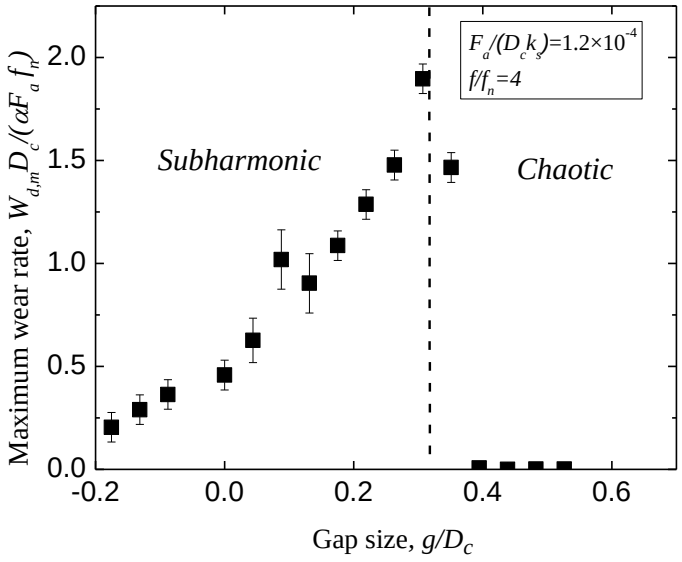

(b)

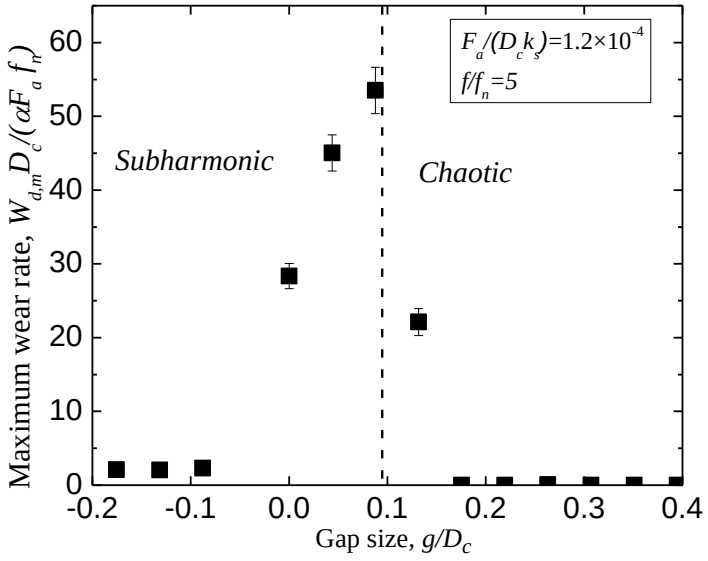

(c)

Figure 6-5**:** Plots of the relationship between the maximum local wear rate and the gap size at various excitation frequencies of f/f_n=3, 4 and 5. The wear rate of an interference (negative gap size) is smaller than that of a gap. The wear rate increases with the gap size until it peaks at a particular gap that we call the critical gap size. Beyond this the vibration becomes chaotic and the wear rate drops dramatically.

Period doubling regime: Figure 6-6 shows the relationship between the wear rate and the gap size under a lower excitation frequency, where the period doubling regime appears. Although the wear rate still increases with the gap size in the period doubling regime, it fluctuates more significantly. A comparison between Figure 6-6 and Figure 6-5 shows that the wear rate is smaller for those conditions where a period doubling regime exists. It should be noted that there is no sharp boundary between the subharmonic, period doubling and chaotic regimes. For example, the period of vibration may become too large to be identified around the boundary between period doubling and chaotic regimes.

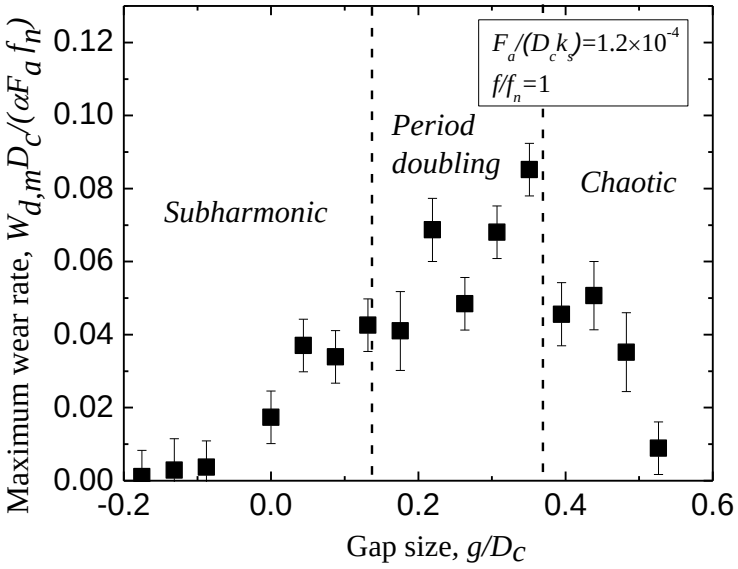

Figure 6-6**:** Plot of the relationship between the maximum local wear rate and the gap size at the excitation frequencies of *f/fn*=1. With the existence of a period doubling regime, the wear rate is smaller than that in Figure 6-5.

6.3.3 A wear rate map of the gap size and the excitation frequency

We performed a series of calculations similar to those in Figure 6-6 and Figure 6-5 to cover a large spectrum of gap sizes and excitation frequencies. The results are presented as

a wear map in Figure 6-7, which shows the dependence of the wear rate on the gap size and excitation frequency. In the subharmonic regime, for each excitation frequency, there is a critical gap size associated with the maximum wear rate. When the gap size exceeds the critical value, the vibration becomes chaotic and the wear rate drops dramatically. The critical gap that is associated with the peak wear rate is dependent on the excitation frequency. We found that the maximum wear rate in the landscape of gap size and excitation frequency is closely related to resonance to the system natural frequency, which is defined as the first mode free vibration frequency of the rod and support plates system. To determine the system natural frequencies, we applied an initial displacement to the rod and it is large enough to cause contact between the rod and the plate. We then released it and calculated the vibration frequencies based on the displacement at the middle of the fuel rod. When the gap size is relatively small, we found that the vibration is dominated by the first mode and therefore the system natural frequency is straightforward to determine. The dependence of the system natural frequency on the gap size in this regime is shown in Figure 6-7. The curve appears to generally overlap with the peaks in the contour. In other words, the peak wear rates appear to happen in resonance with the system natural frequency. Although the amplitude of the excitation force affects the magnitude of the wear rate, it has little effect on the location of the peak wear rate on the map. The reason is that the system natural frequency is independent of the loading amplitude. Figure 6-8 shows how the system natural frequency depends on the gap size. With increasing gap size, the system nonlinearity becomes more significant. The dependence of the wear rate on the gap size and the excitation frequency becomes more complicated due to the appearance of period doubling. However, the wear rate in this regime is much smaller.

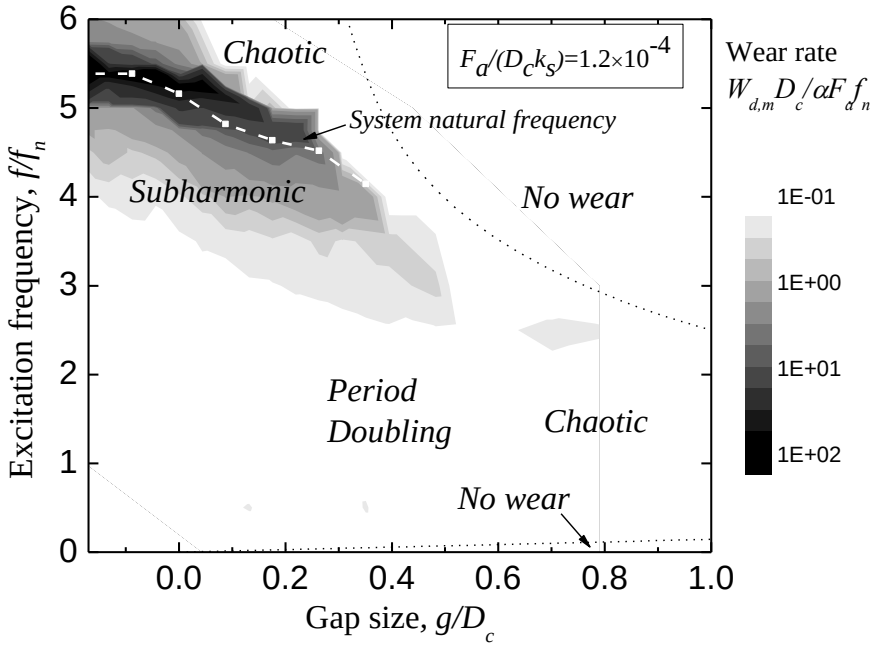

Figure 6-7**:** The wear rate map for a large spectrum of gap sizes and excitation frequencies. The critical gap size, which is associated with the maximum wear rate, lies within the subharmonic regime. In the no wear region the amplitude of the rod vibration is smaller than the gap size so that no impact between the rod and plate can happen. The curve of system natural frequency appears to generally overlap with the peaks in the contour.

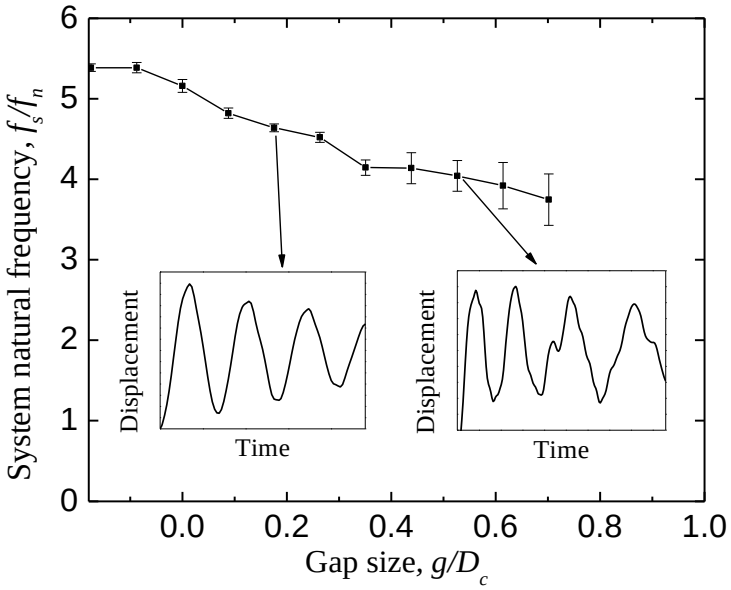

Figure 6-8**:** The dependence of the system natural frequency on the gap size. The behavior becomes more complicated when the gap size is large.

For a given excitation frequency and amplitude, if the gap size is larger than the vibration amplitude of a free rod, there will be no wear. We simulated the vibration of a free rod under different excitation frequencies. Using the maximum vibration amplitude, we can identify the wear and no wear regimes, which are shown in Figure 6-9 as well as partially shown in Figure 6-7. When the excitation frequency is close to the natural frequency of the free rod, or f/f_n=1, we have the largest possible gap size that engages some wear. However, as shown in Figure 6-7, the wear rate is relatively small in this condition. We can also gain some insights on the excitation frequency from the perspective of wear growth. The growth of wear depth results in an increase of the gap size. When the excitation frequency is relatively low, say close to or a little above f/f_n=1, the wear scar grows slowly. However, the wear action will take effect for an extended time, changing the contact surface geometry even when the gap becomes relatively large. On the other hand, if the excitation frequency

is relatively large, the corresponding wear rate in the subharmonic regime is large. The wear scar will grow fast at the beginning and then decrease quickly with the increase of the gap size as the vibration becomes chaotic. No wear will happen when the gap size is sufficiently large.

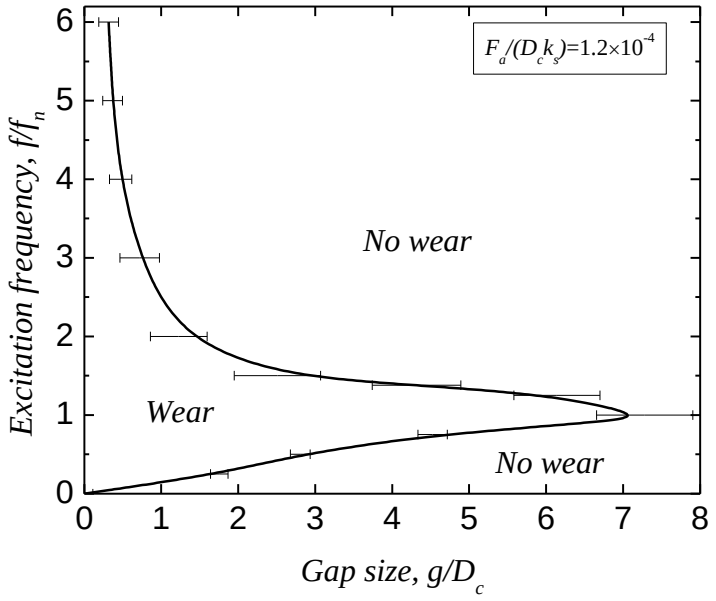

Figure 6-9**:** There is no wear if the gap size is larger than the vibration amplitude of the rod.

6.4 Conclusions

In this chapter we investigated the effects of gap size and excitation frequency on the vibration and wear rate of a fuel rod using a 3D dynamic model. It is observed that the wear rate is sensitive to the vibration response of the system. The wear rate in the subharmonic regime is significantly larger than that in the period doubling or chaotic regimes. Based on simulations of a large spectrum of gap sizes and excitation frequencies, we found that there is a critical gap size resulting in the maximum wear rate and this critical gap depends on

the excitation frequency. The peak wear rate appears to correlate to the resonance response to a system natural frequency, which further depends on the gap size. By avoiding the high wear rate regimes through geometry design of fuel assembly and optimization of the flow velocity, the risk of fuel leak due to GTRF wear can be significantly reduced. For this purpose, our present chapter focused on quantifying and evaluating the effect of gap size on the wear rate. Tracking the growth of wear scars as well as incorporating mechanisms such as creep is currently in progress.

Chapter 7

Conclusions and outlook

In this dissertation, the fundamental contact mechanics for the onset and propagation of GTRF wear, and its dependence on the gap size and excitation frequency, is studied. The geometry design of the springs/dimples is a key factor to the onset of GTRF wear; it determines the partial-slip wear behaviors around the contact edges. The propagation of wear is investigated using contacts with both sharp and rounded corners. The models are normalized in a general way so that the results can be easily projected to a specific geometry design and material. For contacts with a sharp contact edge, the incorporation of an interfacial shear strength significantly reduces the sensitivity of slip to geometrical details due to the singularity. That is particularly important in determining wear near the sharp corners created by the punching of sheet metal (see Figure 1-3). The role of interfacial shear strength and plasticity are similar in the partial-slip wear propagation. They allow the partial-slip wear scar to propagate from the contact edge continuously to the entire contact interface, which is sharply different from results based on linear elastic model with a Coulomb friction law only.

The consideration of creep may accelerate the propagation of a partial-slip zone. An algorithm is developed to couple creep and wear. Using the effective cycle with a magni-

fied wear coefficient, the time scale of vibration and wear model can be effectively coupled. The efficiency of coupling creep and wear is realized by limiting the stress relaxation over an effective cycle less than a reasonable threshold. This method can be applied in various conditions when either creep or wear dominate stress relaxation, a contact edge is either smooth or sharp, and part or entire contact interface has slip.

The gap size and excitation frequency are two factors affecting the dynamic vibration of the rod, which led to three different regimes: subharmonic, period doubling and chaotic. The wear rate in the subharmonic regime is significantly larger than that in the other two regimes, and reaches maximum when the excitation frequency is close to a system natural frequency dependent on the gap size. The concept of critical gap size that gives the maximum wear rate for any excitation was introduced. The properties and values of the critical gap size was identified: the wear rate decreases when the gap size is larger or smaller. A wear map was developed based on a large amount of parametric studies. This map shows quantitatively the wear rate as a function of the gap size and excitation frequency, which will be a valuable tool for the design and optimization of the fuel assembly to reduce the risk of fuel leak due to GTRF.

The work presented in this dissertation provides guidelines in the design of PWR system in the aspects such as optimizing the spring/dimple geometry and flow rate. The fundamental mechanisms in contact mechanics and vibration as well as the modeling tools in this study can be potentially applied in future research. Of particular interest is the modeling of wear growth in a dynamic model. The growth of wear scar modifies the gap between the rod and spacer grid, which in turn affects the vibrations and wear. The role of excitation frequency in this problem become more critical and needs to be understood.

The wear modeling method based on the eigenstrain enables efficient wear modeling in dynamic solvers, which makes this type of simulation possible.

Bibliography

1. Kim, K.-T., *Applicability of out-of-pile fretting wear tests to in-reactor fretting wear-induced failure time prediction.* Journal of Nuclear Materials, 2013. **433**(1–3): p. 364-371.
2. Kim, K.-T., *A study on the grid-to-rod fretting wear-induced fuel failure observed in the 16×16KOFA fuel.* Nuclear Engineering and Design, 2010. **240**(4): p. 756-762.
3. Axisa, F., J. Antunes, and B. Villard, *Overview of numerical methods for predicting flow-induced vibration.* Journal of Pressure Vessel Technology, 1988. **110**(1): p. 6-14.
4. Kim, K.-T., *The study on grid-to-rod fretting wear models for PWR fuel.* Nuclear Engineering and Design, 2009. **239**(12): p. 2820-2824.
5. Kim, H.-K., Y.-H. Lee, and S.-P. Heo, *Mechanical and experimental investigation on nuclear fuel fretting.* Tribology International, 2006. **39**(10): p. 1305-1319.
6. Wang, H., et al., *A mechanism-based framework for the numerical analysis of creep in zircaloy-4.* Journal of Nuclear Materials, 2013. **433**(1–3): p. 188-198.
7. Kovács, S., et al., *Comparative study on rod fretting behavior of different spacer spring geometries.* Wear, 2009. **266**(1–2): p. 194-199.
8. Lee, Y.-H., H.-K. Kim, and Y.-H. Jung, *Effect of impact frequency on the wear behavior of spring-supported tubes in room and high temperature distilled water.* Wear, 2005. **259**(1–6): p. 329-336.
9. Sung, J.H., T.H. Kim, and S.S. Kim, *Fretting damage of TiN coated zircaloy-4 tube.* Wear, 2001. **250**(1–12): p. 658-664.
10. Yan, J., et al., *A new method to predict Grid-To-Rod Fretting in a PWR fuel assembly inlet region.* Nuclear Engineering and Design, 2011. **241**(8): p. 2974-2982.
11. Bortoleto, E.M., et al., *Experimental and numerical analysis of dry contact in the pin on disc test.* Wear, 2013. **301**(1–2): p. 19-26.
12. Kim, H.-K., et al., *Fretting wear of laterally supported tube.* Wear, 2001. **250**(1–12): p. 535-543.
13. Rubiolo, P.R. and M.Y. Young, *On the factors affecting the fretting-wear risk of PWR fuel assemblies.* Nuclear Engineering and Design, 2009. **239**(1): p. 68-79.
14. Kim, H.-K., Y.-H. Lee, and K.-H. Lee, *On the geometry of the fuel rod supports concerning a fretting wear failure.* Nuclear Engineering and Design, 2008. **238**(12): p. 3321-3330.
15. Shin, M.K., et al., *Optimization of a nuclear fuel spacer grid spring using homology constraints.* Nuclear Engineering and Design, 2008. **238**(10): p. 2624-2634.

16. Hu, Z., et al., *Simulation of wear evolution using fictitious eigenstrains.* Tribology International, 2015. **82, Part A**(0): p. 191-194.
17. Goryacheva, I.G., P.T. Rajeev, and T.N. Farris, *Wear in Partial Slip Contact.* Journal of Tribology, 2001. **123**(4): p. 848-856.
18. Delafontaine, S. and G. Ricciardi, *Fluctuating pressure calculation induced by axial flow trough mixing grid.* Nuclear Engineering and Design, 2012. **242**: p. 233-246.
19. Kim, K.-T. and J.-M. Suh, *Development of an advanced PWR fuel for OPR1000s in Korea.* Nuclear Engineering and Design, 2008. **238**(10): p. 2606-2613.
20. Rubiolo, P.R., *Probabilistic prediction of fretting-wear damage of nuclear fuel rods.* Nuclear Engineering and Design, 2006. **236**(14–16): p. 1628-1640.
21. Rubiolo, P.R. and M.Y. Young, *VITRAN: an advance statistic tool to evaluate fretting-wear damage.* Journal of Power and Energy Systems, 2008. **2**(1): p. 57-66.
22. Kim, K.-T., *The effect of fuel rod supporting conditions on fuel rod vibration characteristics and grid-to-rod fretting wear.* Nuclear Engineering and Design, 2010. **240**(6): p. 1386-1391.
23. Choi, M.H., et al., *Vibration analysis of a dummy fuel rod continuously supported by spacer grids.* Nuclear Engineering and Design, 2004. **232**(2): p. 185-196.
24. Shaw, S.W., *Forced vibrations of a beam with one-sided amplitude constraint: Theory and experiment.* Journal of Sound and Vibration, 1985. **99**(2): p. 199-212.
25. Shaw, S.W. and P.J. Holmes, *A periodically forced impact oscillator with large dissipation.* Journal of Applied Mechanics, 1983. **50**(4a): p. 849-857.
26. Park, N.-G., J.-M. Suh, and K.-L. Jeon, *Dynamic response of a nuclear fuel rod impacting on elastoplastic gapped supports.* Nuclear Engineering and Design, 2011. **241**(12): p. 4862-4873.
27. Kim, H.-K., *Mechanical analysis of fuel fretting problem.* Nuclear Engineering and Design, 1999. **192**(1): p. 81-93.
28. Hu, Z., W. Lu, and M.D. Thouless, *Slip and wear at a corner with Coulomb friction and an interfacial strength.* Wear, 2015. **338–339**: p. 242-251.
29. Hu, Z., et al., *Effect of plastic deformation on the evolution of wear and local stress fields in fretting.* International Journal of Solids and Structures, 2016. **82**: p. 1-8.
30. Churchman, C.M. and D.A. Hills, *General results for complete contacts subject to oscillatory shear.* Journal of the Mechanics and Physics of Solids, 2006. **54**(6): p. 1186-1205.
31. Ödfalk, M. and O. Vingsbo, *An elastic-plastic model for fretting contact.* Wear, 1992. **157**(2): p. 435-444.
32. Chang, L. and H. Zhang, *A Mathematical Model for Frictional Elastic-Plastic Sphere-on-Flat Contacts at Sliding Incipient.* Journal of Applied Mechanics, 2005. **74**(1): p. 100-106.
33. Kasarekar, A.T., et al., *Modeling of fretting wear evolution in rough circular contacts in partial slip.* International Journal of Mechanical Sciences, 2007. **49**(6): p. 690-703.
34. Johansson, L., *Numerical Simulation of Contact Pressure Evolution in Fretting.* Journal of Tribology, 1994. **116**(2): p. 247-254.
35. Ding, J., S.B. Leen, and I.R. McColl, *The effect of slip regime on fretting wear-induced stress evolution.* International Journal of Fatigue, 2004. **26**(5): p. 521-531.

36. Madge, J.J., et al., *Contact-evolution based prediction of fretting fatigue life: Effect of slip amplitude.* Wear, 2007. **262**(9–10): p. 1159-1170.
37. Kim, K.-T. and J.-M. Suh, *Impact of nuclear fuel assembly design on Grid-to-Rod Fretting Wear.* Journal of Nuclear Science and Technology, 2009. **46**(2): p. 149-157.
38. Woodford, D.A., *Creep analysis of zircaloy-4 and its application in the prediction of residual stress relaxation.* Journal of Nuclear Materials, 1979. **79**(2): p. 345-353.
39. Causey, A.R., G.J.C. Carpenter, and S.R. MacEwen, *In-reactor stress relaxation of selected metals and alloys at low temperatures.* Journal of Nuclear Materials, 1980. **90**(1): p. 216-223.
40. Hegadekatte, V., N. Huber, and O. Kraft, *Finite element based simulation of dry sliding wear.* Modelling and Simulation in Materials Science and Engineering, 2005. **13**(1): p. 57-75.
41. Põdra, P. and S. Andersson, *Simulating sliding wear with finite element method.* Tribology International, 1999. **32**(2): p. 71-81.
42. Söderberg, A. and S. Andersson, *Simulation of wear and contact pressure distribution at the pad-to-rotor interface in a disc brake using general purpose finite element analysis software.* Wear, 2009. **267**(12): p. 2243-2251.
43. Mukras, S., et al., *Numerical integration schemes and parallel computation for wear prediction using finite element method.* Wear, 2009. **266**(7–8): p. 822-831.
44. McColl, I.R., J. Ding, and S.B. Leen, *Finite element simulation and experimental validation of fretting wear.* Wear, 2004. **256**(11–12): p. 1114-1127.
45. Archard, J.F., *Contact and Rubbing of Flat Surfaces.* Journal of Applied Physics, 1953. **24**(8): p. 981-988.
46. Dundurs, J., *Discussion: "Edge-Bonded Dissimilar Orthogonal Elastic Wedges Under Normal and Shear Loading" (Bogy, D. B., 1968, ASME J. Appl. Mech., 35, pp. 460–466).* Journal of Applied Mechanics, 1969. **36**(3): p. 650-652.
47. Hills, D.A., et al., *Correlation of fretting fatigue experimental results using an asymptotic approach.* International Journal of Fatigue, 2012. **43**: p. 62-75.
48. Öqvist, M., *Numerical simulations of mild wear using updated geometry with different step size approaches.* Wear, 2001. **249**(1–2): p. 6-11.
49. Rezaei, A., et al., *Adaptive finite element simulation of wear evolution in radial sliding bearings.* Wear, 2012. **296**(1–2): p. 660-671.
50. Tang, L., et al., *A multilayer nodes update method in FEM simulation of large depth fretting wear.* Wear, 2013. **301**(1–2): p. 483-490.
51. Yeo, T. and J.R. Barber, *Finite element analysis of the stability of static thermoelastic contact.* Journal of Thermal Stresses, 1996. **19**(2): p. 169-184.
52. Barber, J.R., M. Davies, and D.A. Hills, *Frictional elastic contact with periodic loading.* International Journal of Solids and Structures, 2011. **48**(13): p. 2041-2047.
53. Hoeppner, D.W., *Fretting fatigue case studies of engineering components.* Tribology International, 2006. **39**(10): p. 1271-1276.
54. Johnson, K., *Contact mechanics*. 1984, Cambridge, UK: Cambridge University Press.
55. Sills, R.B. and M.D. Thouless, *Cohesive-Length Scales of Intrinsic and Extrinsic Toughening Mechanisms in Composites.* International Journal of Solids and Structures, 2015. **55**: p. 32-43.

56. Parmigiani, J.P. and M.D. Thouless, *The effects of cohesive strength and toughness on mixed-mode delamination of beam-like geometries.* Engineering Fracture Mechanics, 2007. **74**(17): p. 2675-2699.
57. Sills, R.B. and M.D. Thouless, *The effect of cohesive-law parameters on mixed-mode fracture.* Engineering Fracture Mechanics, 2013. **109**(0): p. 353-368.
58. Vingsbo, O. and S. Söderberg, *On fretting maps.* Wear, 1988. **126**(2): p. 131-147.
59. Zhou, Z.R., et al., *Progress in fretting maps.* Tribology International, 2006. **39**(10): p. 1068-1073.
60. Bay, N. and T. Wanheim, *Real area of contact and friction stress at high pressure sliding contact.* Wear, 1976. **38**(2): p. 201-209.
61. Bartos, P., *Review paper: Bond in fibre reinforced cements and concretes.* International Journal of Cement Composites and Lightweight Concrete, 1981. **3**(3): p. 159-177.
62. Okabe, T. and N. Takeda, *Estimation of strength distribution for a fiber embedded in a single-fiber composite: experiments and statistical simulation based on the elasto-plastic shear-lag approach.* Composites Science and Technology, 2001. **61**(12): p. 1789-1800.
63. Warren, P.D., T.J. Mackin, and A.G. Evans, *Design, Analysis and Application of an Improved Push-through Test for the Measurement of Interface Properties in Composites.* Acta Metallurgica Et Materialia, 1992. **40**(6): p. 1243-1249.
64. Marshall, D.B., M.C. Shaw, and W.L. Morris, *Measurement of Interfacial Debonding and Sliding Resistance in Fiber Reinforced Intermetallics.* Acta Metallurgica Et Materialia, 1992. **40**(3): p. 443-454.
65. Thouless, M.D., J.W. Hutchinson, and E.G. Liniger, *Plane-Strain, Buckling-Driven Delamination of Thin-Films - Model Experiments and Mode-Ii Fracture.* Acta Metallurgica Et Materialia, 1992. **40**(10): p. 2639-2649.
66. Bogy, D.B., *Two Edge-Bonded Elastic Wedges of Different Materials and Wedge Angles Under Surface Tractions.* Journal of Applied Mechanics, 1971. **38**(2): p. 377-386.
67. Hills, D.A. and D. Dini, *Characteristics of the process zone at sharp notch roots.* International Journal of Solids and Structures, 2011. **48**(14–15): p. 2177-2183.
68. Flicek, R., D.A. Hills, and D. Dini, *Progress in the application of notch asymptotics to the understanding of complete contacts subject to fretting fatigue.* Fatigue & Fracture of Engineering Materials & Structures, 2013. **36**(1): p. 56-64.
69. Hertz, H., *Ueber die Berührung fester elastischer Körper.* Journal für die reine und angewandte Mathematik, 1882. **1882**(92): p. 156-171.
70. Barber, J.R., *Elasticity*. 3rd ed. 2010, Dordrecht, NY: Springer.
71. Comninou, M., *Stress singularity at a sharp edge in contact problems with friction.* Zeitschrift für angewandte Mathematik und Physik ZAMP, 1976. **27**(4): p. 493-499.
72. Gdoutos, E.E. and P.S. Theocaris, *Stress Concentrations at the Apex of a Plane Indenter Acting on an Elastic Half Plane.* Journal of Applied Mechanics, 1975. **42**(3): p. 688-692.
73. Bao, G. and Z. Suo, *Remarks on Crack-Bridging Concepts.* Applied Mechanics Reviews, 1992. **45**(8): p. 355-366.
74. Giannakopoulos, Suresh, and Chenut, *Similarities of stress concentrations in contact at round punches and fatigue at notches: implications to fretting fatigue*

crack initiation. Fatigue & Fracture of Engineering Materials & Structures, 2000. **23**(7): p. 561-571.
75. Ciavarella, M., *The generalized Cattaneo partial slip plane contact problem. I—Theory.* International Journal of Solids and Structures, 1998. **35**(18): p. 2349-2362.
76. Ciavarella, M., *The generalized Cattaneo partial slip plane contact problem. II—Examples.* International Journal of Solids and Structures, 1998. **35**(18): p. 2363-2378.
77. Fouvry, S., K. Elleuch, and G. Simeon, *Prediction of crack nucleation under partial slip fretting conditions.* The Journal of Strain Analysis for Engineering Design, 2002. **37**(6): p. 549-564.
78. Hills, D.A. and L.J. Fellows, *Some observations on contact problems involving fretting in the presence of wear.* Wear, 1999. **231**(2): p. 319-324.
79. Jäger, J., *A New Principle in Contact Mechanics.* Journal of Tribology, 1998. **120**(4): p. 677-684.
80. Kuno, M., et al., *Initiation and growth of fretting fatigue cracks in partial slip regimes.* Fatigue & Fracture of Engineering Materials & Structures, 1989. **12**(5): p. 387-398.
81. Sum, W.S., E.J. Williams, and S.B. Leen, *Finite element, critical-plane, fatigue life prediction of simple and complex contact configurations.* International Journal of Fatigue, 2005. **27**(4): p. 403-416.
82. Araújo, J.A., et al., *A Crack Initiation Threshold Methodology in Fretting Fatigue.* The Journal of Strain Analysis for Engineering Design, 2006. **41**(5): p. 363-368.
83. Dini, D. and D.A. Hills, *Bounded asymptotic solutions for incomplete contacts in partial slip.* International Journal of Solids and Structures, 2004. **41**(24–25): p. 7049-7062.
84. Rice, J.R., *Limitations to the small scale yielding approximation for crack tip plasticity.* Journal of the Mechanics and Physics of Solids, 1974. **22**(1): p. 17-26.
85. Ciavarella, M. and G. Macina, *New results for the fretting-induced stress concentration on Hertzian and flat rounded contacts.* International Journal of Mechanical Sciences, 2003. **45**(3): p. 449-467.
86. Hutchinson, J.W., *Plastic stress and strain fields at a crack tip.* Journal of the Mechanics and Physics of Solids, 1968. **16**(5): p. 337-342.
87. Tvergaard, V. and J.W. Hutchinson, *The relation between crack growth resistance and fracture process parameters in elastic-plastic solids.* Journal of the Mechanics and Physics of Solids, 1992. **40**(6): p. 1377-1397.
88. Manonukul, A. and F.P.E. Dunne, *High– and low–cycle fatigue crack initiation using polycrystal plasticity*. Vol. 460. 2004. 1881-1903.
89. McDowell, D.L., *Simulation-based strategies for microstructure-sensitive fatigue modeling.* Materials Science and Engineering: A, 2007. **468–470**(0): p. 4-14.
90. McDowell, D.L. and F.P.E. Dunne, *Microstructure-sensitive computational modeling of fatigue crack formation.* International Journal of Fatigue, 2010. **32**(9): p. 1521-1542.
91. Abuzaid, W., H. Sehitoglu, and J. Lambros, *Plastic strain localization and fatigue micro-crack formation in Hastelloy X.* Materials Science and Engineering: A, 2013. **561**(0): p. 507-519.

92. Bevill, S.L., et al., *Finite element simulation of early creep and wear in total hip arthroplasty.* Journal of Biomechanics, 2005. **38**(12): p. 2365-2374.
93. Jacobs, O., et al., *Creep and wear behaviour of ethylene–butene copolymers reinforced by ultra-high molecular weight polyethylene fibres.* Wear, 2002. **253**(5–6): p. 618-625.
94. Lee, K.-Y. and D. Pienkowski, *Reduction in the initial wear of ultrahigh molecular weight polyethylene after compressive creep deformation.* Wear, 1997. **203–204**(0): p. 375-379.
95. Teeter, M.G., et al., *Wear and Creep Behavior of Total Knee Implants Undergoing Wear Testing.* The Journal of Arthroplasty, 2015. **30**(1): p. 130-134.
96. Frost, H.J. and M.F. Ashby, *Deformation Mechanism Maps: The Plasticity and Creep of Metals and Ceramics*. 1982, Oxford, UK: Pergamon Press.
97. Kim, K.-T., *The effect of fuel rod loading speed on spacer grid spring force.* Nuclear Engineering and Design, 2010. **240**(10): p. 2884-2889.
98. Wang, H., et al., *A mechanism-based framework for the numerical analysis of creep in zircaloy-4.* Journal of Nuclear Materials, 2013. **433**(1-3): p. 188-198.
99. Chung, I. and M. Lee, *An experimental study on fretting wear behavior of cross-contacting Inconel 690 tubes.* Nuclear Engineering and Design, 2011. **241**(10): p. 4103-4110.
100. Chen, S.S., S. Zhu, and Y. Cai, *Experiment of chaotic vibration of loosely supported tube rows in cross-flow*. Journal of Pressure Vessel Technology, 1995. **117**(3): p. 204-212.
101. Rogers, R.J. and R.J. Pick, *Factors associated with support plate forces due to heat-exchanger tube vibratory contact.* Nuclear Engineering and Design, 1977. **44**(2): p. 247-253.
102. Park, N.-G., et al., *Indirect estimation method of the turbulence induced fluid force spectrum acting on a fuel rod.* Nuclear Engineering and Design, 2009. **239**(7): p. 1237-1245.
103. Hassan, M.A., D.S. Weaver, and M.A. Dokainish, *A simulation of the turbulence response of heat exchanger tubes in lattice-bar supports.* Journal of Fluids and Structures, 2002. **16**(8): p. 1145-1176.
104. Timoshenko, S.P., *History of strength of materials: with a brief account of the history of theory of elasticity and theory of structure*. 1953, Toronto, Canada: Courier Dover Publications.
105. Johansson, L., *Beam motion with unilateral contact constraints and wear of contact sites.* Journal of Pressure Vessel Technology, 1997. **119**(1): p. 105-110.
106. Hassan, M.A., D.S. Weaver, and M.A. Dokainish, *A new tube/support impact model for heat exchanger tubes.* Journal of Fluids and Structures, 2005. **21**(5–7): p. 561-577.
107. Antunes, J., et al., *Coulomb friction modelling in numerical simulations of vibration and wear work rate of multispan tube bundles.* Journal of Fluids and Structures, 1990. **4**(3): p. 287-304.
108. Shin, Y., D. Sass, and J. Jendrzejczyk, *Vibro-impact responses of a tube with tube--baffle interaction*. 1978, Argonne National Lab., Ill.(USA).

109. Sauvé, R.G. and W.W. Teper, *Impact simulation of process equipment tubes and support plates—A numerical algorithm.* Journal of Pressure Vessel Technology, 1987. **109**(1): p. 70-79.
110. Moon, F.C. and S.W. Shaw, *Chaotic vibrations of a beam with non-linear boundary conditions.* International Journal of Non-Linear Mechanics, 1983. **18**(6): p. 465-477.
111. Shen, X., et al., *Numerical simulation of sliding wear for self-lubricating spherical plain bearings.* Journal of Materials Research and Technology, 2012. **1**(1): p. 8.
112. Thompson, J.M.T. and R. Ghaffari, *Chaos after period-doubling bifurcations in the resonance of an impact oscillator.* Physics Letters A, 1982. **91**(1): p. 5-8.